



DLR-IB-FA-BS-2019-105

**Structural Design of Intelligent
Wind Turbine Rotor Blades**

Masterarbeit

Maximilian Geers, Edgar Werthen



DLR

Deutsches Zentrum
für Luft- und Raumfahrt

Institut für Faserverbundleichtbau und Adaptronik

DLR-IB-FA-BS-2019-105

**Structural Design
of Intelligent
Wind Turbine Rotor Blades**

Zugänglichkeit:

Stufe 2 DLR intern zugänglich: analog „allgemein zugänglich“, allerdings ist dieser in ELIB nur für intern zugänglich abzulegen.

Braunschweig, Juli, 2019

Der Bericht umfasst: 142 Seiten

Abteilungsleiter:


Autor: Maximilian Geers

Prof.-Dr.-Ing. Christian Hühne




Betreuer: Edgar Werthen



Deutsches Zentrum
für Luft- und Raumfahrt

Hochschule Bremen

Fakultät 5: Natur und Technik

Master in Aerospace Technologies – Masterarbeit

Strukturelle Auslegung von intelligenten Windkraftanlagenrotorblättern

Structural Design of Intelligent Wind Turbine Rotor Blades

| | |
|--------------------|-----------------------------------|
| Studierender: | Maximilian Geers |
| Matrikel-Nummer: | 5017082 |
| 1. Prüfer: | Prof. Dr.-Ing. Dirk Hennigs |
| 2. Prüfer: | Dr.-Ing. M.Sc. Frank Kortenstedde |
| Betreuer beim DLR: | M.Sc. Edgar Werthen |

Bremen, 30.11.2018 to 16.05.2019

Erklärung über das eigenständige Erstellen der Arbeit

Hiermit versichere ich, dass ich die vorliegende Arbeit oder die von mir im Rahmen der Gruppenarbeit verantworteten, entsprechend gekennzeichneten Teile der Arbeit selbstständig verfasst und keine anderen als die angegebenen Quellen und Hilfsmittel benutzt habe. Die Stellen der Arbeit, die anderen Werken dem Wortlaut oder dem Sinn nach entnommen wurden, sind durch Angaben der Herkunft kenntlich gemacht.

Diese Erklärung erstreckt sich auch auf in der Arbeit enthaltene Grafiken, Skizzen, bildliche Darstellungen sowie auf Quellen aus dem Internet.

Die Arbeit habe ich in gleicher oder ähnlicher Form auch auszugsweise noch nicht als Bestandteil einer Prüfungs- oder Studienleistung vorgelegt.

Ich versichere, dass die eingereichte elektronische Version der Arbeit vollständig mit der Druckversion übereinstimmt.

Studierender: Maximilian Geers

Matrikelnummer: 5017082

(Ort, Datum)

(Unterschrift)

Abstract

Das Ziel der vorliegenden Masterthesis ist es, Konzepte von strukturellen Auslegungen von Windkraftanlagenrotorblättern zu untersuchen, die eine Lastenreduktion bewirken sollen. Diese Lastenreduktion soll dazu führen, größere Rotordurchmesser für Windkraftanlagen umsetzbar zu machen, oder bestehende Blätter kostengünstiger herzustellen indem das Gewicht des Blattes gesenkt wird. Mit Hilfe von automatisierten Prozessen werden dabei die strukturellen Modelle anhand eines Referenzrotorblattes aufgebaut und anschließend die dazu gehörigen Lasten simuliert. Die resultierenden Lasten und Massen der unterschiedlichen Konzepte werden mit denen des Referenzrotorblattes verglichen. Die Ergebnisse zeigen, dass sowohl ein strukturelles Design mit einem C-Balken, als auch ein strukturelles Design mit einem geschwungenen Balken zu einer Lastenreduktion führt. Ein weiteres Konzept, welches auf der Benutzung einer aktiven Hinterkantenklappe basiert, kann nur anhand von Referenzlasten bewertet werden. Hier zeigt sich ein deutlicher Gewichtsanstieg, der durch eine Lastenreduzierung durch die Klappe aufgefangen werden muss.

The aim of the present master thesis is to investigate concepts of structural designs of wind turbine rotor blades, which should result into a load reduction. This load reduction should lead to larger rotor diameters being feasible for wind turbines, or existing blades being produced more cost-effectively by reducing the weight of the blade. With the help of automated processes, the structural models are constructed using a reference rotor blade and then the associated loads are simulated. The resulting loads and masses of the different concepts are compared with those of the reference rotor blade. The results show that both a structural design with a c-beam and a structural design with a swept beam leads to a load reduction. Another concept based on the use of an active trailing edge flap can only be evaluated using reference loads. This shows a significant increase in weight, which must be absorbed by a load reduction through the flap

Table of Contents

| | |
|---|-------------|
| Abstract..... | i |
| Table of Contents | ii |
| List of Figures..... | iv |
| List of Tables | vi |
| List of Abbreviations..... | vii |
| List of Symbols..... | viii |
| 1 Introduction..... | 1 |
| 2 State of the Art | 2 |
| 2.1 Structural Design of Wind Rotor Blades | 2 |
| 2.2 Intelligent Wind Turbine Rotor Blades | 4 |
| 3 Approaches of the Research Topic Smart Blades 2..... | 7 |
| 4 Reference Wind Turbine..... | 10 |
| 5 Structural Requirements | 14 |
| 5.1 Engineering Standards..... | 14 |
| 5.2 Safety Factors | 16 |
| 6 Methodology | 19 |
| 6.1 FE Model..... | 19 |
| 6.2 Structural Sizing | 21 |
| 6.2.1 Iterative Sizing | 22 |
| 6.2.2 Material..... | 22 |
| 6.2.3 Assemblies and Sections..... | 28 |
| 6.2.4 Analysis Selections and Methods | 31 |
| 6.2.5 Further Development of Adaptive Twist Stiffness | 35 |
| 6.3 Loads Processing..... | 44 |
| 6.4 „Technology 1“ Process | 48 |
| 6.5 „Technology 2“ Process | 51 |
| 7 Optimization of the Structural Design..... | 53 |
| 7.1 „Technology 1“ | 53 |
| 7.1.1 C-Beam Concept | 58 |
| 7.1.2 Swept Beam Concept | 63 |
| 7.1.3 Induced Twist Concept | 67 |
| 7.2 „Technology 2“ | 67 |
| 8 Results Discussion..... | 70 |
| 8.1 Reference Design | 70 |
| 8.2 „Technology 1“ | 72 |
| 8.2.1 Induced Twist..... | 72 |

| | | |
|----------|--|------------|
| 8.2.2 | C-Beam | 83 |
| 8.2.3 | Swept Beam | 90 |
| 8.2.4 | Conclusion | 97 |
| 8.3 | „Technology 2“ | 100 |
| 9 | Conclusion and Outlook | 101 |
| | Bibliography | 102 |
| | Appendix | 104 |
| A. | C-Beam Layout 6 RBE Element Forces and Moments | 105 |
| B. | Swept Beam Layout 3 RBE Element Forces and Moments | 117 |

List of Figures

| | |
|---|----|
| Figure 2-1 Section of a modern Glider Wing [2]..... | 2 |
| Figure 2-2 Section of a modern Wind Turbine Rotor Blade [3] | 3 |
| Figure 2-3 Laminating of a Rotor Blade [3]..... | 4 |
| Figure 2-4 „Technology 2“ Flap Demonstrator [5]..... | 6 |
| Figure 2-5 Technology 2 Test Rig with installed Prototype [5]..... | 6 |
| Figure 3-1 Aerodynamic Forces acting on a Rotor Blade [6] | 7 |
| Figure 4-1 IWT-7.5-164 Reference Wind Turbine [8]..... | 10 |
| Figure 4-2 Power curve of the IWT-7.5-164 [7]..... | 11 |
| Figure 4-3 Negative Pre-Twist Angle [9]..... | 12 |
| Figure 4-4 Pre-Twist of the IWT-7.5-164 Rotor Blade [10]..... | 12 |
| Figure 4-5 Pre-Bend of the IWT-7.5-164 Rotor Blade [10] | 13 |
| Figure 6-1 Plan View on the FE Model of the Rotor Blade | 19 |
| Figure 6-2 Side View on the FE Model of the Rotor Blade | 20 |
| Figure 6-3 Plan View on the Spars in the FE Model | 20 |
| Figure 6-4 Side View on the Spars in the FE Model | 21 |
| Figure 6-5 Dynamic View on the RBE Elements in the FE Model of the Rotor Blade | 21 |
| Figure 6-6 Lamina directions [16] | 23 |
| Figure 6-7 In-Plane Forces on a Flat Laminate [18] | 25 |
| Figure 6-8 Moments on a Flat Laminate [18]..... | 25 |
| Figure 6-9 Layer Angle in Comparison to the Laminate Angle [16] | 26 |
| Figure 6-10 Lay-up Methods [20]..... | 28 |
| Figure 6-11 Foam Sandwich..... | 29 |
| Figure 6-12 Ply Stacks | 29 |
| Figure 6-13 Panels in Hypersizer | 31 |
| Figure 6-14 Blade Tip Deflection Node..... | 34 |
| Figure 6-15 Blade Tip Twist Nodes | 36 |
| Figure 6-16 Hypotenuse between Leading and Trailing Edge Node | 36 |
| Figure 6-17 Deflected Positions of the Leading and Trailing Edge Node | 37 |
| Figure 6-18 Imaginary Node | 37 |
| Figure 6-19 Stiffness Equations..... | 39 |
| Figure 6-20 Equation Mass Results..... | 41 |
| Figure 6-21 Stiffness Equation with adapted Start Point | 43 |
| Figure 6-22 Equation Mass Results for the different Start Point | 43 |
| Figure 6-23 Load Scenarios from IEC-61400 [11] | 45 |
| Figure 6-24 Explanation of the IEC-61400 Load Scenarios [11]..... | 46 |
| Figure 6-25 Extreme Load Case Table [24]..... | 47 |
| Figure 6-26 „Technology 1“ Optimal Induced Twist Process | 49 |
| Figure 6-27 „Technology 1“ RCE Process | 50 |
| Figure 6-28 „Technology 1“ Structural Optimization Process | 51 |
| Figure 6-29 „Technology 2“ RCE Process..... | 52 |
| Figure 7-1 Shear Centre of a Rectangular..... | 54 |
| Figure 7-2 Simplification of the Airfoil Geometry [9]..... | 54 |
| Figure 7-3 Centre of Pressure of the Airfoil [9] | 55 |
| Figure 7-4 Aerodynamic Forces in the Centre of Pressure [9]..... | 55 |
| Figure 7-5 Shifting of the Centre of Shear | 57 |
| Figure 7-6 C-Beam Concept Spar [28] | 58 |
| Figure 7-7 C-Beam Layout 1 | 61 |
| Figure 7-8 C-Beam Layout 2 | 61 |

| | |
|--|----|
| Figure 7-9 C-Beam Layout 3 | 61 |
| Figure 7-10 C-Beam Layout 4 | 62 |
| Figure 7-11 C-Beam Layout 5 | 62 |
| Figure 7-12 C-Beam Layout 6 | 62 |
| Figure 7-13 Swept Beam [28] | 63 |
| Figure 7-14 Swept Beam Layout 1 | 66 |
| Figure 7-15 Swept Beam Layout 2 | 66 |
| Figure 7-16 Swept Beam Layout 3 | 66 |
| Figure 7-17 Swept Beam Layout 4 | 66 |
| Figure 7-18 „Technology 2“ Flap Cut-Out Plan View | 68 |
| Figure 7-19 „Technology 2“ Spar Layout | 68 |
| Figure 7-20 Spar Course at the Flap Cut-Out..... | 69 |
| Figure 7-21 Flap Cut-Out with all Assemblies..... | 69 |
| Figure 8-1 Global Force Coordinate System [23] | 70 |
| Figure 8-2 Positive Induced Twist Angle [9] | 71 |
| Figure 8-3 Aerodynamic Loads - Reference Design vs. C-Beam Layout 6 | 74 |
| Figure 8-4 Relative Load Difference vs. Maximum Induced Twist | 77 |
| Figure 8-5 Aerodynamic Loads - Reference Design vs. C-Beam Layout 6 limited to 1.4° Induced Twist..... | 79 |
| Figure 8-6 Aerodynamic Loads - Reference Design vs. C-Beam Layout 6 limited to 0.8° Induced Twist..... | 80 |
| Figure 8-7 Aerodynamic Loads - Reference Design vs. C-Beam Layout 6 limited to 1.3° Induced Twist..... | 82 |
| Figure 8-8 Load Comparison for C-Beam Layout 6 | 86 |
| Figure 8-9 M_{xmax} Load Comparison for C-Beam Layout 6 | 88 |
| Figure 8-10 Relative Load Difference vs. Maximum Induced Twist C-Beam Concept | 90 |
| Figure 8-11 Relative Load Difference vs. Maximum Induced Twist Swept Beam Concept..... | 92 |
| Figure 8-12 Load Comparison for Swept Beam Layout 3..... | 94 |
| Figure 8-13 M_{xmax} Load Comparison for Swept Beam Layout 3 | 95 |
| Figure 8-14 Relative Load Difference vs. Maximum Induced Twist of the Investigated Structural Layouts | 97 |

List of Tables

| | |
|--|-----|
| Table 5-1 Applied Engineering Standards [8], [9]..... | 15 |
| Table 6-1 Hypersizer Assemblies | 30 |
| Table 6-2 Hypersizer Criteria | 33 |
| Table 6-3 Evaluated Load Scenarios | 46 |
| Table 7-1 „Technology 1“ C-Beam Layouts | 60 |
| Table 7-2 „Technology 1“ Swept Beam Layouts | 65 |
| Table 7-3 Flap Dimensions | 67 |
| Table 8-1 Reference Design Results | 72 |
| Table 8-2 Induced Twist Base Concept Results | 73 |
| Table 8-3 Limited Maximum Induced Twist Results..... | 76 |
| Table 8-4 Induced Twist Concept Non-Convergence Example | 81 |
| Table 8-5 C-Beam Concept Results | 84 |
| Table 8-6 Swept Beam Concept Results | 91 |
| Table 8-7 „Technology 2“ Results | 100 |

List of Abbreviations

| <u>Abbreviation</u> | <u>Explanation</u> |
|---------------------|---|
| AoA | <i>Angle of attack</i> |
| CFD | <i>Computational Fluid Dynamics</i> |
| COE | <i>Cost of Energy</i> |
| CPACS | <i>Common Parametric Aircraft Configuration Scheme</i> |
| DLC | <i>Design Load Case</i> |
| DLR | <i>Deutsches Zentrum für Luft- und Raumfahrt e.V.</i> |
| DLR-FA | <i>Deutsches Zentrum für Luft- und Raumfahrt e.V. – Institut für Faserverbundleichtbau und Adaptronik</i> |
| DNVGL | <i>Det Norske Veritas Germanischen Lloyd</i> |
| FE | <i>Finite Element</i> |
| FoS | <i>Factor of Safety</i> |
| FVWE | <i>Forschungsverbund Windenergie</i> |
| GBTK | <i>Geometrische Biege-Torsions Kopplung</i> |
| IEC | <i>International Electrotechnical Commission</i> |
| IWES | <i>Institut für Windenergie und Energiesystemtechnik</i> |
| MoS | <i>Margin of Safety</i> |
| N/A | <i>Not Available</i> |
| RBE | <i>Rigid Body Element</i> |
| SBTK | <i>Strukturelle Biege-Torsions Kopplung</i> |

List of Symbols

| <u>Abbreviation</u> | <u>Explanation</u> | <u>Unit</u> |
|---------------------|---|---------------------|
| \bar{Q}_{ij} | Reduced stiffness of a laminate | GPa |
| A_{ij} | Extensional stiffness | N/m |
| B_{ij} | Bending-extension coupling stiffness | N-m/m |
| D_{ij} | Torsional stiffness | N-m ² /m |
| E_c | Stiffness against compression | GPa |
| E_t | Stiffness against tension | GPa |
| F_D | Drag Force | N |
| F_L | Lift Force | N |
| F_{cu} | Allowed stresses through compression | MPa |
| F_{su} | Allowed stresses through in-plane shear | MPa |
| F_{tu} | Allowed stresses through tension | MPa |
| I_x | Moment of inertia in x direction | kgm ² |
| I_y | Moment of inertia in y direction | kgm ² |
| Q_{ij} | Reduced stiffness of a lamina | GPa |
| S_x | Static moment in x direction | m ³ |
| S_y | Static moment in y direction | m ³ |
| $a_{Deflection}$ | Factor for deflection analysis | - |
| a_{Twist} | Factor for twist analysis | - |
| c_d | Drag coefficient | - |
| c_l | Lift coefficient | - |
| e_{cu} | Allowed strain through compression | μm/m |
| e_{pb} | Pre-Bend | m |
| e_{su} | Allowed strain through in-plane shear | μm/m |

| | | |
|---------------------|---|-----------|
| e_{tu} | Allowed strain through tension | $\mu m/m$ |
| l_{Blade} | Length of Rotor Blade | m |
| l_{MP} | Distance in x direction between the pressure point and the shear centre | m |
| $l_{maxDeflection}$ | Maximal allowed deflection of the rotor blade | m |
| x_M | x coordinate of the shear centre | - |
| $x_{PresweepStart}$ | x coordinate of the start of the sweep | - |
| x_{Tip} | x coordinate of the blade tip | - |
| y_M | y coordinate of the shear centre | - |
| $z_{PresweepMax}$ | z coordinate of the maximum sweep | - |
| γ_{mFF} | Reduction factor for the material for fibre failure | - |
| γ_{mIFF} | Reduction factor for the material for inter-fibre failure | - |
| γ_{mStab} | Reduction factor for the material for stability and buckling | - |
| γ_{12} | Poisson's ratio | - |
| γ_S | Safety factor | - |
| γ_f | Partial safety factor for loads | - |
| γ_m | Partial safety factor for materials | - |
| γ_{m0} | Base reduction factor | - |
| γ_{m1} | Partial reduction factor for environmental degradation | - |
| γ_{m2} | Partial reduction factor for temperature effects | - |
| γ_{m3} | Partial reduction factor for manufacturing effects | - |
| γ_{m4} | Partial reduction factor for the accuracy of analysis methods | - |
| γ_{m5} | Partial reduction factor for the accuracy of load assumptions | - |

| | | |
|------------------------|---|----------|
| γ_{mc} | Partial reduction factor for criticality of failure mode | - |
| γ_n | Partial safety factor for consequences of failure | - |
| θ_{twist} | Twist Angle | ° |
| ρ_{Air} | Air Density | kg/m^3 |
| τ_{12} | Shear stress | N/m^2 |
| $\Delta z_{Reference}$ | Difference of the z coordinates of spar positions | - |
| ΔL | Relative load difference | % |
| h | Deflection of the blade tip | m |
| A | Cross Sectional Area | m^2 |
| F | Force | N |
| G | Stiffness against in-plane shear | GPa |
| M | Moment | Nm |
| N | Force per unit width | N/m |
| S | Wing Area | m^2 |
| c | Chord Length | m |
| s | Infinitesimal area of a general area | m^2 |
| t | Thickness of a layer of the laminate | mm |
| v | Speed | m/s |
| z | Distance of the layer to the middle surface of the laminate | m |
| α | Induced twist angle | ° |
| ε | Elongation | - |
| κ | Curvature | m^{-1} |
| ρ | Density | kg/m^3 |
| σ | Stress | N/m^2 |

1 Introduction

From an engineering perspective, the main task of today's wind turbine industry is to reduce the COE. The COE indicates the ratio of the total and operating costs of a wind turbine to its energy production in one year. In order to keep wind energy competitive in the future, this is probably the most critical economic aspect. This results in the following main point of attack for reducing COE: increasing energy production while maintaining or even reducing overall or operating costs. For this reason, various research institutes in the "Forschungsverbund Windenergie" have joined forces to research new technologies. Among others, the Fraunhofer IWES Northwest Institute and the DLR are part of this network. DLR in particular has established its own strategic field for wind energy. In this strategic field, various DLR institutes are conducting joint research on various projects. These include, for example, the Institute of Composite Structures and Adaptronics (DLR-FA).

One of the research projects is the "Smart Blades" project. The aim of this project is to reduce the loads acting on the rotor blades of wind turbines during operation. This should not only make it possible to further increase the rotor diameters of wind turbines in the future, but also to produce existing blades more cost-effectively by saving material or to increase their life span. Three technologies are subject of the research in the project:

- Passive rotor blades („Technology 1“), which are inducing twist while bending due to their geometric or structural design during aerodynamic load changes (so-called "Aeroelastic Tailoring"). Thus, a different angle of inflow along the blade is achieved by external loads
- Active rotor blades that can react to load increases due to changing wind conditions by means of a control flap attached either to the trailing edge („Technology 2“) or to the leading edge („Technology 3“).

The continuing research project "Smart Blades 2" is based on the research results achieved in the "Smart Blades" project. The research successes are presented in the chapter 2.2 for technology 1 and 2. The structural design optimization of the rotor blades for both technologies are the main topics for this thesis.

2 State of the Art

This section shall give an overview on the state of the art of the structural design of wind turbine rotor blades. Furthermore, the state of the art of the investigations, which have already been done in the “Smart Blades 1” research program, is described. The investigations of the “Smart Blades 2” project are based on the foregoing achieved results.

2.1 Structural Design of Wind Rotor Blades

Due to the immense wingspan of the current and upcoming wind turbine rotor blades, lightweight construction principles are in the foreground. Therefore, state-of-the-art rotor blades closely follow the design of aircraft wings. In detail, the design of current rotor blades is oriented on the structure of glass-fibre composite glider wings [1]. These wings are similar in many aspects:

- The usage of glass-fibre composite results in a low overall weight of the structure compared to aluminium construction methods
- The aerodynamic efficiency is a key aspect during the design process
- The great span of the wing

Figure 2-1 below shows the section of a modern glider wing. The wing is fabricated in a sandwich structure. The lower and upper skin of the sandwich structure is made from glass-fibre composite while the core is made from either a foam-like material or balsa wood. The spar (see “Holmsteg”) has a great benefit to the overall torsional stiffness of self-supporting rotors or wings. Additionally it increases the stiffness in the bending moment direction [1].

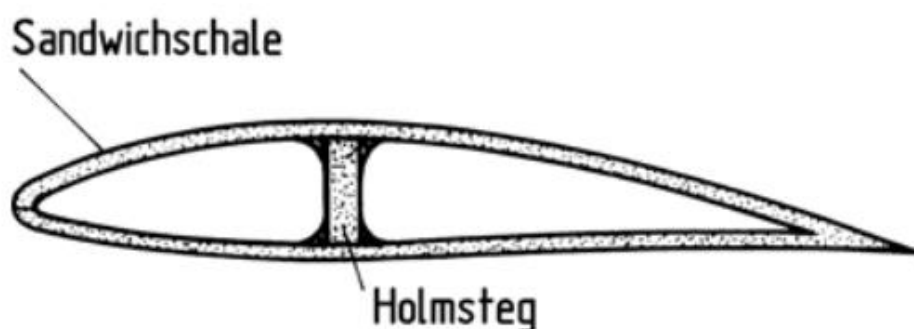


Figure 2-1 Section of a modern Glider Wing [2]

This design principle is applied to the design of wind turbine rotor blades. There are two different approaches for the spar construction. Either single/multiple spars are used or a box beam, see **Figure 2-2**.

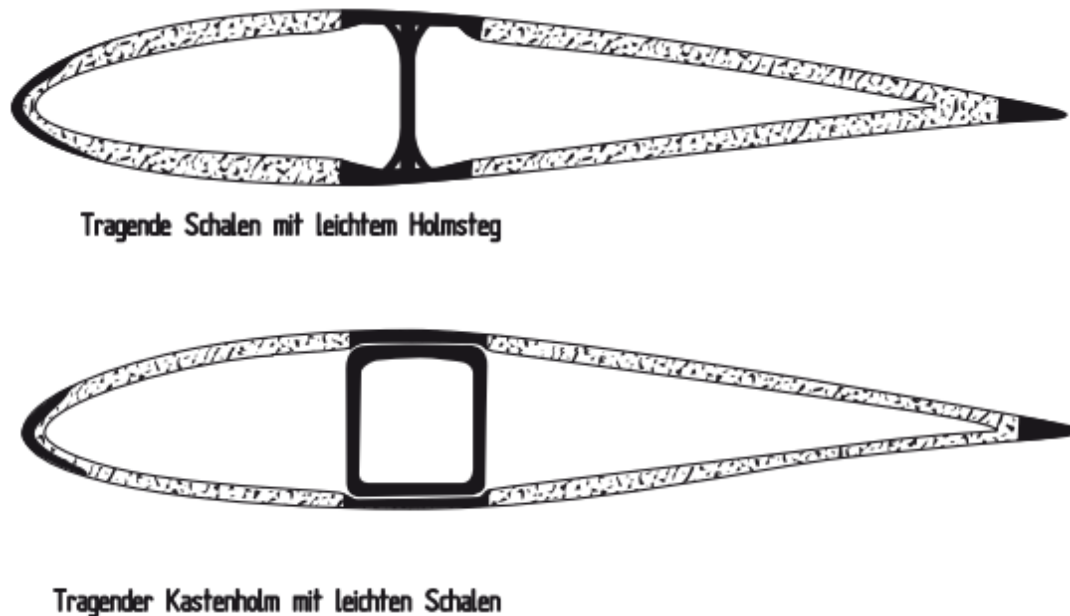


Figure 2-2 Section of a modern Wind Turbine Rotor Blade [3]

In both construction methods, the profiling skin is fabricated using a sandwich structure. In contrast, the beams or spars and their caps are manufactured from unstiffened glass-fibre composite layers. The spar caps are mainly absorbing the acting flapwise bending forces and moments.

In a box beam approach, the loads are mainly absorbed by the box beam, while the profiling skin is not necessarily required for load transfer. A single (or multiple) spar design favours the transfer of loads by means of the profiling skin. The spar design is advantageous because less material is required, thus reducing the overall cost of the rotor blade [3].

Current rotor blades are manufactured using glass-fibre composites with epoxy resin as matrix material. For the sandwich structure, balsa wood is used as the core material. Due to their high cost, carbon fibres are rarely used. Their usage is generally restricted to high loaded parts of the rotor blade as the spar caps. For this material composition, laminating is the favourable manufacturing approach. Laminating is advantageous by adding the possibility to have a different material

composition along the rotor blade. Therefore, the stiffness of the blade can be adjusted in individual regions as desired. Additionally, the automated production of complex geometries of this kind is difficult and involves considerable costs. The disadvantage is that the blade has to be made by hand [3]. The lamination process using a negative form of a rotor blade is shown in **Figure 2-3**.



Figure 2-3 Laminating of a Rotor Blade [3]

2.2 Intelligent Wind Turbine Rotor Blades

The research project „Smart Blades 2” is based on the results of the foregoing research project “Smart Blades”. For the in chapter 1 introduced technologies different research statuses were achieved. The most important research results for the technology 1 and 2 are outlined in the following and are the basis for on-going investigations.

For „Technology 1“, the passive rotor blades, both a geometric bending-torsion coupling (GBTK) and a structural bending-torsion coupling (SBTK) were investigated. Both technology types were designed for the in chapter 4 introduced reference wind turbine. For the geometrical bending-torsion coupling, the concept

of pre-deformation of the blade was pursued, which counteracts deformation under load. The structural bending-torsion coupling was implemented through an anisotropy of the fiber layers, leading to different induced twist along the blade. Induced twist results from forces acting on the rotor blade in loaded states, inducing a torsion, resulting in a change of the angle of attack along the blade. Various CFD simulations of the adapted GBTK rotor blade and the adapted SBTK rotor blade have shown that both technology types are leading to a load reduction compared to the reference rotor blade. Overall, the GBTK led to a greater load reduction than the SBTK. To generalize the achieved results, a different rotor blade was designed and further verified by simulations. This rotor blade was a 20 m long rotor blade with implemented GTBK as the expected load reduction in comparison to the SBTK was greater. These advanced simulations supported the results previously obtained. Furthermore, the results for this rotor blade shall be experimentally verified by a prototype in the upcoming “Smart Blades 2” project [4]. Overall, the investigations on the reference rotor blade using GBTK resulted in a relative load reduction of the extreme and fatigue loads of several percent. In comparison, the SBTK only lead to a relative load reduction lower than 1 %. In the follow-up project “Smart Blades 2”, the SBTK is in focus. The reason for this is that the outer shape and thus the aerodynamic properties of the blade do not have to be changed in comparison to the GBTK. Further concepts for the implementation of the SBTK to increase the achieved load reduction are to be developed here [4].

For „Technology 2“, the active rotor blades with trailing edge flap, extensive parameter studies with aerodynamic simulations regarding the flap properties were carried out for the reference rotor blade. The results are the flap length, the flap end position, the flap depth and the flap profiles. With the help of further simulations, the load reduction by the trailing edge flap could be verified. Here, a 2 m long demonstrator was manufactured and is going to be tested in “Smart Blades 2” [4]. **Figure 2-4** shows the demonstrator flap used for the described prototype blade.



Figure 2-4 „Technology 2“ Flap Demonstrator [5]

Furthermore, the complete prototype blade installed at a test rig is shown in **Figure 2-5**.



Figure 2-5 Technology 2 Test Rig with installed Prototype [5]

In the "Smart Blades 2" project, an overall structural design of the reference rotor blade with trailing edge flap is aimed at. The effects of the trailing edge on the entire blade are to be analyzed with regard to structural, aerodynamic parameters.

3 Approaches of the Research Topic Smart Blades 2

In the “Smart Blades 2” project, different approaches for the load reduction on a rotor blade are investigated. These approaches are based on the results achieved in the “Smart Blades 1” project as previously described in chapter 2.2. This thesis is focusing on two technologies. First, the integration of bending torsion coupling by using SBTk and second the integration of active control elements in form of a flap at the trailing edge.

The bending torsion coupling is part of the „Technology 1“ research package in “Smart Blades 2”. It is also commonly known as aeroelastic tailoring. The core idea of this concept is to passively control the induced twist in the blade under bending conditions. Induced twist results from forces acting on the rotor blade in loaded states, inducing a torsion, resulting in a change of the angle of attack along the blade. In normal operation conditions, the blade is bending due to the dynamic pressure of the wind as well as the acting lift and drag forces on the blade. The acting aerodynamic forces are shown in **Figure 3-1**. It shall be noted, that the low-pressure side of the airfoil is orientated towards the tower for the reference turbine, as it is an upwind turbine.

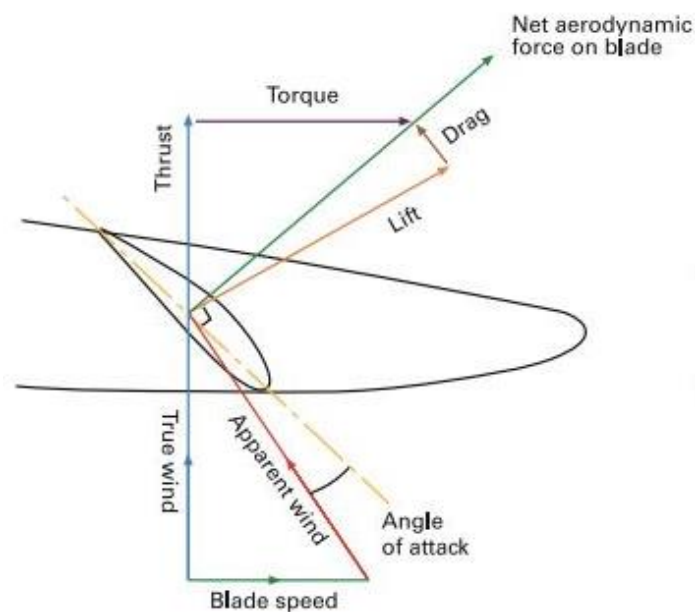


Figure 3-1 Aerodynamic Forces acting on a Rotor Blade [6]

The incoming velocity as well as the angle of attack on an aerodynamic airfoil of the rotor blade is dependent on two wind speeds. The “True wind” indicates the wind. The induced wind speed is created by the rotation of the rotor, the “Blade speed”. The “Apparent wind” is the product of both components. The arising aerodynamic forces on the blade, namely the “Lift” and “Drag” are creating the “Torque” which drives the rotor of the wind turbine. The “Thrust” force is parallel to the wind, thus leading to the bending of the blade in wind direction. Aeroelastic tailoring is therefore an effective concept for load reduction, as the driving force (the bending of the blade) exists in all power production states of the wind turbine. The load reduction itself is achieved by the induction of twist. The induced twist leads to a different angle of attack along the blade. The aerodynamic lift coefficient c_l and the drag coefficient c_d , resulting in the lift force F_L and the drag force F_D , see equation (3-1) and (3-2), are dependent on the Angle of attack.

$$F_L = \frac{1}{2} \rho v^2 S c_l \quad (3-1)$$

$$F_D = \frac{1}{2} \rho v^2 A c_d \quad (3-2)$$

Different lift and drag forces are therefore the result of altered angle of attacks. As mentioned previously, the product of both forces is resulting in the torque and the thrust acting on the rotor. From a structural point of view, the reduction of those forces is leading to lower required stiffness's and strengths of the blade as the aerodynamic loads are lowered. From an aerodynamic and efficiency point of view, the reduction of the thrust acting on the blade is also desired, as the thrust has no beneficial effect. However, the relationship between thrust and torque leads to the conclusion, that the thrust acting on the blade cannot be reduced without an altered torque. Therefore, aeroelastic tailoring has an impact on the aerodynamic efficiency as well as the overall produced torque of the blade. For this reason, the optimal aerodynamic design of the blade may differ from the optimal structural design.

The „Technology 2“ of “Smart Blades 2”, which bases on an active flap at the trailing edge towards the tip of the blade, works similar. The flap itself is definable

as an additional airfoil replacing the trailing edge of the blade airfoil. This flap airfoil is creating additional drag and lift forces dependent on its angle of attack. The resulting aerodynamic forces on the rotor blade become actively controllable by the forces added from the flap. Therefore, the overall produced torque and thrust are variable. Thus, the controlling of the flap is leading to minimized (or maximized) loads on the structure.

The advantage of this concept in contrast to aeroelastic tailoring is that the angle of attack of the flap actively controls the aerodynamic forces of the blade. Due to being passive, the aerodynamic impact of aeroelastic tailoring cannot be dynamically changed, but is given by the structural design. The disadvantage of the active controlled flap is the complexity it adds to the blade. On one hand, the increased structural requirements, as the flap has no benefits to the structure strength and stiffness and on the other hand the required controller of the flap. Therefore, the decrease of the structures mass by the achieved load reduction must be greater than the added weight by the additional components by the flap installation.

4 Reference Wind Turbine

The reference wind turbine for the “Smart Blades 2” project is the IWT-7.5-164. The rotor of the turbine has a diameter of 164 *m* and the maximum produced electric power is 7.5 *MW* [7].

The partaking institutes of the research association designed this turbine. It reflects the up-to-date standards of modern wind turbines in point of view of electrical, control and aerodynamic design. Due to the research focus on rotor blades of the project, special attention is paid towards the design of the rotor blades. The leading designer of the wind turbine, the IWES institute, created the reference structural design of the rotor blade. The IWES institute itself is also contributing to the aerodynamic and aeroelastic investigations on the rotor blade [8].

Due to being a virtual design concept, there is no prototype turbine. In the **Figure 4-1** below, the wind turbine is shown in an aerodynamic simulation environment.

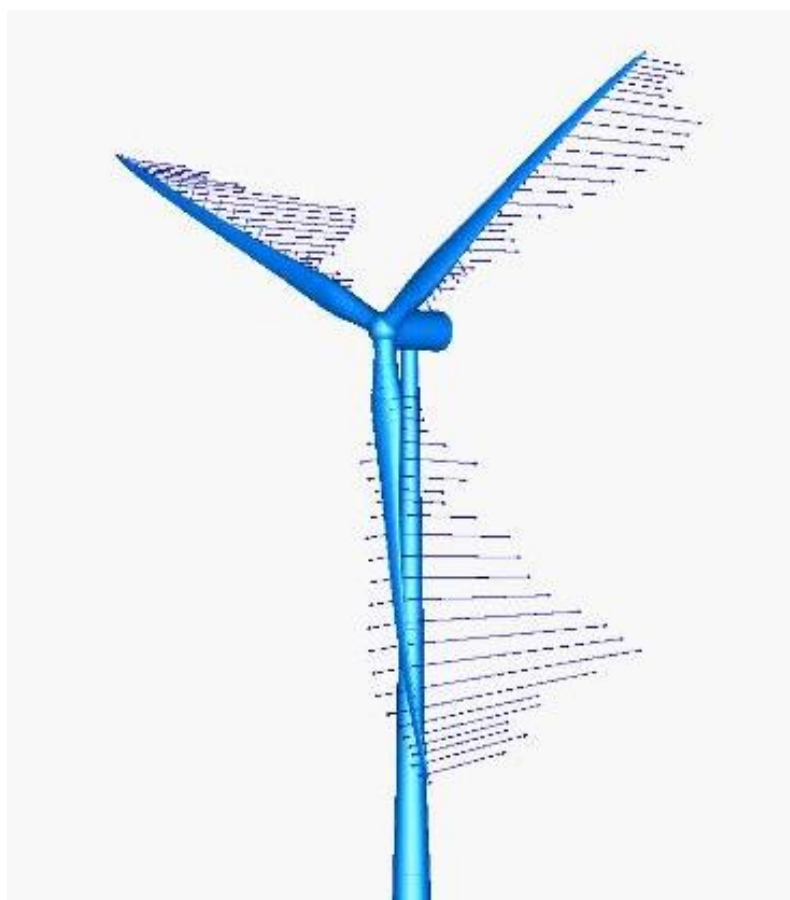


Figure 4-1 IWT-7.5-164 Reference Wind Turbine [8]

The power curve of the reference wind turbine is shown in **Figure 4-2**. The power curve displays the produced electrical power of the wind turbine against the wind speed. The cut-in wind speed, the speed where the turbine starts producing electrical power, is 3 m/s . The cut-out wind speed where the turbine is shut down to prevent structural damage is $> 25 \text{ m/s}$.

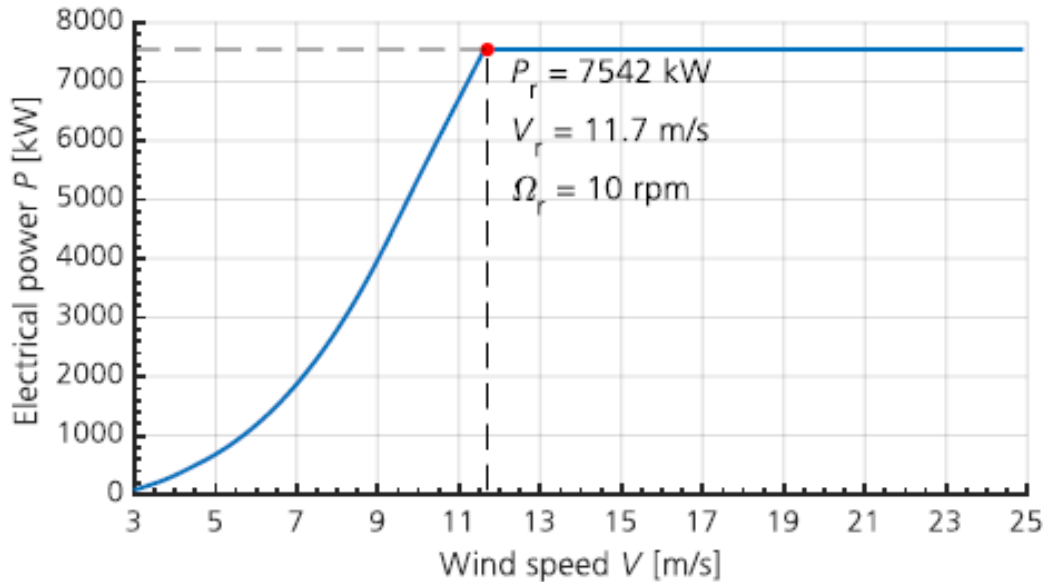


Figure 4-2 Power curve of the IWT-7.5-164 [7]

As indicated from the figure, the maximum electrical produced power is 7542 kW . This electrical power is produced starting at a wind speed of 11.7 m/s and a rotational speed of 10 RPM . At greater wind speeds, the electrical output of the turbine stays constant. It does not make sense from a cost point of view to further increase the electrical power produced for these wind speeds, as these occur very rarely. The power curve of a wind turbine in general is dependent on many factors, including aerodynamic boundary conditions as the air density. The air density for the displayed power curve is $\rho_{Air} = 1.225 \text{ kg/m}^3$.

The rotor blade of the IWT-7.5-164 is designed to aerodynamic standards. The total length of the rotor blade is $l_{blade} = 80 \text{ m}$. The blade has a pre-twist starting from roughly $\theta_{twist} = +16.7^\circ$ at the blade root to up to $\theta_{twist} = -1^\circ$ at the blade tip. A negative pre-twist angle indicates the creation of a higher angle of attack of the airfoil section, see **Figure 4-3**.

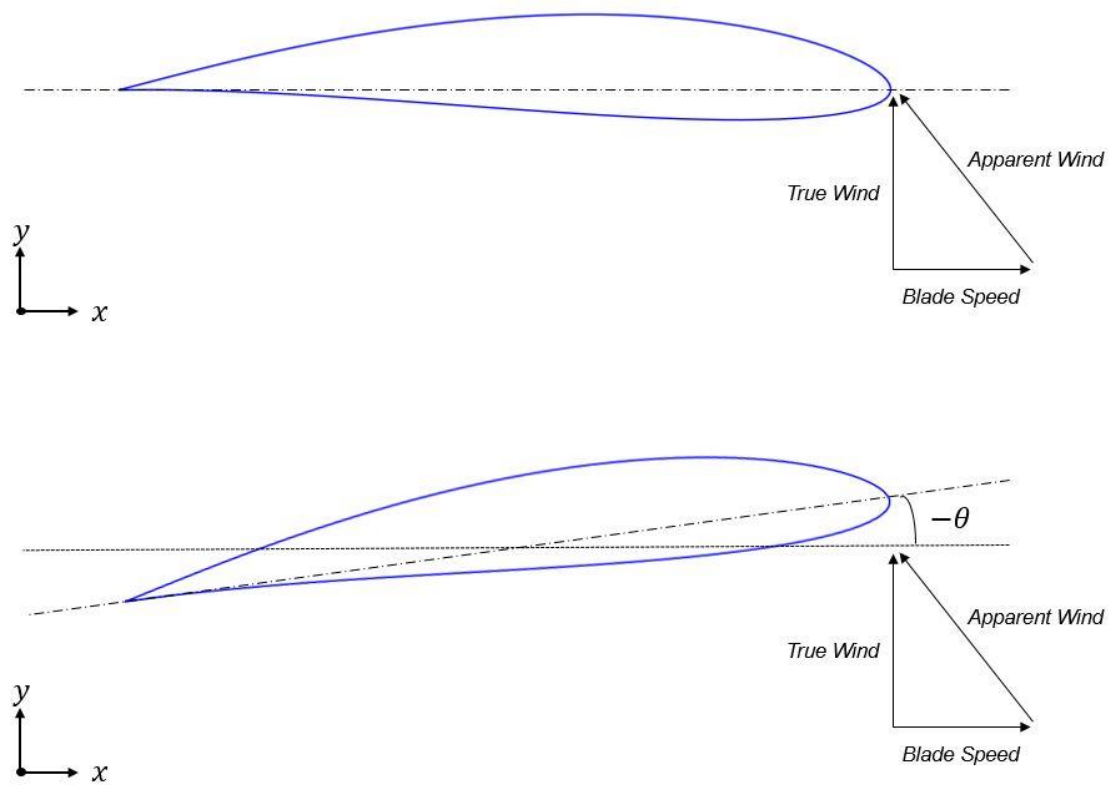


Figure 4-3 Negative Pre-Twist Angle [9]

The pre-twist allows each airfoil to operate at its most efficient aerodynamic work point. The **Figure 4-4** shows the pre-twist of the rotor blade along the radial position.

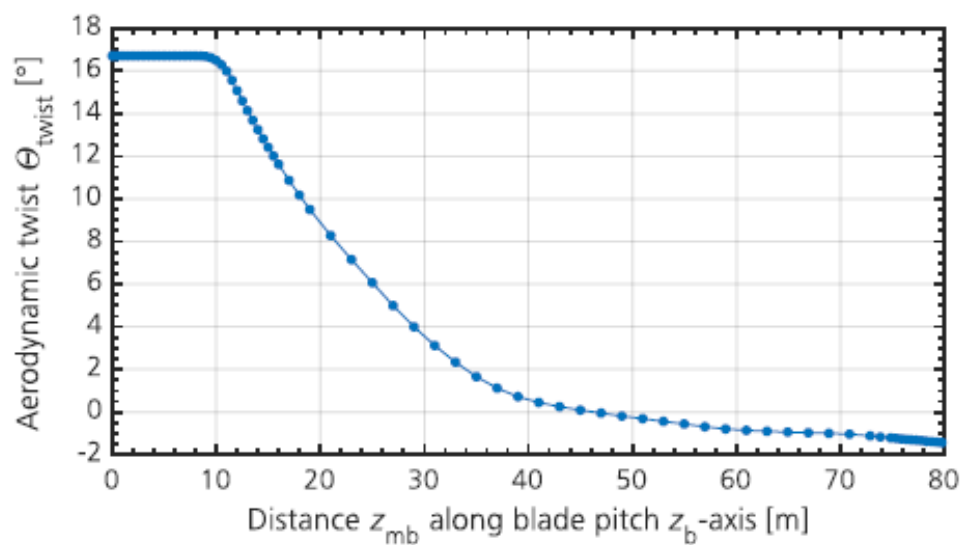


Figure 4-4 Pre-Twist of the IWT-7.5-164 Rotor Blade [10]

The pre-bend of the rotor blade is up to $e_{pb} = -4\text{ m}$ at the blade tip. This results in a total tower clearance of 22.995 m for the tip of the blade including the pre-cone of the shaft. A pre-bend against the wind direction lowers the structural requirements. The structural requirements for the bending strength in wind direction are derived from the minimum allowable tower clearance of the rotor blade to the tower of the wind turbine. A pre-bend, which further increases the clearance to the tower in the unloaded state, is therefore preferable. The pre-bend against the radial position of the rotor blade is shown by the red line e_{pb} in **Figure 4-5**. The blue line c displays the chord length against the radial position.

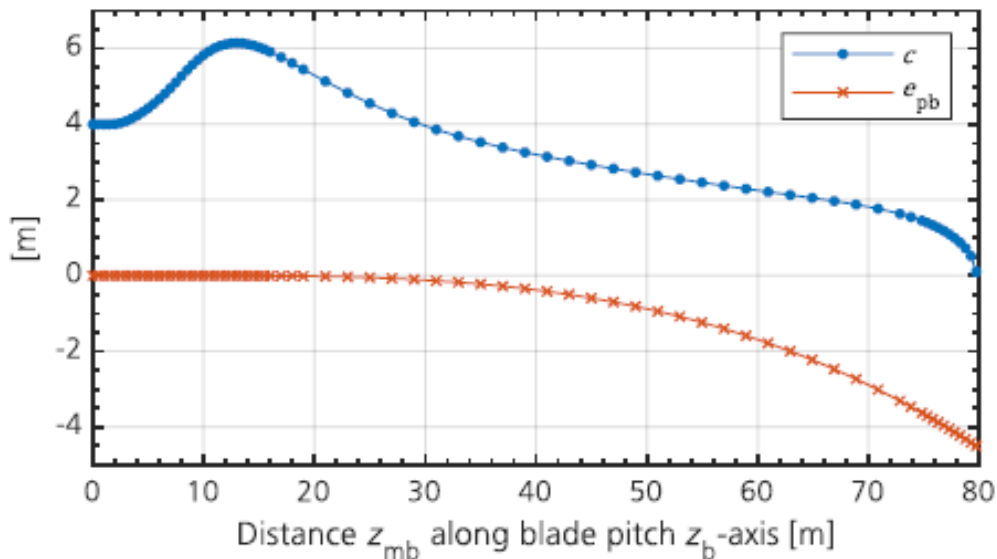


Figure 4-5 Pre-Bend of the IWT-7.5-164 Rotor Blade [10]

The detailed structural design of the rotor blade including the spar distributions is further described in chapter 6.1.

5 Structural Requirements

The structural design process of wind turbine rotor blades is strictly following engineering standards. For the assessed technologies, two different guidelines have to be considered: The IEC-61400 that is most commonly used along all wind turbine manufacturers and the DNVGL-ST-0376. Both engineering standards are describing a standardized approach for designing parts of a wind turbine. The guidelines may have similar regulations, which have to be fulfilled in order to achieve certification. For the design process, the stricter regulation of both norms is applied to enable a certification for both engineering standards. The following chapter is outlining the most important design rules in terms of structural design, which are considered in the structural sizing process.

5.1 Engineering Standards

The **Table 5-1** on the next page is showing all applied regulations from the engineering standards. The shown regulations are extracted from the chapters of the guidelines regarding the structural design of rotor blades. Further regulations, for example regulations for loads, are not assessed. These regulations are considered in other sub processes used in the structural design process. The calculation of the represented reduction and safety factors for the regulations is described in chapter 5.2.

Table 5-1 Applied Engineering Standards [8], [9]

| <u>Category</u> | <u>Guideline</u> | <u>Description</u> | <u>Value</u> |
|----------------------------------|------------------|--|--|
| Deflection | IEC-61400 | It shall be ensured that the rotor of the turbine does not collide with the tower or other parts of the wind turbine. A deformation analysis shall be performed for the relevant tower clearance load case. | Maximal Flapwise Deflection: 11.9 m (Equivalent maximal deflection from DNVGL-ST-0376: 16 m) |
| Fiber Failure | DNVGL-ST-0376 | For the verification of fiber failure, the fiber values of the used material shall be reduced by a reduction factor γ_{mFF} . | $\gamma_{mFF} = 2.26512$ (Equivalent reduction factor from IEC-61400: $\gamma_{mFF} = 1.1$) |
| Inter-Fiber Failure (IFF) | DNVGL-ST-0376 | The blade laminate shall be verified for inter-fiber failure. It shall be demonstrated by analysis that IFF does not occur for the serviceability limit state loads envelope for each individual layer of laminate. Failure to be considered includes IFF caused by in-plane transversal tensile or compressive stresses, by in-plane shear stresses, or a combination of these. The failure criterion shall be Puck or Larc03. The fiber values of the used material shall be reduced by a reduction factor γ_{mIFF} . | $\gamma_{mIFF} = 1.518$ |
| Stability | DNVGL-ST-0376 | All parts of the blade shall be verified for buckling failure and localized instability. Analytical or numerical methods can be used. The fiber values of the used material shall be reduced by a reduction factor γ_{mStab} . | $\gamma_{mStab} = 1.53$ (Equivalent reduction factor from IEC-61400: $\gamma_{mStab} = 1.53$) |
| Stress / Strain | DNVGL-ST-0376 | For the verification of allowable stresses and strains of the material, the fiber values shall be reduced by a reduction factor. The reduction factor applies corresponds to the reduction factor for fiber failure. | $\gamma_{mFF} = 2.26512$ (Equivalent reduction factor from IEC-61400: $\gamma_{mFF} = 1.1$) |

5.2 Safety Factors

The represented reduction and safety factors from **Table 5-1** are extracted from the applied guidelines. The guidelines are outlining a strict procedure for the calculation.

For the assessment of the maximal allowed deflection of the blade accordingly to the IEC-64100, three different partial safety factors have to be considered [11]. The partial safety factors are then multiplied by each other to achieve the overall safety factor γ_S , which has to be used in the design process. Generally, each partial safety factor is used only for its special application case, e.g. the partial loads safety factor only for the loads analysis. By using a multidisciplinary design process, the combination of all safety factors is assessed as acceptable. Equation (5-1) is showing this context.

$$\gamma_S = \gamma_f * \gamma_m * \gamma_n \quad (5-1)$$

where:

| | |
|------------|---|
| γ_f | Partial safety factor for loads |
| γ_m | Partial safety factor for materials |
| γ_n | Partial safety factor for consequences of failure |

A value of $\gamma_S = 1.9305$ follows for the safety factor, see equation (5-2). This leads to the allowable maximum flapwise deflection of the blade as the requested minimum tower clearance in the guideline is described by no collisions between any parts. By dividing the maximal tower clearance available by the considered safety factor, the maximum allowed deflection is assessed, see equation (5-3).

$$\gamma_S = 1.35 * 1.1 * 1.3 = 1.9305 \quad (5-2)$$

$$l_{maxDeflection} = 22.995 \text{ m} / 1.9305 = 11.9 \text{ m} \quad (5-3)$$

In contrast, the procedure of the DNVGL-ST-0376 is based on partial reduction factors for each design criterion. These partial reduction factors are then combined to achieve an overall reduction factor for the material for each criterion. The overall reduction factor is assessed using the equation (5-4) [12].

$$\gamma_m = \gamma_{m0} * \gamma_{mc} * \gamma_{m1} * \gamma_{m2} * \gamma_{m3} * \gamma_{m4} * \gamma_{m5} \quad (5-4)$$

where:

| | |
|---------------|---|
| γ_{m0} | Base factor |
| γ_{mc} | Partial reduction factor for criticality of failure mode |
| γ_{m1} | Partial reduction factor for environmental degradation |
| γ_{m2} | Partial reduction factor for temperature effects |
| γ_{m3} | Partial reduction factor for manufacturing effects |
| γ_{m4} | Partial reduction factor for the accuracy of analysis methods |
| γ_{m5} | Partial reduction factor for the accuracy of load assumptions |

For the reduction factor for fibre failure $\gamma_{m_{FF}}$ follows via equation (5-5):

$$\gamma_{m_{FF}} = 1.2 * 1.1 * 1.2 * 1.1 * 1.3 * 1 * 1 = 2.265 \quad (5-5)$$

Furthermore, for the reduction factor for inter-fibre failure $\gamma_{m_{IFF}}$ follows via equation (5-6):

$$\gamma_{m_{IFF}} = 1.2 * 1 * 1.1 * 1 * 1 * 1.15 * 1 = 1.518 \quad (5-6)$$

Lastly for the reduction factor for stability $\gamma_{m_{Stab}}$ follows via equation (5-7):

$$\gamma_{m_{Stab}} = 1.2 * 1.1 * 1 * 1.05 * 1.05 * 1.05 * 1 = 1.53 \quad (5-7)$$

The values for the partial reduction factors are extracted from the named guideline. As mentioned in **Table 5-1** the reduction factor for the stress and strain criteria is equal to the reduction factor for fibre failure $\gamma_{m_{FF}}$.

The described safety and reduction factors are integrated in an automated structural design process. The integration of these values as well as the analysis criteria are further described in chapter 6.2.4.

6 Methodology

The design and optimization process of the blades structure is transcribed by an automated design process. This chapter gives an overview about the different sub processes, which form the optimization process. The assembled processes for the technologies, based on the introduced sub processes, are explained in chapter 6.4 and 6.5.

6.1 FE Model

The FE model, which is used in the structural sizing and design process, is based on a parametric CPACS file. A CPACS file includes the necessary information for creating a FE models. CPACS is developed by the DLR and mostly used for aviation purposes [13]. For the FE shell model of the rotor blade the file includes the following structural information's:

- 30 airfoil profiles along the radial position of the blade including the pre-twist
- Position and number of the spars as well as their course throughout the blade
- Shell thickness and material parameters
- Position and connection points of RBE elements
- Applied load cases to the structure

The DLR-FA internal tool “DELiS” is building the FE shell model from the parametric file for further usage in FE calculation tools [14]. From the 30 given airfoils and their radial position, the outer shell of the blade is built by interpolation, see **Figure 6-1** and **Figure 6-2**.



Figure 6-1 Plan View on the FE Model of the Rotor Blade



Figure 6-2 Side View on the FE Model of the Rotor Blade

The rotor blades of the IWT-7.5-164 are built in a multiple spar approach. The spars in the blade, which are created from the parametric file, are defined by their position along the blade. Each positional definition is described by a point. This point has two coordinates: the radial position and the chordwise position as relative values of the total length of the blade and the local chord length. The two main spars, also known as the rear and the front spar, see **Figure 6-3 (1)** and **(2)**, are defined by two positional definitions. An endpoint and a start point of the spar. The given points are connected by linear interpolation between the two positions. The third spar, which is positioned at the trailing edge, see **Figure 6-3 (3)**, consists of three positional definitions, as its progression is subjected to a change. The course of the spars is adaptable by changing the existing positional definitions or by adding additional definitions. This enables an individual spar design for different structural layouts and is further used and explained in the different structural concepts. **Figure 6-4** shows the spars from the side view.

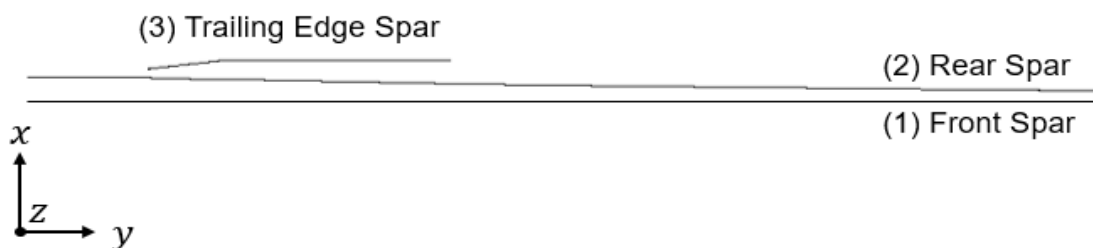


Figure 6-3 Plan View on the Spars in the FE Model



Figure 6-4 Side View on the Spars in the FE Model

Furthermore, RBE elements are integrated into the model and the defined surrounding nodes are connected to them, see **Figure 6-5**. The surrounding nodes are defined from the 30 airfoils used in the creation of the shell model. This leads to 30 RBE elements for the blade overall. The blue lines in the figure are showing the connection of surrounding nodes to the RBE element. The RBE elements are used to introduce loads to certain parts of the FE model, by using a reference node (the RBE element). The reference node defines the resulting displacement by loads of the connected nodes. This procedure allows interrupting complex loads on individual single RBE node loads.

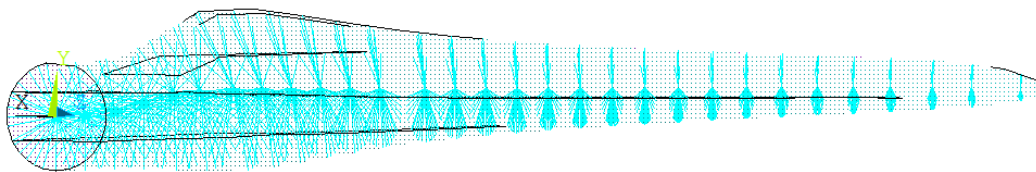


Figure 6-5 Dynamic View on the RBE Elements in the FE Model of the Rotor Blade

6.2 Structural Sizing

For the sizing of the structure with glass fibre materials the program Hypersizer is used as a basic. Hypersizer, originally developed by NASA [15], sizes a structure by using a defined material library and furthermore given loads. By using defined criteria's, described in chapter 5.1, the shell model is analysed, the best material combination for the structure is obtained and the margins of safety are

assessed. The optimization objective of Hypersizer is the mass of the structure [15]. Hypersizer is integrated into a sizing process, which iteratively sizes the structure by updating a parameter space and set.

6.2.1 Iterative Sizing

The sizing process in Hypersizer is extended by an outer iterative sizing loop. The maximum and minimum thickness of the sized assemblies must be defined in Hypersizer. This given thickness is the parameter space Hypersizer is working with next to different glass fibre laminates. The iterative sizing loop analyses the margins of safety obtained from the sizing in Hypersizer. Based on the results, the allowed thicknesses are adapted and the new iteration starts with different boundaries for the thickness. This is leading to the lowest possible mass for the complete structure while reducing the required sizing time. Furthermore, the iterative sizing is required for the adaptation of the maximum deflection of the blade. This is further described in chapter 6.2.4. Next to the deflection criterion, the process uses the margins of safety as well as the achieved difference in mass between iterations to assess the convergence of the process.

6.2.2 Material

Hypersizer is based on a material library for the glass fibre lamina. This library includes all relevant material properties needed for the sizing:

- The given stiffness against tension (E_{t1}), the allowed stresses through tension (F_{tu1}) and the allowed strain through in-plane tension (e_{tu1}) in 0 degree direction of the laminate
- The given stiffness against tension (E_{t2}), the allowed stresses through tension (F_{tu2}) and the allowed strain through in-plane tension (e_{tu2}) in 90 degree direction of the laminate
- The given stiffness against compression (E_{c1}), the allowed stresses through compression (F_{cu1}) and the allowed strain through in-plane compression (e_{cu1}) in 0 degree direction of the laminate

- The given stiffness against compression (E_{c2}), the allowed stresses through compression (F_{cu2}) and the allowed strain through in-plane compression (e_{cu2}) in 90 degree direction of the laminate
- The given stiffness against in-plane shear (G_{12}), the given stiffness against interlaminar shear (G_{13} and G_{23}), the allowable stress through in-plane shear (F_{su12}) and the allowable strain through in-plane shear (e_{su12})
- The Poisson's ratio ν_{12}
- The density ρ of the material

The coordinate system of a lamina is strictly defined, see **Figure 6-6**. The index 1 is equivalent to the 0 degree direction of the lamina, the index 2 to the 90 degree direction and the index 3 to the perpendicular direction of the fibres. The above introduced abbreviations are according to this definition.

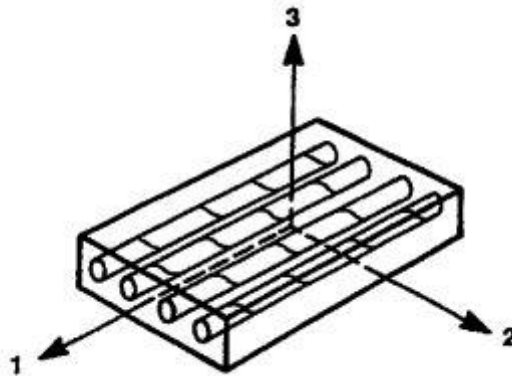


Figure 6-6 Lamina directions [16]

From the given material properties, Hypersizer formulates the stiffness matrix of a laminate. The stiffness matrix is determined by using the classic laminate theory. For each layer of the laminate, the stress-strain relations are defined via equation (6-1) [16].

$$\begin{bmatrix} \sigma_1 \\ \sigma_2 \\ \tau_{12} \end{bmatrix} = \begin{bmatrix} Q_{11} & Q_{12} & 0 \\ Q_{12} & Q_{22} & 0 \\ 0 & 0 & Q_{66} \end{bmatrix} \begin{bmatrix} \varepsilon_1 \\ \varepsilon_2 \\ \gamma_{12} \end{bmatrix} \quad (6-1)$$

where:

$$Q_{11} = \frac{E_1}{1 - \nu_{12}\nu_{21}} \quad Q_{22} = \frac{E_2}{1 - \nu_{12}\nu_{21}} \quad Q_{12} = \frac{\nu_{12}E_2}{1 - \nu_{12}\nu_{21}} \quad Q_{66} = G_{12}$$

E_1 matches the given E_{t1} or E_{c1} depended on the direction of the stress. The same applies to E_2 for E_{t2} and E_{c2} . The terms Q_{13} and Q_{23} are set to zero, as a layer is analysed as an orthotropic material in its plane stress state. This consideration is recognized with regard to individual layers of the laminate. The assumption of plane stress for single plies is widely spread. A single ply is only able to withstand high forces in its plane directions. A force in perpendicular direction of the plane cannot be intercepted by the ply, as there are no fibres in that direction. Therefore, the stiffness's of the ply in its perpendicular direction are neglect able low, which allows the definition of a ply in a plane stress state [16]. For the stiffness matrix of the laminate it is further assumed, that each lamina of the laminate is perfectly bonded to one another, that the bonds are infinitesimally thin and non-shear-deformable. Therefore, the resulting laminate can be considered as one layer [17].

The forces and moments acting on the complete laminate are derived by the integration of the stresses in each layer, see equation (6-2) and (6-3) [18].

$$N_{x/y/xy/yx} = \int_{-t/2}^{t/2} \sigma_{x/y/xy/yx} dz \quad (6-2)$$

$$M_{x/y/xy/yx} = \int_{-t/2}^{t/2} \sigma_{x/y/xy/yx} z dz \quad (6-3)$$

where:

| | |
|----------------------|--|
| $N_{x/y/xy/yx}$ | Force per unit width of the cross section of the laminate in all directions |
| $M_{x/y/xy/yx}$ | Moment per unit width of the cross section of the laminate in all directions |
| $\sigma_{x/y/xy/yx}$ | Acting stresses in all directions |
| t | Thickness of the layer |
| z | Distance of the layer to the middle surface of the laminate |

Figure 6-7 and **Figure 6-8** are indicating the introduced forces N and M acting on a flat laminate in the different directions.

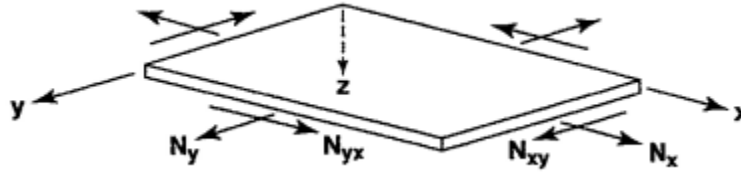


Figure 6-7 In-Plane Forces on a Flat Laminate [18]

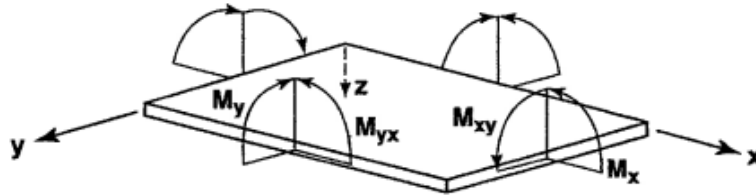


Figure 6-8 Moments on a Flat Laminate [18]

The equations (6-2) and (6-3) are equal to the formulation (6-4) and (6-5) [18].

$$\begin{bmatrix} N_x \\ N_y \\ N_{xy} \end{bmatrix} = \sum_{k=1}^N \begin{bmatrix} \bar{Q}_{11} & \bar{Q}_{12} & \bar{Q}_{16} \\ \bar{Q}_{12} & \bar{Q}_{22} & \bar{Q}_{26} \\ \bar{Q}_{16} & \bar{Q}_{26} & \bar{Q}_{66} \end{bmatrix}_k \left[\int_{z_{k-1}}^{z_k} \begin{bmatrix} \varepsilon_x^0 \\ \varepsilon_y^0 \\ \gamma_{xy}^0 \end{bmatrix} dz + \int_{z_{k-1}}^{z_k} \begin{bmatrix} \kappa_x \\ \kappa_y \\ \kappa_{xy} \end{bmatrix} z dz \right] \quad (6-4)$$

$$\begin{bmatrix} M_x \\ M_y \\ M_{xy} \end{bmatrix} = \sum_{k=1}^N \begin{bmatrix} \bar{Q}_{11} & \bar{Q}_{12} & \bar{Q}_{16} \\ \bar{Q}_{12} & \bar{Q}_{22} & \bar{Q}_{26} \\ \bar{Q}_{16} & \bar{Q}_{26} & \bar{Q}_{66} \end{bmatrix}_k \left[\int_{z_{k-1}}^{z_k} \begin{bmatrix} \varepsilon_x^0 \\ \varepsilon_y^0 \\ \gamma_{xy}^0 \end{bmatrix} z dz + \int_{z_{k-1}}^{z_k} \begin{bmatrix} \kappa_x \\ \kappa_y \\ \kappa_{xy} \end{bmatrix} z^2 dz \right] \quad (6-5)$$

where:

| | |
|--------------------|---|
| N | Total number of layers |
| $[\bar{Q}_{ij}]_k$ | Transformed stiffness's of layer k |
| z_k | Distance of the layer k to the middle surface of the laminate |

The transformed stiffness's of layer k , $[\bar{Q}_{ij}]_k$, are only dependent on the in equation (6-1) introduced stiffness's Q_{ij} of the layer and the angle θ . The angle θ describes the difference of the layer coordinate system, see **Figure 6-6**, to the laminate coordinate system, see **Figure 6-7**. This context is shown in **Figure 6-9**.

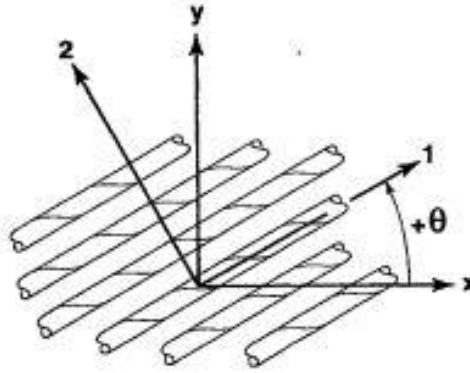


Figure 6-9 Layer Angle in Comparison to the Laminate Angle [16]

Finally, the stiffness matrix-force correlation of the complete laminate is described via (6-6) and (6-7) [18].

$$\begin{bmatrix} N_x \\ N_y \\ N_{xy} \end{bmatrix} = \begin{bmatrix} A_{11} & A_{12} & A_{16} \\ A_{12} & A_{22} & A_{26} \\ A_{16} & A_{26} & A_{66} \end{bmatrix} \begin{bmatrix} \varepsilon_x^0 \\ \varepsilon_y^0 \\ \gamma_{xy}^0 \end{bmatrix} + \begin{bmatrix} B_{11} & B_{12} & B_{16} \\ B_{12} & B_{22} & B_{26} \\ B_{16} & B_{26} & B_{66} \end{bmatrix} \begin{bmatrix} \kappa_x \\ \kappa_y \\ \kappa_{xy} \end{bmatrix} \quad (6-6)$$

$$\begin{bmatrix} M_x \\ M_y \\ M_{xy} \end{bmatrix} = \begin{bmatrix} B_{11} & B_{12} & B_{16} \\ B_{12} & B_{22} & B_{26} \\ B_{16} & B_{26} & B_{66} \end{bmatrix} \begin{bmatrix} \varepsilon_x^0 \\ \varepsilon_y^0 \\ \gamma_{xy}^0 \end{bmatrix} + \begin{bmatrix} D_{11} & D_{12} & D_{16} \\ D_{12} & D_{22} & D_{26} \\ D_{16} & D_{26} & D_{66} \end{bmatrix} \begin{bmatrix} \kappa_x \\ \kappa_y \\ \kappa_{xy} \end{bmatrix} \quad (6-7)$$

where:

$$A_{ij} = \sum_{k=1}^N (\bar{Q}_{ij})_k (z_k - z_{k-1})$$

$$B_{ij} = \frac{1}{2} \sum_{k=1}^N (\bar{Q}_{ij})_k (z_k^2 - z_{k-1}^2)$$

$$D_{ij} = \frac{1}{3} \sum_{k=1}^N (\bar{Q}_{ij})_k (z_k^3 - z_{k-1}^3)$$

A_{ij} corresponds to the extensional stiffness's, B_{ij} to the bending-extension coupling stiffness's and D_{ij} to the torsional stiffness's [18]. With the strains obtained from a before connected FE tool, Hypersizer is able to calculate the acting stresses and build for each laminate design the corresponding laminate stiffness matrix.

For the IWT-7.5-164 rotor blade, only glass fibre fabrics are used. Fabric materials already include the matrix material, e.g. epoxy resin. These materials are implemented into the material library as effective laminates. When using effective laminates, the discrete stacking of the individual layers is resolved and the effective material properties are displayed in percent of 0° , 90° and $\pm 45^\circ$ layers of the entire laminate. By dissolving the discrete individual layers, the required computing time is significantly reduced by limiting the possible stacking combinations. However, this also means that no direct layer stacking can be derived from the laminate design created. The discrete layer stacking must be verified in a post processing [19].

The effective laminates are commonly differentiated in three different ways: uniaxial, biaxial or triaxial. The uniaxial fabric has all fibres orientated in one direction corresponding to a 0° orientation. Uniaxial material is preferable for regions with homogeneous stresses in a single load direction. Biaxial material further increases the material properties in an additional direction and corresponds to either 0° and 90° or $+45^\circ$ and -45° fibre orientation. Triaxial material combines three fibre orientations and is most commonly used in complex load locations where the load direction and distribution can be described as inhomogeneous or the loads lead to stresses in several directions of the material. Triaxial material

corresponds to $+45^\circ$, -45° and 90° or 0° degree fibre orientation. **Figure 6-10** is showing the different lay-up methods.

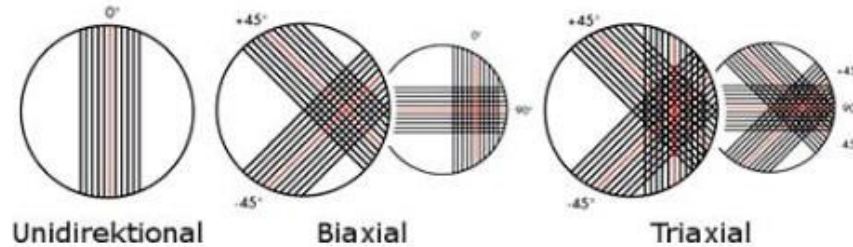


Figure 6-10 Lay-up Methods [20]

In effective laminates, multiple lay-up methods may be combined. Therefore, effective laminates are often described with the percentage amount of each layup type included. For example, a fabric described as “50% uniaxial / 50% biaxial” contains half-uniaxial fibres and half-biaxial fibres. The arising fabric differs in material properties, mainly in terms of stiffness’s in the different directions as well as density, from a fabric using only one fibre direction. The material library used for the sizing process inhibits the following different fabric types:

- 100 % uniaxial, biaxial or triaxial
- x % uniaxial, x % biaxial, where x is ranging from 5 to 95 in 5 % steps
- x % uniaxial, x % triaxial, where x is ranging from 5 to 95 in 5 % steps

This results into a total number of 41 different considered fabrics.

6.2.3 Assemblies and Sections

For the sizing in Hypersizer, the shell model of the blade is divided into different assemblies. In these assemblies, the general design concept, the analysed criteria’s and the allowed materials are defined. Two different design concept are considered for the sizing of the rotor blade. The usage of foam sandwiches, see **Figure 6-11**, and unstiffened ply stacks, see **Figure 6-12**. Foam sandwiches are adding thickness to the structure. This increases the resistance against buckling. In contrast, ply stacks are used at higher loaded regions where the thickness of the ply stacks is sufficient to withstand an instability or buckling.

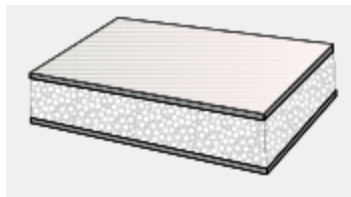


Figure 6-11 Foam Sandwich

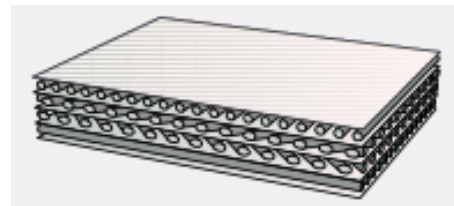


Figure 6-12 Ply Stacks

The IWT-7.5-164 rotor blade is differentiated into the following assemblies:

- Three assemblies for the spars of the blade
- Two assemblies for the trailing edge shell of the blade at the location of the trailing edge spar
- Two assemblies between the front and rear spar, the spar caps
- Four assemblies including the shells next to the spar caps in direction of the trailing and leading edge, the profiling skin

For the introduced assemblies the design concept, as well as the allowed material in Hypersizer differ. A short description of the assemblies and their properties are displayed in **Table 6-1**.

Table 6-1 Hypersizer Assemblies

| <u>Assembly</u> | <u>Description</u> | <u>Design Concept</u> | <u>Allowed Laminates</u> |
|-----------------------------|--|------------------------|--------------------------|
| Spars | <p>The design concept for the spar assemblies is the foam sandwich. The foam sandwiches increase the total area of the spars without adding much weight. This benefits the bending load transmission. The spars are exposed to loads in several directions. This favours the usage of triaxial fabrics.</p> | Foam Sandwich | Triaxial |
| Trailing Edge Shells | <p>The assemblies at the trailing edge are loaded mainly in one direction. In a preliminary design study, it was determined, that uniaxial material in this location is sufficient. The design method is ply stacking.</p> | Unstiffened Ply Stacks | Uniaxial |
| Spar Caps | <p>The spar caps are designed to absorb the forces created by the deflection of the blade. The deflection of the blade is mainly a compression and tension force. Therefore, the allowed material is restricted to uniaxial material. Because the deflection of the blade is leading to high bending forces, the design concept is ply stacking.</p> | Unstiffened Ply Stacks | Uniaxial |
| Profiling Skins | <p>These regions of the blade are responsible for the shape of the blade. The loads are minor compared to other regions. This favours the usage of foam sandwiches. However, due to the inhomogeneous loading of the regions, the material selection is not restricted</p> | Foam Sandwich | All |

All named assemblies are further subdivided into smaller sections or panels. The finer breakdown of the assemblies allows a more optimal material selection for the whole blade, as more parts are designed and analysed. **Figure 6-13** indicates the different defined sections on the outer shell of the blade. The applied design concept and the allowed materials are not affected by this differentiation. Each panel is separately sized by Hypersizer.

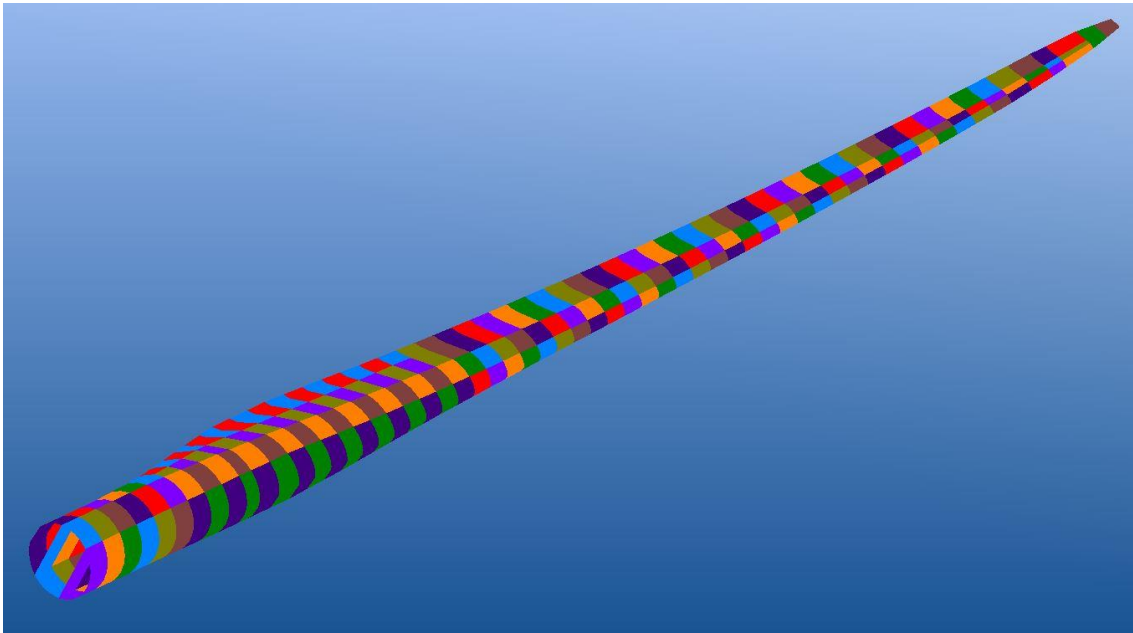


Figure 6-13 Panels in Hypersizer

The blade is subdivided into 60 panels in radial direction from the root to the tip of the blade. The subdivision of the panels in chord position is variable due to the different assemblies and varying local chord lengths.

6.2.4 Analysis Selections and Methods

During the sizing process, the highlighted standards from chapter 5.1 are analysed. For this purpose, various analysis methods that correspond to the criteria of the standards are defined in Hypersizer. The following **Table 6-2** shows the chosen analysis methods in correlation to the engineering standard regulations. The assessed safety and regulation factors are further interpreted as safety factors. Hypersizer is assessing margins of safety for each analysed criterion. These

margins of safety (MoS) are dependent on the safety factor (FoS) as shown in equation (6-8).

$$MoS = \frac{Failure\ Load}{Design\ Load} - 1 = FoS - 1 \quad (6-8)$$

This method simplifies the procedure as the material properties of all fabrics do not need to be altered by the reduction factors resulting from DNVGL-ST-0376.

Table 6-2 Hypersizer Criteria

| <u>Category</u> | <u>Hypersizer Criteria</u> | <u>Description</u> | <u>Margin of Safety</u> |
|----------------------------------|--|---|--------------------------|
| Fiber Failure | Maximum strain in 1 / 2 / 12 direction of the effective laminate | The verification against fiber failure is assessed by the maximum allowable strain of the effective laminate in Hypersizer. | $\gamma_{mFF} = 1.26512$ |
| Inter-Fiber Failure (IFF) | LaRC03 fiber failure / LaRC03 matrix cracking | As proposed in the DNVGL-ST-0376, IFF is assessed by the LaRC03 analysis. | $\gamma_{mIFF} = 0.518$ |
| Stability | Panel Buckling | The stability of the lamina is assessed using the panel buckling criteria. | $\gamma_{mStab} = 0.43$ |
| Stress / Strain | Maximum stress in 1 / 2 / 12 direction of the effective lamina | The stress and strain verification is assessed by further extending the fiber failure analysis for maximum stress in the equal directions (see Fiber Failure). The margin of safety remains the same. | $\gamma_{mFF} = 1.26512$ |

Additionally to the chosen analysis methods, the maximum flapwise deflection of the blade needs to be assessed. Hypersizer offers no option to analyse the deflection of the blade and furthermore restrict it. The iterative sizing process build around Hypersizer uses a workaround for this criterion.

The deflections of the blade are calculated in the FEM tool. The deflection of each FE node in the model is evaluated. By identifying a node, which is located at the low-pressure side of the blade tip. The total flapwise deflection of the blade is measured as the flapwise deflections towards the blade tip are adding up. **Figure 6-14** is showing the outer aerodynamic profile of the blade tip including the corresponding FE Nodes. The node marked by the red arrow is located nearly at the middle of the low-pressure side and depicts the position of the airfoil with the greatest thickness. It is used for the measurement of the total blade deflection.

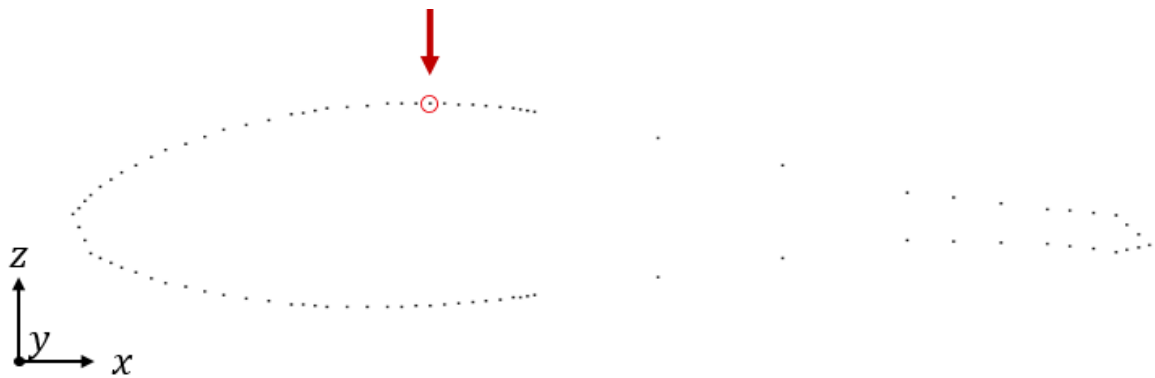


Figure 6-14 Blade Tip Deflection Node

The bending of the blade in wind direction is mostly dependent on the stiffness of the spar caps. The spar caps and the spars are especially designed for the load transmission of bending moments in wind direction, as already mentioned in chapter 2.1. The sized laminate of the spar caps are defined through their stiffness matrix by Hypersizer as described in chapter 6.2.2.

The A_{11} term of the stiffness matrix corresponds to the stiffness in bending direction for the spar caps as the bending force results from tension and compression in fibre direction. While not being able to define allowed deflections of the structure, Hypersizer allows the assignment of to be reached stiffness terms in the stiffness matrix.

The sizing process factorizes the current flapwise deflection $h_{ReachedDeflection}$ with the allowed flapwise deflection $h_{AllowedDeflection}$, resulting from the engineering standards in each iteration, see equation (6-9).

$$a_{Deflection} = \frac{h_{ReachedDeflection}}{h_{AllowedDeflection}} \quad (6-9)$$

The factor $a_{Deflection}$ is multiplied by the $A_{11Current}$ term of the stiffness matrix. The resulting stiffness A_{11new} is set in the next iteration as a constraint, see equation (6-10). As mentioned the target of the stiffness increase are the spar caps.

$$A_{11new} = A_{11Current} * a_{Deflection} \quad (6-10)$$

As a boundary condition for this workaround, it is assumed that the stiffness of the spar caps in their A_{11} direction has a proportional dependency on the flapwise deflection displayed in equation (6-11).

$$A_{11Current} * a_{Deflection} \propto \frac{h_{ReachedDeflection}}{a_{Deflection}} \quad (6-11)$$

Furthermore, the A_{11} stiffness factorization is applied equally to each panel along the radial position of the blade.

6.2.5 Further Development of Adaptive Twist Stiffness

For the investigation on the aeroelastic tailoring of the blade, the assessment of the induced twist by the applied loads is necessary. The induced twist is the design parameter for the aeroelastic tailoring. As described previously, Hypersizer does not include a method for restricting deflections of the blade in different directions.

The iterative process built around Hypersizer is extended not only assessing the induced twist, but also restrict the absolute value of it. The developed approach is based on the deflection analysis described in chapter 6.2.4.

First, the evaluated nodes for the induced twist must be identified. Based on the airfoil profile at the blade tip, the leading and trailing edge nodes are chosen to determine the induced twist, see **Figure 6-15** red arrows.



Figure 6-15 Blade Tip Twist Nodes

From the deflection of the leading and trailing edge node, the induced twist is calculated via the theorem of Pythagoras. In the unloaded state, the difference of the x locations of the nodes form the hypotenuse c of a rectangular triangle, see **Figure 6-16**. It is assumed that the displacement of the nodes to each other in the unloaded state in the z and y direction is negligibly small.

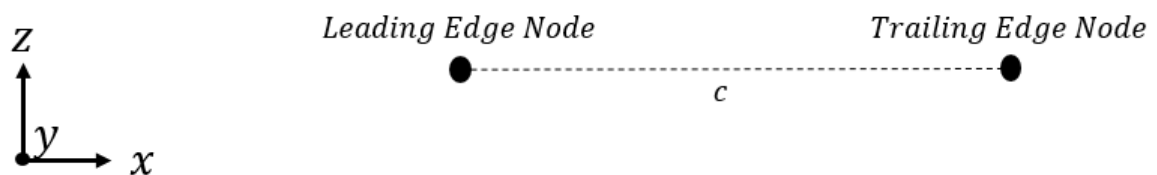


Figure 6-16 Hypotenuse between Leading and Trailing Edge Node

From the deflected positions of the nodes in the loaded state, see **Figure 6-17**, an imaginary third node is created. This node displays the delta of the deflection between the leading and trailing edge node in z direction, see **Figure 6-18**.

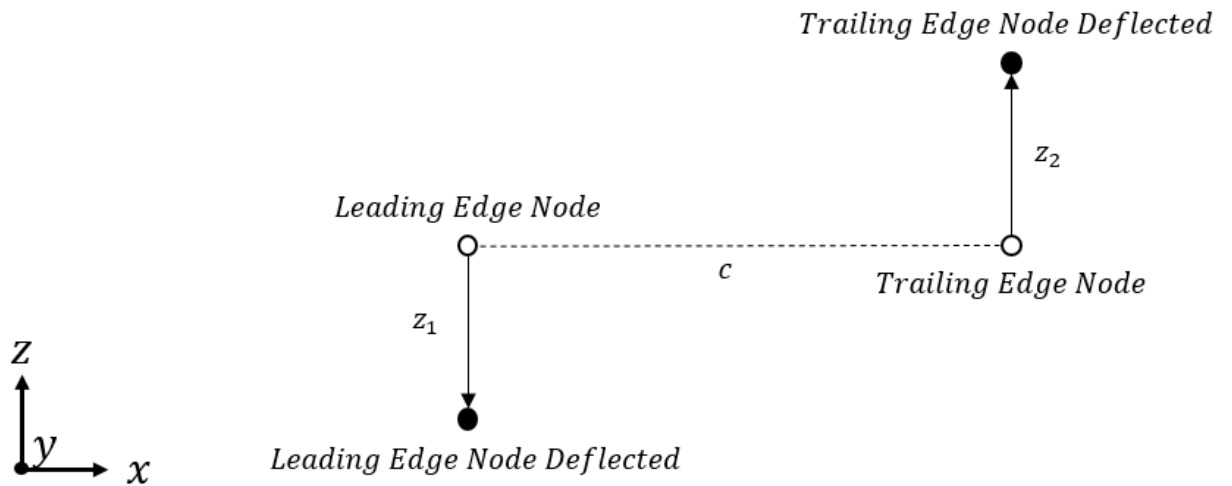


Figure 6-17 Deflected Positions of the Leading and Trailing Edge Node

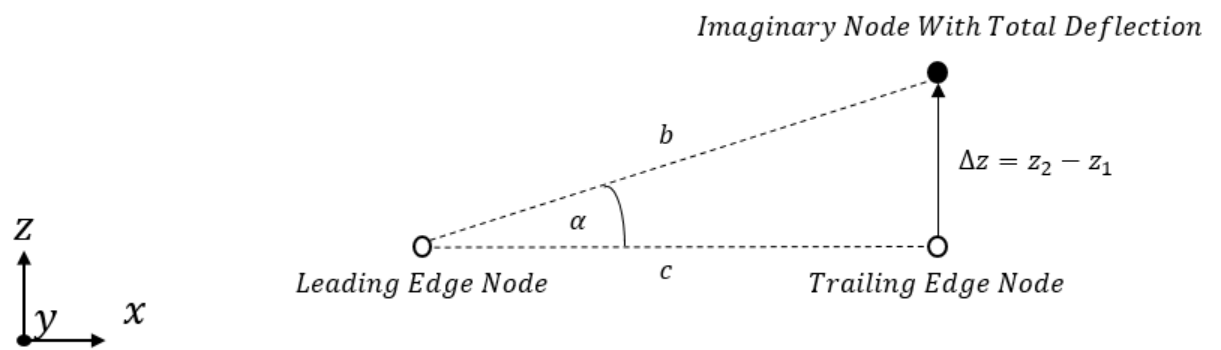


Figure 6-18 Imaginary Node

The indicated angle α in the **Figure 6-18** is then derived from equation (6-12).

$$\alpha = \tan^{-1} \left(\frac{\Delta z}{c} \right) \quad (6-12)$$

The angle α depicts the induced twist at the blade tip. An additional assumption is that the induced twist adds up over the length of the blade. Therefore, the twisting of the blade tip reflects the twisting of the whole blade.

The adaptation of the stiffness of the spar caps, which is used for the deflection criteria, is insufficient for the induced twist criterion. In a preliminary study, it is established that the stiffness against torsion is mainly determined by the profiling skins next to the spar caps. Furthermore, the results of the study are showing, that the A_{11} stiffness is not contributing to stiffness against twisting of the blade. The twist stiffness is mainly dependent on two terms of the stiffness matrix, the A_{66} stiffness value and the D_{66} stiffness value. The A_{66} stiffness value corresponds to the stiffness against shear acting in-plane of the laminate, see **Figure 6-6** 1 – 2 direction. In comparison, the D_{66} stiffness value corresponds to the torsional stiffness in the 1 – 2 direction of the laminate [18] [21].

As the overall goal of the optimization is the reduction of the total mass of the blade, it has to be verified, that the stiffness adaption for the induced twist is optimized in the perspective of mass increase. It is further shown, that the A_{66} stiffness value is more efficient in terms of weight increase than the D_{66} stiffness value. Therefore, the A_{66} stiffness value of the profiling skins next to the spar caps are used to adapt the stiffness against twist. In a similar approach to the assessment of the deflection, the twist stiffness to be reached is evaluated by factorization, see equation (6-13) and (6-14).

$$a_{Twist} = \frac{\alpha_{ReachedTwist}}{\alpha_{AllowedTwist}} \quad (6-13)$$

$$A_{66_{new}} = A_{66_{Current}} * a_{Twist} \quad (6-14)$$

While the deflection criterion uses the approach of adding stiffness equally throughout the blade length, this cannot be verified for the induced twist. The moment of inertia to the shear decreases over the blade. The cross-sectional area to the blade tip decreases due to shorter local chord lengths. Thus, the stiffness against twist decreases towards the blade tip.

This indicates that an increase in stiffness of the stiffness value A_{66} towards the blade tip is more efficient than an even increase in stiffness over the entire blade length. To prove this assumption, a further study is performed with two parameters:

- Usage of an equation for the relative application of the twist stiffness factor, leading to an increase of the twist stiffness towards the tip of the blade
- The radial start position of the stiffness increase
-

Various equations are established for the application of the stiffness increase factor.

- A static or equal distribution of the stiffness increase $f(x) = 100$
- A linear distribution $h(x) = 1.67 * x$
- A quadratic distribution $p(x) = 0.0275 * x^2 - 0.023$
- A logarithmic distribution $g(x) = 24.42 * \log(x)$
- An e distribution $t(x) = 8.7565 * 10^{-25} * e^x$

The variable x indicates the radial position along the blade through the panel numbers. As mentioned previously, the blade is divided into 60 panels in its radial direction. Therefore, the 60th panel is depicting the total blade length of 80 m. The equations are shown in **Figure 6-19**.

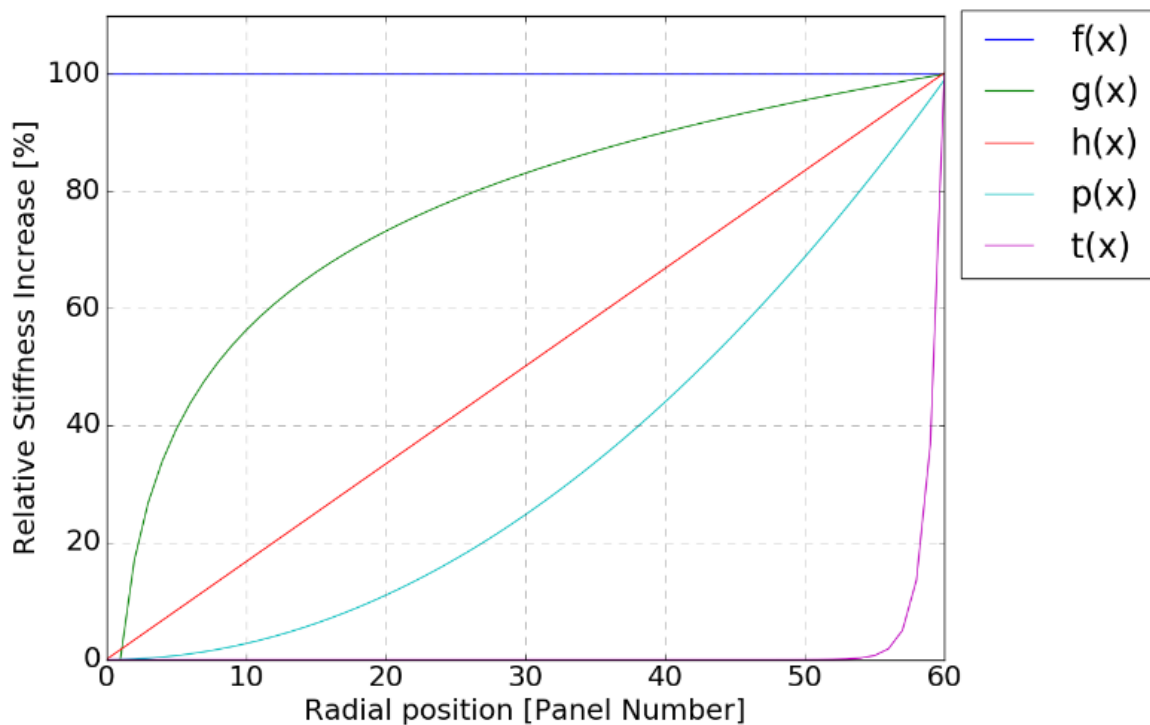


Figure 6-19 Stiffness Equations

The relative stiffness increase resulting from the introduced equations is added to the factorization, see equation (6-15).

$$a_{Twist} = 1 + \left[\left(\frac{\alpha_{ReachedTwist}}{\alpha_{AllowedTwist}} - 1 \right) * f(x) \right] \quad (6-15)$$

where:

| | |
|--------|------------------------|
| $f(x)$ | Corresponding equation |
|--------|------------------------|

As an example, when using the linear equation $h(x)$ from **Figure 6-19**, and an assumed factor for twist

$$\frac{\alpha_{ReachedTwist}}{\alpha_{AllowedTwist}} = 2$$

The factor a_{Twist} for the blade root is

$$a_{Twist} = 1 + [(2 - 1) * h(0)] = 1 + (1 * 0) = 1$$

The factor a_{Twist} for the panels in the middle of the blade is

$$a_{Twist} = 1 + [(2 - 1) * h(30)] = 1 + (1 * 0.5) = 1.5$$

And the factor a_{Twist} for the panels at the tip of the blade is

$$a_{Twist} = 1 + [(2 - 1) * h(60)] = 1 + (1 * 1) = 2$$

As a conclusion, only the panels at the blade tip are adapted by the full factor resulting from $\alpha_{ReachedTwist}/\alpha_{AllowedTwist}$. The panels at the blade root remain unchanged.

Using this approach, the reference blade is sized in the iterative sizing process with preliminary loads. The induced twist for this sizing is restricted. Only if the twist is restricted and the sizing is evaluating, that this restriction is transcended, the stiffness's are adapted. Therefore, the allowed twist of the reference blade is set to $\sim 1^\circ$. The reference blade has an induced twist without restrictions up to $\sim 5^\circ$ using the preliminary loads. This implicates a maximum factor for the twist stiffness increase of 5.

To evaluate the efficiency of the different equations, the mass has to be assessed. The following **Figure 6-20** is showing the results of the sizing with the different equations.

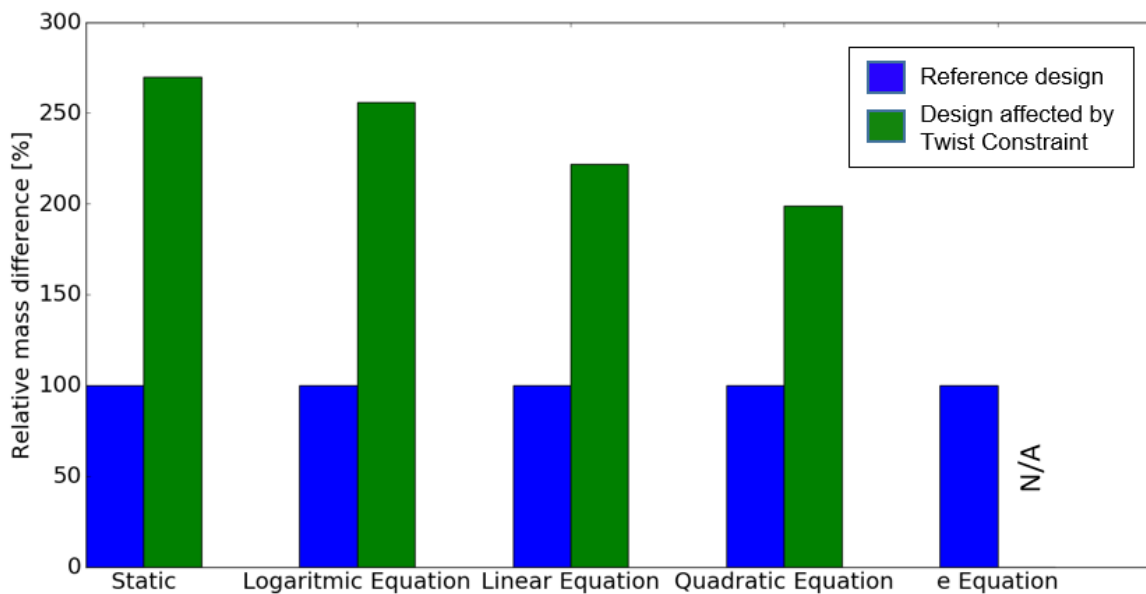


Figure 6-20 Equation Mass Results

The achieved results are showing, that the mass of the blade is the highest at the static sizing with a relative mass difference to the reference design of 270 %. Decreasing the stiffness requirements for the blade root, the logarithmic equation and the linear equation are decreasing in relative weight difference to 256 % and 222%. The quadratic equation achieves the lowest weight increase with a relative mass of

199%. It would be assumed that the e equation further decreases the weight, because the stiffness requirements for panels before the blade tip are further lowered. However, the usage of an e equation is not leading to a convergence of the sizing process. The e equation is mainly increasing the twist stiffness of the blade tip as visible from **Figure 6-19**. The required twist of only 1° is never reached during the sizing. This indicates, that the twist stiffness increase cannot be reduced to the region around the blade tip. It must include a greater number of panels along the radial position of the blade. The quadratic equation is therefore the most preferable application of twist stiffness.

It should be noted, that the relative mass difference is relatively high. However, the stiffness increase of maximum factor 5 is unreasonable. The highlight of this pre-study is more aimed towards the general conclusion about the equation to be used, than the relative mass difference. The relative mass difference is dependent on the required induced twist and the consequent twist factor.

Concluding that a quadratic function is best suited, the equation is further used to determine the radial starting point position of the optimization. This is the second design parameter of the study. The assumption is made, that the starting point of the twist stiffness increase shall start around a radial position of about 25 % of the total blade length. This corresponds to a blade length of 20 m or in terms of radial panel position, position 15. From this blade length on, the cross-sectional area is steadily reduced towards the blade tip. The following **Figure 6-21** is showing the adapted quadratic equation $z(x)$, which now starts to increase the twist stiffness at 25 % of the blade length. The equation $p(x)$ displays the quadratic equation, which is introduced before.

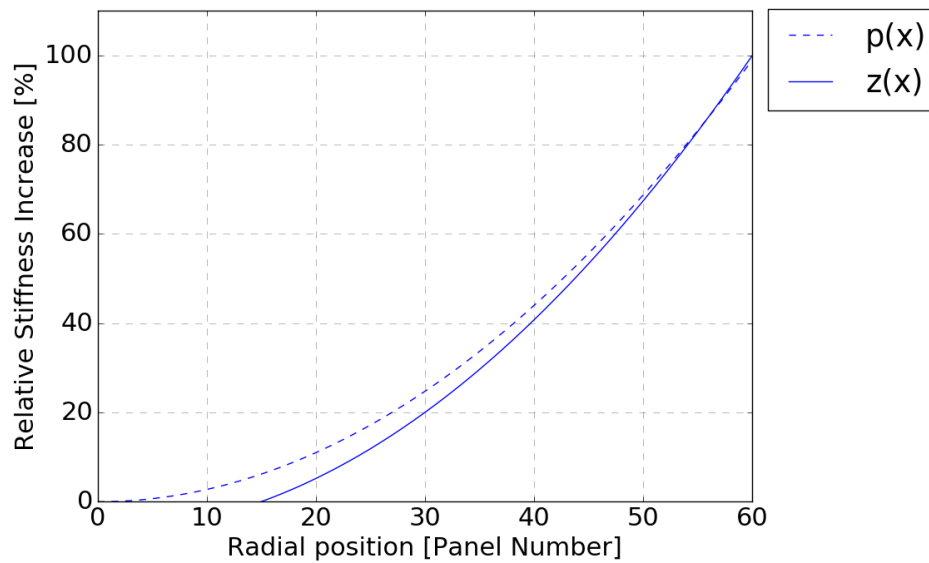


Figure 6-21 Stiffness Equation with adapted Start Point

The sizing of the blade with the adapted quadratic equation results in a further reduced relative mass difference compared to the standard quadratic equation. In a further study, the start point of the stiffness increase should have been further increased in 5 % steps upwards. However, the next evaluated start point of 30 % total blade length is not converging. A further increase of the start point is therefore obsolete. The made assumption about the start point is consistent with the achieved results. **Figure 6-22** shows the achieved relative mass difference results for the new equation.

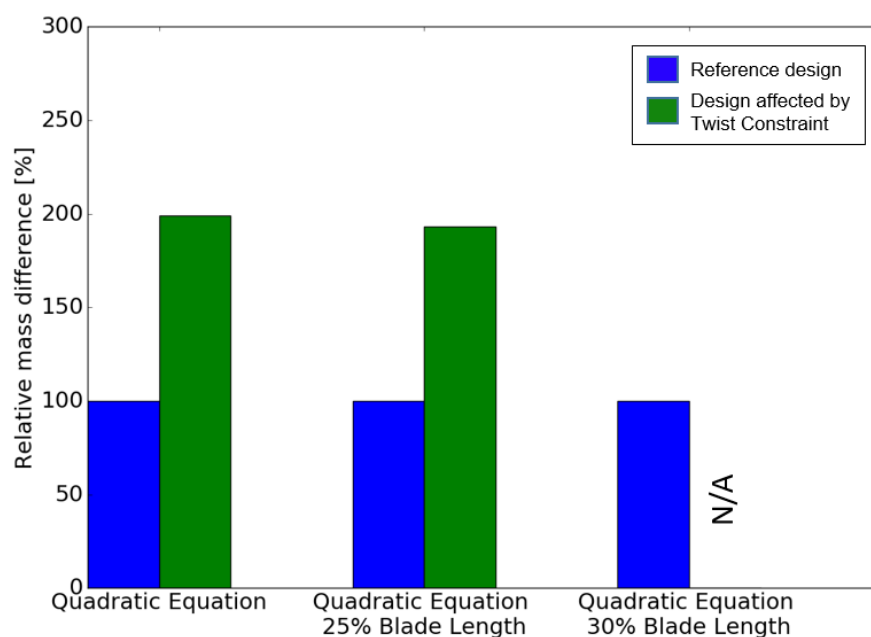


Figure 6-22 Equation Mass Results for the different Start Point

The relative mass difference further decreases to 193 % from the previous achieved 199 %.

Based on the achieved results, a quadratic equation with a starting point of 25 % of the blade length is implemented into the sizing process for the adaptation of twist stiffness. The equation used is once more displayed in (6-16).

$$z(x) = 0.0296 * x^2 - 6.67 \quad (6-16)$$

6.3 Loads Processing

The loads for the sizing of the structure must be evaluated throughout the structural design process. For the assessment of loads, the tool Simpack by Dassault Systèmes is used. Simpack is a multi-body simulation software, which enables the assessment of dynamic systems. Each part of the wind turbine is depicted by its eigenfrequencies and other system dependent variables [22].

The aerodynamic and inertia forces from different load scenarios are assessed in Simpack. The blade itself is integrated into the simulation by modal reduction. A modal reduction reduces the degrees of freedom of a complex structure to simplify the numerical expenses. For the modal reduction of the blade, the 30 RBE elements, introduced in chapter 6.1, are used. At those elements, the structure is defined by its cross section stiffness, its mass matrix and the eigenfrequencies. The described data is processed in Simpack to build the blade model. The dynamic behaviour of the blade becomes assessable, while reducing the required computational time.

The model created in Simpack can simulate and evaluate various load scenarios in a time integration. The wind turbine is built in Simpack, and the required wind fields for the different load scenarios are created. Starting the simulation, the controller of the turbine regulates the required turbine parameters as generator torque or blade pitch. The turbine starts up until a steady-state is reached. This steady-state differs for the evaluated load scenarios. Thus, different forces and moments are resulting for each load scenario.

The introduced engineering standards are giving a strict list of load scenarios to be assessed. The IEC-61400 divides between the general load scenarios, see **Figure 6-23**.

| Design situation | DL C | Wind condition | Other conditions | Type of analysis | Partial safety factors |
|--|---------|---|---|---------------------|------------------------------|
| 1) Power production | 1.1 | NTM $V_{in} < V_{hub} < V_{out}$ | For extrapolation of extreme events | U | N |
| | 1.2 | NTM $V_{in} < V_{hub} < V_{out}$ | | F | * |
| | 1.3 | ETM $V_{in} < V_{hub} < V_{out}$ | | U | N |
| | 1.4 | ECD $V_{hub} = V_r - 2 \text{ m/s}, V_r, V_r + 2 \text{ m/s}$ | | U | N |
| | 1.5 | EWS $V_{in} < V_{hub} < V_{out}$ | | U | N |
| 2) Power production plus occurrence of fault | 2.1 | NTM $V_{in} < V_{hub} < V_{out}$ | Control system fault or loss of electrical network | U | N |
| | 2.2 | NTM $V_{in} < V_{hub} < V_{out}$ | Protection system or preceding internal electrical fault | U | A |
| | 2.3 | EOG $V_{hub} = V_r \pm 2 \text{ m/s}$ and V_{out} | External or internal electrical fault including loss of electrical network | U | A |
| | 2.4 | NTM $V_{in} < V_{hub} < V_{out}$ | Control, protection, or electrical system faults including loss of electrical network | F | * |
| 3) Start up | 3.1 | NWP $V_{in} < V_{hub} < V_{out}$ | | F | * |
| | 3.2 | EOG $V_{hub} = V_{in}, V_r \pm 2 \text{ m/s}$ and V_{out} | | U | N |
| | 3.3 | EDC $V_{hub} = V_{in}, V_r \pm 2 \text{ m/s}$ and V_{out} | | U | N |
| 4) Normal shut down | 4.1 | NWP $V_{in} < V_{hub} < V_{out}$ | | F | * |
| | 4.2 | EOG $V_{hub} = V_r \pm 2 \text{ m/s}$ and V_{out} | | U | N |
| 5) Emergency shut down | 5.1 | NTM $V_{hub} = V_r \pm 2 \text{ m/s}$ and V_{out} | | U | N |
| 6) Parked (standing still or idling) | 6.1 | EWM 50-year recurrence period | | U | N |
| | 6.2 | EWM 50-year recurrence period | Loss of electrical network connection | U | A |
| | 6.3 | EWM 1-year recurrence period | Extreme yaw misalignment | U | N |
| | 6.4 | NTM $V_{hub} < 0,7 V_{ref}$ | | F | * |
| 7) Parked and fault conditions | 7.1 | EWM 1-year recurrence period | | U | A |
| 8) Transport, assembly, maintenance and repair | 8.1 | NTM V_{maint} to be stated by the manufacturer | | U | T |
| | 8.2 | EWM 1-year recurrence period | | U | A |

Figure 6-23 Load Scenarios from IEC-61400 [11]

The abbreviations in Figure 6-23 are further explained in Figure 6-24.

| | |
|--|---|
| The following abbreviations are used in Table 2: | |
| DLC | Design load case |
| ECD | Extreme coherent gust with direction change (see 6.3.2.5) |
| EDC | Extreme direction change (see 6.3.2.4) |
| EOG | Extreme operating gust (see 6.3.2.2) |
| EWM | Extreme wind speed model (see 6.3.2.1) |
| EWS | Extreme wind shear (see 6.3.2.6) |
| NTM | Normal turbulence model (see 6.3.1.3) |
| ETM | Extreme turbulence model (see 6.3.2.3) |
| NWP | Normal wind profile model (see 6.3.1.2) |
| $V_r \pm 2$ m/s | Sensitivity to all wind speeds in the range shall be analysed |
| F | Fatigue (see 7.6.3) |
| U | Ultimate strength (see 7.6.2) |
| N | Normal |
| A | Abnormal |
| T | Transport and erection |
| * | Partial safety for fatigue (see 7.6.3) |

Figure 6-24 Explanation of the IEC-61400 Load Scenarios [11]

The used loads process is only able to evaluate DLC load scenarios starting with 1 (normal power production). For different load scenarios, the controller, which manages the wind turbine, has to be adapted, as these load scenarios are based on possible failure modes of the turbine or modes, which are not corresponding to normal power production. Based on previous load assessments for the reference blade done by the IWES institute, the most critical DLC 1 load cases for the turbine are identified [23]. Therefore, the load scenarios to be simulated are drastically reduced, further decreasing the computational time. The following **Table 6-3** displays the evaluated load scenarios for the sizing of the blade.

Table 6-3 Evaluated Load Scenarios

| <u>DLC</u> | <u>Wind speed</u> | <u>Yaw Angle to Wind Direction</u> | <u>Turbulence Seed</u> |
|------------|-------------------|------------------------------------|------------------------|
| 1.1 | 13.0 m/s | -8; 0; 8 | 1; 2; 3; 5 |
| 1.1 | 19.0 m/s | -8; 0; 8 | 1; 2; 3; 5 |
| 1.1 | 25.0 m/s | -8; 0; 8 | 1; 2; 3; 5 |

As a standard approach introduced in the IEC-61400, it is common to reduce all analysed load scenarios to an extreme load case table for all relevant components.

| | F_x | F_y | F_z | M_x | M_y | M_z | F_R | θ_F | M_R | θ_M |
|------|-------|-------|-------|-------|-------|-------|-------|------------|-------|------------|
| Max. | | | | | | | | | | |
| Min. | | | | | | | | | | |
| Max. | | | | | | | | | | |
| Min. | | | | | | | | | | |
| Max. | | | | | | | | | | |
| Min. | | | | | | | | | | |
| Max. | | | | | | | | | | |
| Min. | | | | | | | | | | |
| Max. | | | | | | | | | | |
| Min. | | | | | | | | | | |
| Max. | | | | | | | | | | |
| Min. | | | | | | | | | | |
| Max. | | | | | | | | | | |
| Max. | | | | | | | | | | |

In this table, the maximum and minimum occurring forces and moments in all directions are displayed. Since these forces usually do not occur at the same time, the acting forces in other directions are also displayed for one maximum occurring force. The diagonal of an extreme load case table displays all minimum and maximum forces for each force and moment component. Only the load cases contributing to the maximum and minimum loads have an impact on the extreme loads table. The other load scenarios, which are not contributing to the extreme loads table, are still covered by the loads analysis, as their loads are lower than the outlined loads.

In the introduced loads process, extreme load tables are created for each of the 30 RBE elements in the blade. From these extreme load tables, the load cases for the FE tool are created where the forces are distributed over the RBE elements. The

loads process is using a conservative approach. Only the diagonal of the extreme load tables and the main moments and forces are contributing to the created load cases. This means, that even though not all maximum forces at all RBE elements in one direction occur at the same time, these forces are still applied simultaneously in the FE calculation. The reason behind this approach is that the number of evaluated load cases in the FE tool is drastically reduced. With this approach, a total number of 12 load cases is produced. Two loadcases for each force and moment component F_x, F_y, F_z, M_x, M_y and M_z displaying the minimum and maximum loads. This approach is common in the wind turbine industry, as the assumption is that even though the maximum and minimum forces do not occur at the exact same time, the difference of the maximal and minimal forces are neglectable small to the simultaneously acting forces. With a non-conservative approach by using all values in the extreme load case table, the load case number would be increased to 360 as 12 loadcases for each of the 30 RBE elements would be considered. Furthermore, including the maximal resultant forces such as F_R the number of load cases would further increase to 600. These load cases would include the named maximum and minimum forces of the corresponding node and the simultaneously acting forces on all other nodes rather than all maximum and minimum loads. It is obvious, that the reduction of the calculation time is immense.

6.4 „Technology 1“ Process

The „Technology 1“ depicts the aeroelastic tailoring. For this optimization, all introduced sub processes have to be combined.

This combination is done via the DLR tool “RCE” [25]. RCE (Remote Component Environment) allows to combine different sub processes in an overall correlating process. In this tool the different interfaces for the connection of the individual sub processes are thus created. Furthermore, the tool offers the possibility to add different iterative process tools, such as an optimizer or a parametric study. A process can therefore be automatically executed multiple times with different parameter sets. This favours the optimization of different structural layouts, as they can be adapted via the CPACS file which the FE model is based on.

The investigations for this technology are split into two different evaluations. The first evaluation for this technology is the assessment of the optimal induced twist,

based on the extreme force envelope formed by the extreme load table. As outlined in chapter 3, the load reduction shall be achieved by adapting the induced twist. The best induced twist is therefore corresponding to the angle of attack along the blade, where the lowest sum of aerodynamic forces occur. This is based on the assumption, that the acting aerodynamic forces and moments in the different directions have the same impact on the sizing of the structure.

This first evaluation process assesses different values of induced twist by sizing the blade with different to be achieved $\alpha_{TwistAllowed}$. After the sizing process sized the blade corresponding to this induced twist with preliminary loads, the new design is simulated in the loads process. The loads and sizing process are related to each other, as each sized structure leads to different deflections and masses of the blade. Therefore, a convergence has to be reached, where the iterative process of sizing and new load creation results into non changing loads. After this convergence is reached, the blade is fully sized and the loads are not changing anymore. When assessing the impact of the induced twist, the aerodynamic loads have to be reviewed. The process aims for a boundary condition for the induced twist for later structural optimizations. Thus, the achieved mass of the blade may be suboptimal and the assessed inertia loads are therefore not significant in this first evaluation. The aerodynamic loads are mostly unrelated to the achieved mass of the blade. These loads are dependent on the induced twist and the deflection of the blade. The approach of this process is shown in **Figure 6-26**.

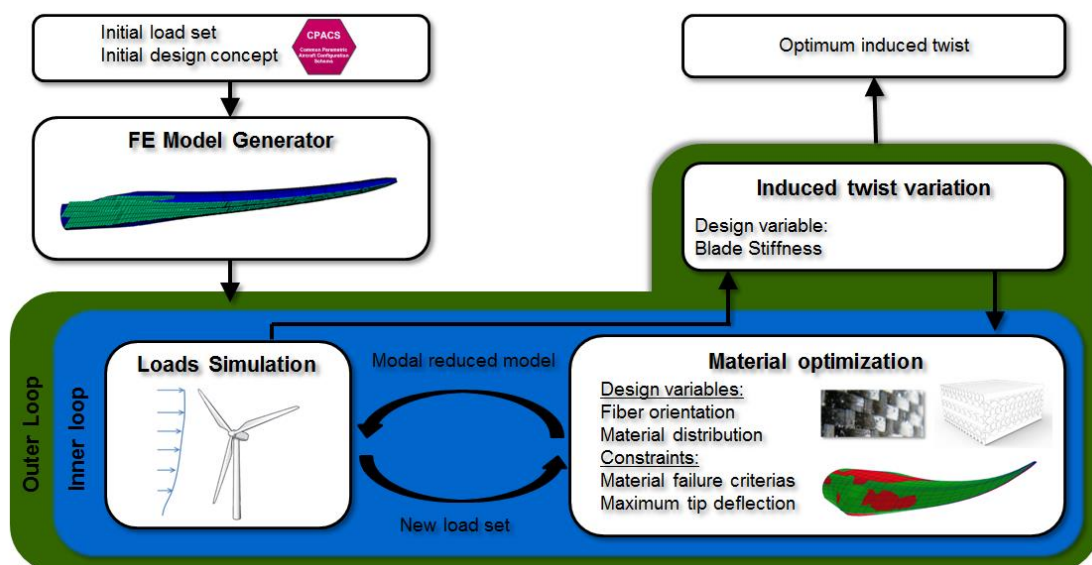


Figure 6-26 „Technology 1“ Optimal Induced Twist Process

An initial design concept is passed to the FE model generator. The outer loop of the process variates the allowed induced twist. Each assessed induced twist has to converge in the inner loop, which shows the correlation between the loads-sizing processing. Overall, this study is intended to provide a statement about the optimal induced twist. The integration of this optimization in RCE is shown in **Figure 6-27**.

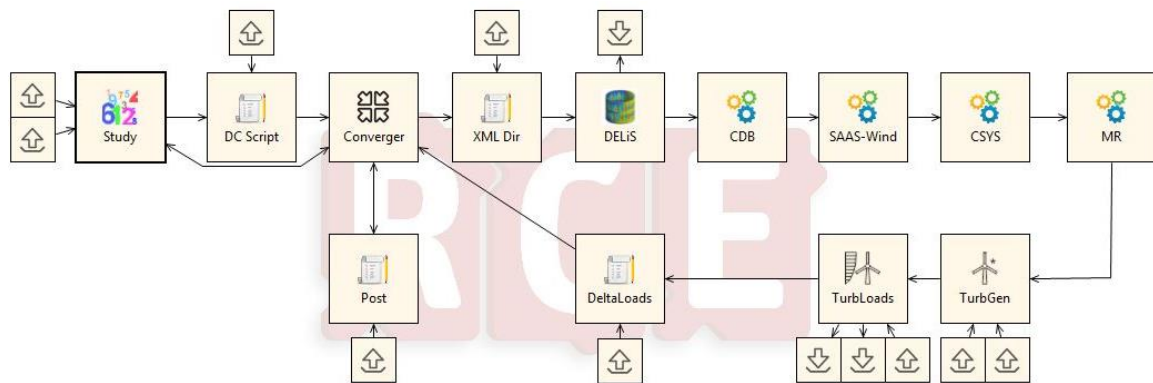


Figure 6-27 „Technology 1“ RCE Process

The RCE process begins with a parametric study, see “Study”, which creates the parameter set for an iteration. In the following blocks, the CPACS file is adapted by using the parameter set. The file is handed over to the “DELiS” tool, described in chapter 6.1. The created FE model is sized in the iterative Hypersizer process. After the sizing, the blade is modally reduced in “MR” and the simulation of the blade in the loads process “TurbGen” and “TurbLoads” begins. The results of the of the load simulation are send to the converger, which decides based on an overall load delta ΔL if the process is converged. The load delta ΔL is evaluated through the following equation (7-5). The load delta includes both, the resulting aerodynamic and the inertia forces.

$$\begin{aligned} \Delta L = & (\Delta F_{(x_{max})} + \Delta F_{(y_{max})} + \Delta F_{(z_{max})} + \Delta M_{(x_{max})} + \\ & \Delta M_{(y_{max})} + \Delta M_{(z_{max})} + \Delta F_{(x_{min})} + \Delta F_{(y_{min})} + \\ & \Delta F_{(z_{min})} + \Delta M_{(x_{min})} + \Delta M_{(y_{min})} + \Delta M_{(z_{min})})/12 \end{aligned} \quad (6-17)$$

Each delta of a force or moment is a relative value of the difference of loads between the current iteration and the forerunning iteration. Therefore, ΔL is the mean relative

difference of the load deltas between load-sizing iterations. The results of this first investigation shall be the optimal induced twist. This optimal induced twist is further used to determine the structural design of the blade, which corresponds to this induced twist, while being lightweight, using different structural concepts. The optimal induced twist is therefore set as a boundary condition in the sizing process. The sketch of the process flow is shown in **Figure 6-28**.

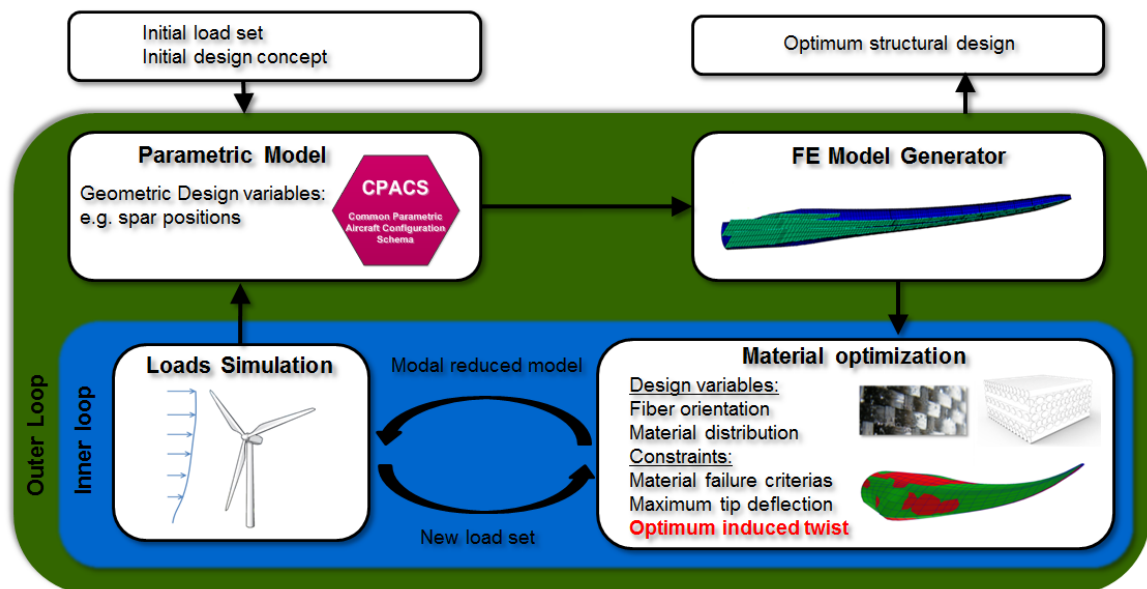


Figure 6-28 „Technology 1“ Structural Optimization Process

As a conclusion the result of these two evaluation processes shall be the achievement of the value of the optimum induced twist and the corresponding best structural design to reach it. The RCE process layout displayed in **Figure 6-27** is unchanged. Only the internal processing of the variables is adapted.

6.5 „Technology 2“ Process

The process for the „Technology 2“, the active flap towards the blade tip, differs from „Technology 1“. For this technology, there is currently no loads process available. The loads process would need to inhibit a controller, which actively controls the angle of attack of the flap, based on the acting loads. An assessment of the load reduction of this technology is therefore currently not possible.

However, the impact of the flap cut-out added to blade in the point of view of the structural design is assessable. The blade including the flap cut-out is sized with the converged reference loads of the blade. The result is the achieved mass of the design and the achieved deflections. The simple RCE process is displayed in **Figure 6-29**.

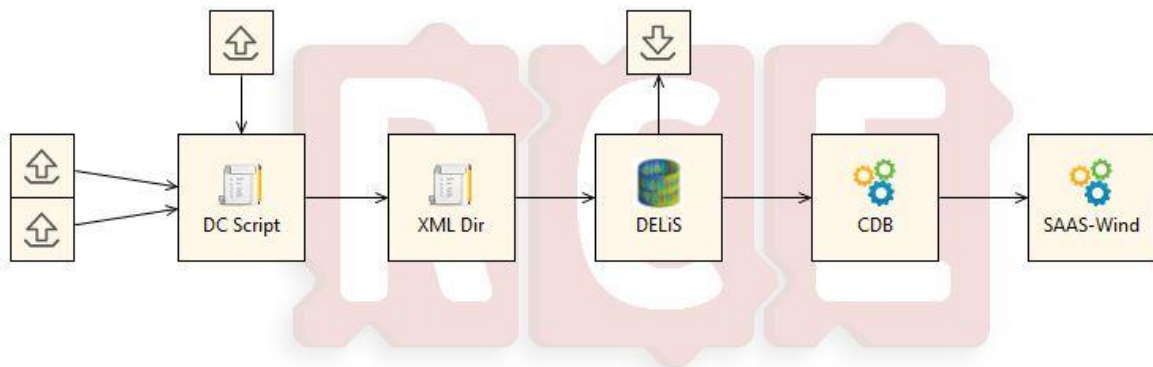


Figure 6-29 „Technology 2“ RCE Process

As visible, the complexity is drastically reduced. Because the loads cannot be assessed, there is no sizing-load convergence.

As a conclusion, the investigations on the „Technology 2“ shall lead to a statement regarding the structural impact of the flap cut-out at the trailing edge of the blade.

7 Optimization of the Structural Design

In this section, the different structural concepts for „Technology 1“ to achieve a load reduction shall be explained. For the different concepts a parameter space is defined which shall be evaluated through a parametric study as introduced in chapter 6.4. For „Technology 2“ an adapted structural design for compensating the strength and stiffness reduce due to the flap cut-out is discussed.

7.1 „Technology 1“

As a boundary condition for the aeroelastic tailoring, the induced twist must be varied from the reference design. From an aerodynamic point of view, the loads acting on the blade shall be lower with an induced twist which leads to a lower angle of attack. The aerodynamic forces created by an airfoil are formally described by the c_l vs. c_d curve. As mentioned in chapter 3, these coefficients are determining the acting lift and drag forces on an airfoil. With a positive angle of attack, a positive lift force is induced by the airfoil. This force is parallel to the wind direction, hence it increases the acting thrust on the blade. A lower angle of attack is decreasing the lift force acting on the airfoil. A lower angle of attack is therefore preferable as it leads to a load reduction.

To reduce the lift created by the airfoil, the angle of attack has to be shifted towards lower values in comparison to the reference design. From a structural point of view, this is achieved by shifting the shear centre of the cross sections of the rotor blade towards the leading edge as the aerodynamic forces are inducing less twist. This is further explained in the following. The shear centre of a cross section describes the point, where the resultant of all transverse forces have to attack to achieve a torsion free deflection. For a rectangular cross section, the shear centre M corresponds to the geometrical centre of gravity S as the cross section has two symmetry axes [26], see **Figure 7-1**.

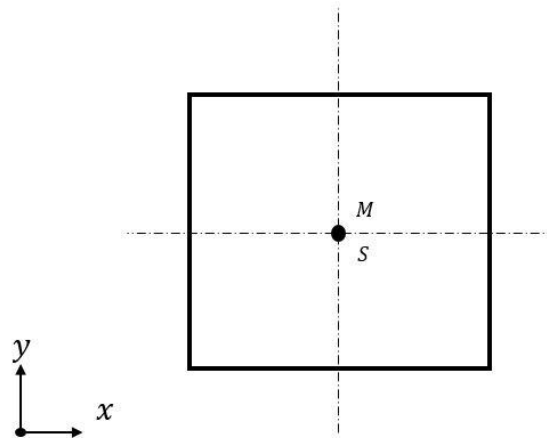


Figure 7-1 Shear Centre of a Rectangular

When simplifying an aerodynamic profile geometry to a rectangle and assuming that the width of the cross section is not changing, the centre of shear is equal to the geometrical centre of gravity as shown below, see **Figure 7-2**.

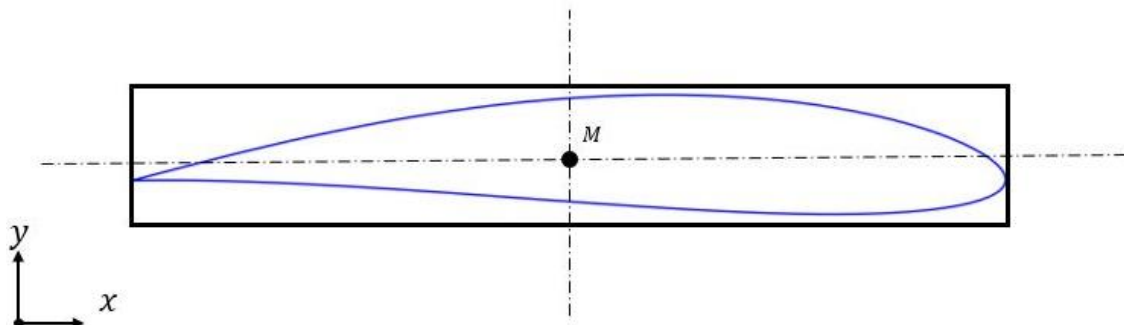


Figure 7-2 Simplification of the Airfoil Geometry [9]

From this simplification, the shear centre of the airfoil becomes easily assessable. Furthermore, the influence of acting aerodynamic forces on the induced twist is derivable. A larger distance between the point of impact of a force that is not parallel to the x -axis has an increased influence on the induced twist. A force acting further from the shear center in one of the two x -directions causes a higher induced twist due to a larger lever arm. The centre of pressure displays the attack point of the resultant of all acting aerodynamic forces on the airfoil. In general, the determination of the pressure point is a complex task, because all acting pressures over the geometries surface have to be evaluated. However, through analytical and testing methods, it was determined, that the centre of pressure of an airfoil is located at

roughly $\frac{1}{4}$ distance of the total chord length from the leading edge at all angle of attack's [27]. In the following, the y coordinate of the centre of pressure, compare **Figure 7-2**, is assumed to be located directly on the symmetry axis parallel to the x -axis of the displayed coordinate system. For the induced twist, the x location of the centre of pressure is from greater impact.

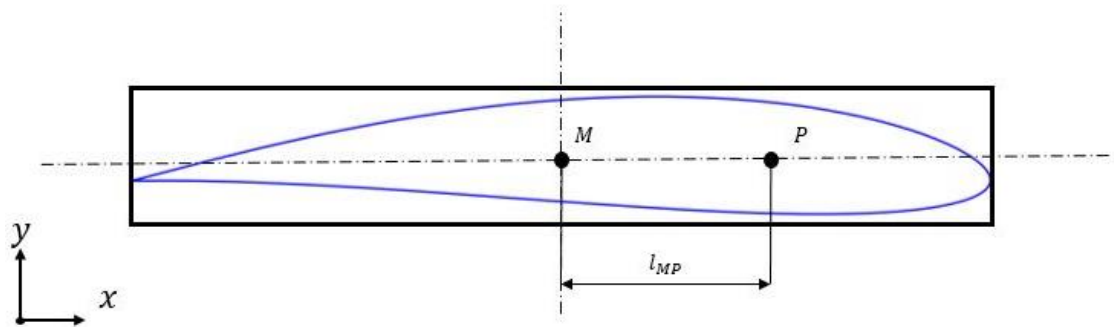


Figure 7-3 Centre of Pressure of the Airfoil [9]

The centre of pressure P and the centre of shear M are shown in **Figure 7-3**. As previously mentioned, the length between the two centres l_{MP} determines the overall impact of the aerodynamic forces on the induced twist. When sketching the aerodynamic lift and drag in the centre of pressure, compare **Figure 7-4**, it becomes apparent, that the centre of shear must be moved towards the centre of pressure in order to lower the induced twist and therefore the angle of attack. Hence, reduce the length l_{MP} .

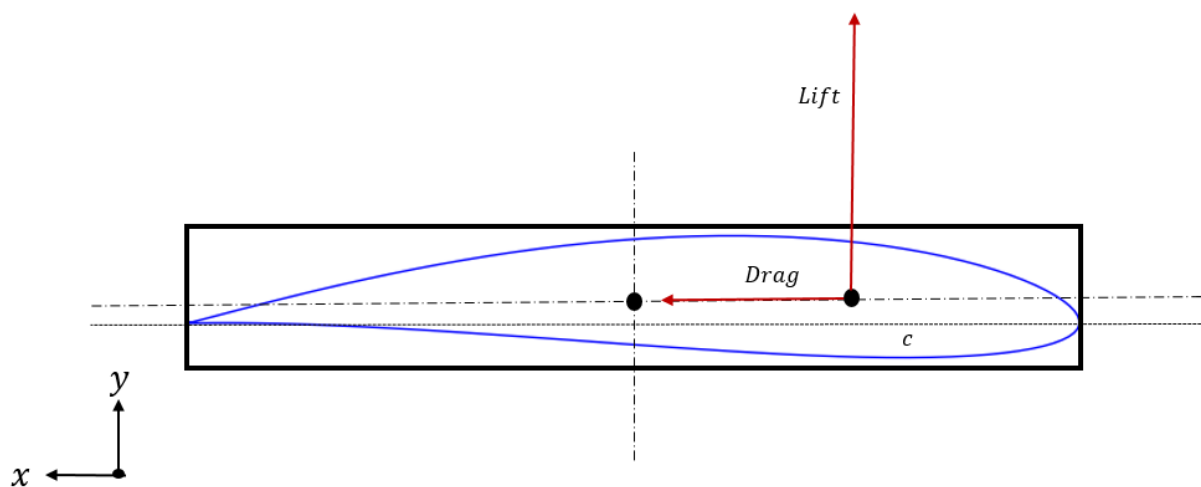


Figure 7-4 Aerodynamic Forces in the Centre of Pressure [9]

For more complex cross sections without a symmetry axis the coordinates of the shear centre are calculated via the equations (7-1) and (7-2) [26].

$$x_M = \frac{1}{I_x} \int_0^1 S_x(s)(x \sin \varphi + y \cos \varphi) ds \quad (7-1)$$

$$y_M = \frac{1}{I_y} \int_0^1 S_y(s)(x \sin \varphi + y \cos \varphi) ds \quad (7-2)$$

where:

x_M Distance in x direction of the shear centre from the coordinate system origin

y_M Distance in y direction of the shear centre from the coordinate system origin

S_x Static moment of the cut-off imagined cross section part in x direction

S_y Static moment of the cut-off imagined cross section part in y direction

I_x Surface moment of inertia in x direction

I_y Surface moment of inertia in y direction

s Subdivide of the total area A of the cross section into infinitesimal areas s

φ Angle between the norm vector and the x direction of the infinitesimal area

The static moments result from equation (7-3) and (7-4) [26].

$$S_x = \int_0^s y dA \quad (7-3)$$

$$S_y = \int_0^s x dA \quad (7-4)$$

where:

- x Distance in x direction of the infinitesimal areas s to the geometrical centre of gravity
- y Distance in y direction of the infinitesimal areas s to the geometrical centre of gravity
- dA Area of the infinitesimal areas s

When finally considering the cross-section of the aerodynamic profile including the spars, the shear centre is shifted towards the leading edge by the increased cross-sectional area. It can be concluded from equation (7-4) that a movement of the spars towards the leading edge or reducing the area of the cross section to the left of the shear centre, results in a further shifting of the shear centre towards the leading edge. This is based on the value of $S_x(s)$ as the value of it grows towards the leading edge as dA grows due to the increased cross section area by the spars. Based on this growth, the coordinate x_M is greater, thus the centre of shear is shifted towards the leading edge, see **Figure 7-5**.

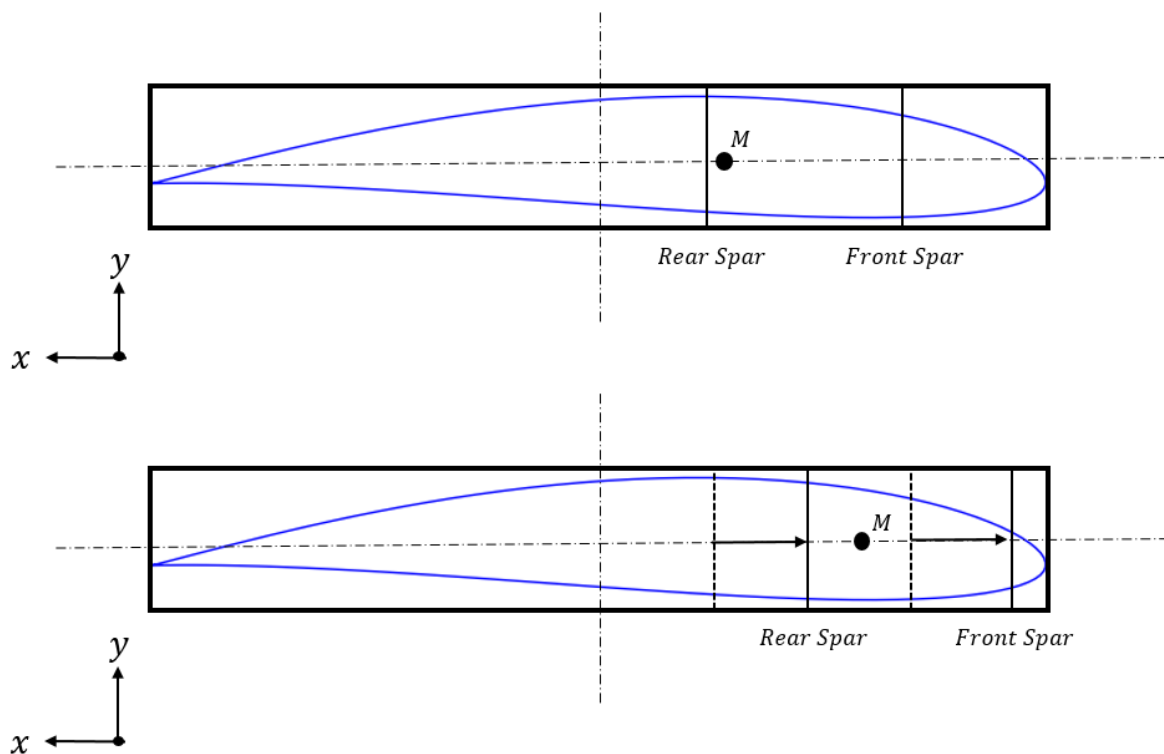


Figure 7-5 Shifting of the Centre of Shear

Both concepts introduced in the following chapters are based on this conclusion. The positions of the spars are adapted, leading to a shifting of the shear centre and therefore impacting the induced twist.

7.1.1 C-Beam Concept

The first concept for „Technology 1“ is the c-beam. This concept focuses on reducing the number of spars towards the blade tip to only one spar. The shear centre is moved dependent on the position of the single remaining spar and through the lower remaining cross section. A preliminary assessment of the c-beam concept depicts the influence on the induced twist. **Figure 7-6** shows a FE calculation of such a beam, where the induced twist is visible due to the shift of the centre of shear.

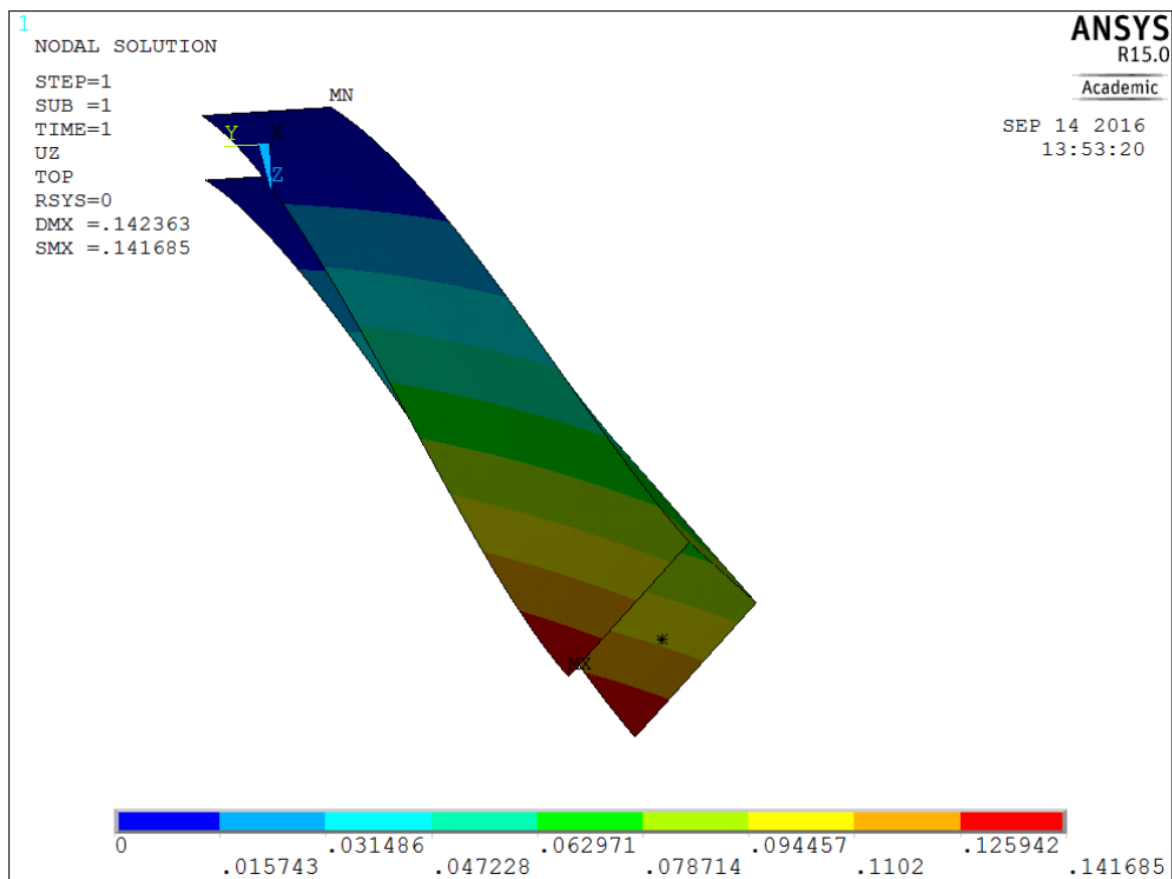


Figure 7-6 C-Beam Concept Spar [28]

A complete removal of the spar, as shown in the above figure, is not meaningful. This would lead to a more unstable blade structure. Furthermore, it was described

in chapter 6.2.5 that the induced twist increases in the radial direction towards the tip of the blade. The influence of the induced twist near the blade root is therefore negligible.

For this concept, it is decided to reduce the length of the front spar. The reduction of the length of the front spar instead of the rear spar may seem contradictory, since the reduction of the length of the rear spar has a greater influence on the induced twist due to its position in front of the shear centre. Therefore, no further adjustments to the structure would shift the shear centre not in the leading edge direction but in the trailing edge direction. The front spar is positioned in front of the shear centre and thus contributes unchanged to the shear centre being closer to the leading edge. However, the influence on the induced twist can be adjusted with this approach by an additional shift of the rear spar towards the leading edge and thus the shear centre is shifted accordingly. Overall, this leads to a curvature of the rear spar to the leading edge, which begins at the point where the front spar ends. The advantage of reducing the length of the front spar is that the rear spar runs much more centrally through the blade than the front spar. A more central position of the remaining spar is favourable for the stability of the blade structure. In contrast, reducing the length of the rear spar significantly reduces stability. A reduced stability promotes the development of torsional oscillations and local buckling.

The parameter space for examining this concept is formed by two parameters. First, the total length reduction of the front spar and second, the position of the rear spar at the blade tip. As a reasonable assumption, the relative minimum length of the spar is set at 0.5 of the total blade length. The maximum length is limited to 0.9. The end position of the spar in the reference design is 0.95 of the total blade length.

The second parameter, the relative chordwise position of the rear spar at the blade tip, is 0.236 to 0.428 of the local chord length. A value of 1 corresponds to the position of the trailing edge. The higher the relative value, the more the spar is moved to the trailing edge. The relative value of 0.428 of the local chord length furthermore corresponds to the position of the rear spar in the reference design. The value of 0.236 corresponds to the maximum position of the rear spar to the front edge without changing the area of the spar caps. As a reminder: The spar caps are defined as the area between the spars. At a relative chordwise position of the rear spar of 0.236 of the local chord length, the spar caps end at a chordwise position of 0.01. A lower

value for the relative chord position of the rear spar would therefore lead to a reduction of the area of the spar caps.

To reduce the number of possible combinations investigated by the parametric study, the two introduced parameters are made dependent to each another. It is obvious, that a position of the rear spar more towards the leading edge of the blade tip has a greater impact on the induced twist. Furthermore, the same is concluded for the length reduction of the front spar. The earlier the front spar ends, the greater the impact. A dependency of the two parameters is therefore derived via equation (7-5).

$$f_{eta}(x) = 1.7391 * x + 0.1522 \quad (7-5)$$

where:

| | |
|-----------|--|
| f_{eta} | Maximum relative length of the front spar |
| x | Relative chordwise position of the rear spar |

The equation indicates, that the further the rear spar is moved towards the leading edge, the greater the reduction of the length of the front spar.

Based on the introduced parameter space, 6 parameter sets for the structural concept are assessed. The used parameters in the 6 spar layouts are displayed in **Table 7-1** resulting from the equation (7-5).

Table 7-1 „Technology 1“ C-Beam Layouts

| Layout Number | Relative Chordwise Position of the Rear Spar at the Blade Tip | Relative Length of the Front Spar |
|---------------|---|-----------------------------------|
| 1 | 0.2 | 0.5 |
| 2 | 0.246 | 0.59 |
| 3 | 0.292 | 0.66 |
| 4 | 0.338 | 0.74 |
| 5 | 0.384 | 0.82 |
| 6 | 0.428 | 0.9 |

It is important to note that in comparison to the other layouts, the position of the rear spar at layout 6 remains unchanged compared to the reference design. As previously explained, this leads to a shifting of the shear centre towards the trailing edge for this single layout. The reason for this is further explained in chapter 7.1.3.

The following **Figure 7-7** to **Figure 7-12** are showing the different spar layouts 1 – 6 from the top view.



Figure 7-7 C-Beam Layout 1

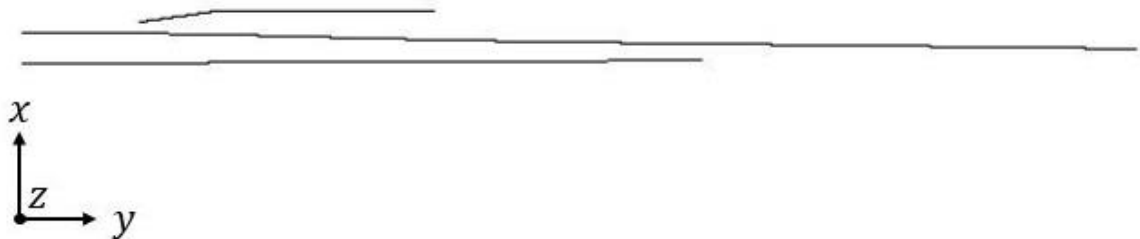


Figure 7-8 C-Beam Layout 2

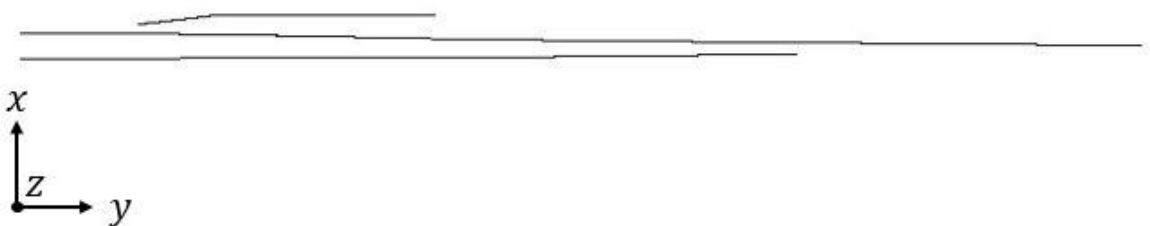


Figure 7-9 C-Beam Layout 3

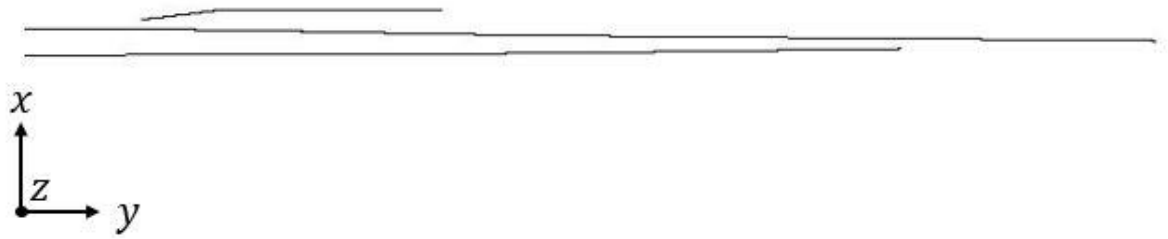


Figure 7-10 C-Beam Layout 4

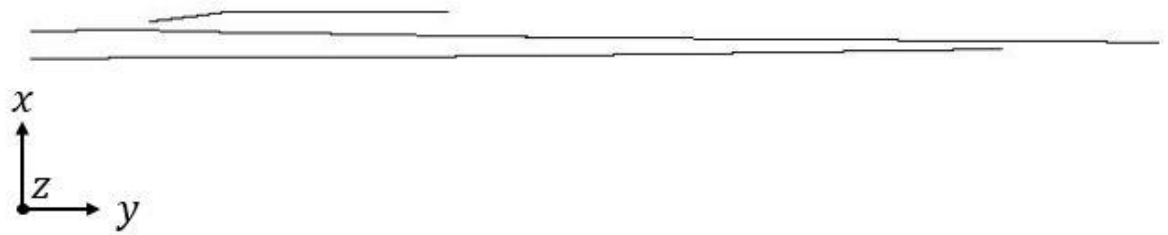


Figure 7-11 C-Beam Layout 5

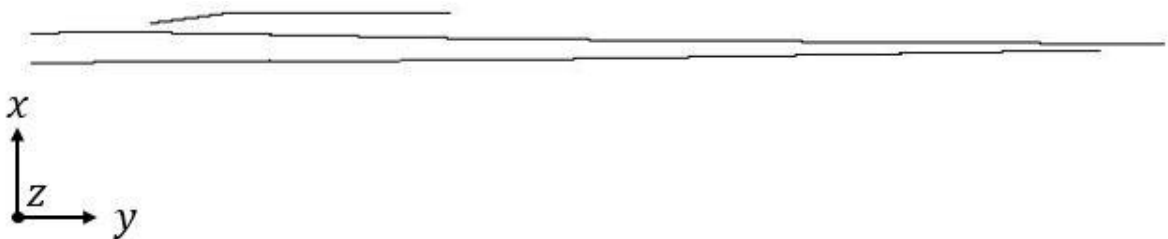


Figure 7-12 C-Beam Layout 6

7.1.2 Swept Beam Concept

The second concept for the „Technology 1“ is the swept beam concept. In the reference design, both spars are running linear through the blade, see **Figure 6-3**. Using a swept beam approach, the beam course becomes non-linear. Furthermore, by changing the relative chordwise end position of both spars, the spars are moved towards the leading edge, compare **Figure 7-5**. The course of a swept beam is indicated in **Figure 7-13**.

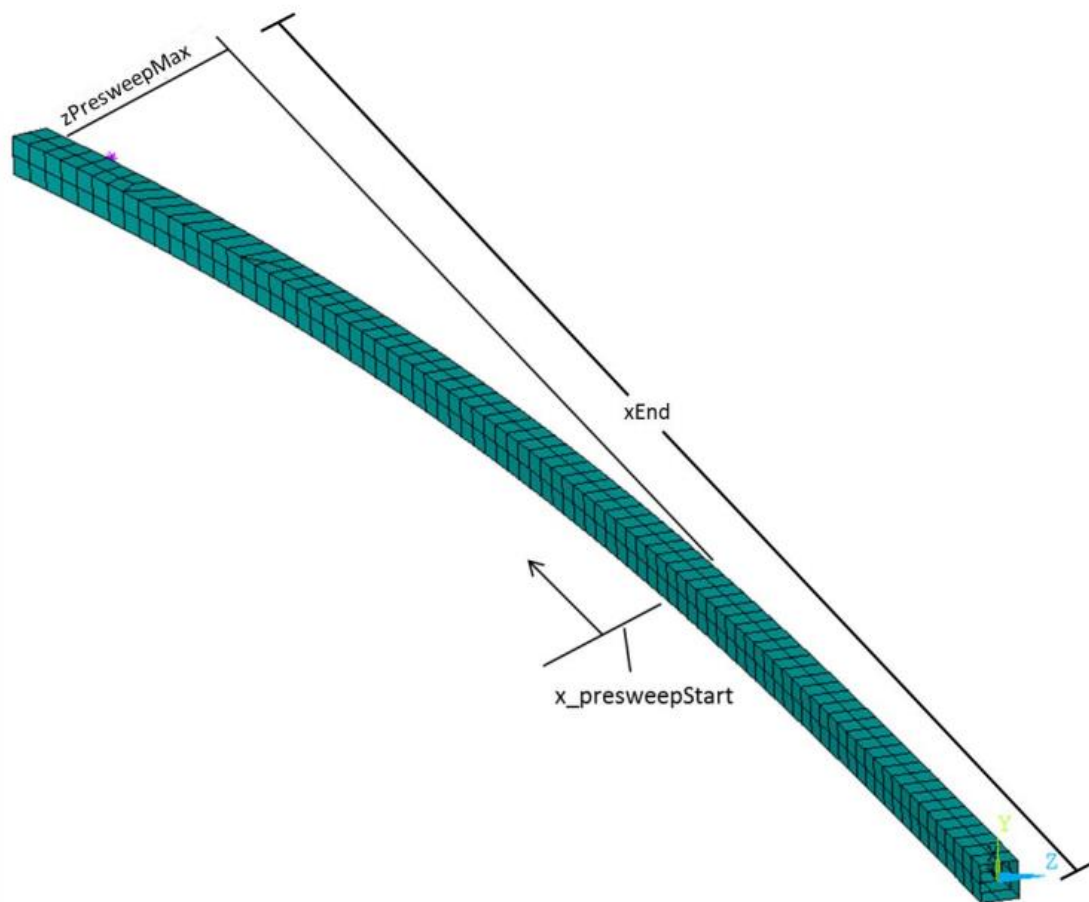


Figure 7-13 Swept Beam [28]

The figure also indicates the two parameters necessary for the description of the swept beam. The first parameter $x_{PresweepStart}$ corresponds to the start position of the sweep. The second parameter $z_{PresweepMax}$ corresponds to the chordwise position of the spars at the blade tip. The course of a swept beam is described via the equation (7-6). This equation results from earlier investigations on sweeping beams [29].

$$f_{Presweep}(x) = z_{PresweepMax} * \left(\frac{x - x_{PresweepStart}}{x_{Tip} - x_{PresweepStart}} \right)^3 \quad (7-6)$$

The x coordinate in equation (7-6) corresponds to the length direction of the beam. The value x_{Tip} describes therefore the maximum length of the beam. The z coordinate corresponds to the chordwise direction of the beam.

From this equation, the position of the front spar is determined by using different parameters for the relative chordwise end position of the spar as well as the sweep start point. In contrast to the shown beam, the blade structure is not including a box beam, but multiple spars. The positions of the rear spar are therefore described through the definition of the reference spar caps. Equal to the c-beam concept, the area of the spar caps shall be unchanged. Thus, the chord-wise position difference of the front and rear spar must be kept unchanged from the reference design. The coordinates of the rear spar are therefore determined by equation (7-7).

$$g_{Presweep}(x) = z_{PresweepMax} * \left(\frac{x - x_{PresweepStart}}{x_{Tip} - x_{PresweepStart}} \right)^3 + \Delta z_{Reference} \quad (7-7)$$

Where $\Delta z_{Reference}$ describes the relative chordwise delta between the front spar and the rear spar in the reference design.

From the introduced equations, 30 new positional definitions for each spar are created in the CPACS file. The parameter space of the sweep start point is determined by the maximum value of 0.7 of the total blade length down to 0.4 of the blade length. The lower boundary of 0.4 corresponds to the endpoint of the third trailing edge spar. A sweep starting earlier than the end of the trailing edge spar is assumed meaningless, as the structures stability and shear centre is at those positions also dependent on the third trailing edge spar. The second parameter space for the chordwise shifting of the two spars is equal to the c-beam concept. The maximum shifting of the rear spar to the leading edge is defined through the relative chordwise position of 0.236. The minimum shifting corresponds to a relative chordwise position of 0.428. As the positions of the rear spar is dependent on the positions of the front spar, the

values of the chordwise position of the front spar are used in this study. The chordwise position of 0.236 of the rear spar corresponds to a chordwise position of the front spar of 0.01. The upper boundary of 0.428 corresponds to a relative chordwise position of the front spar of 0.236.

In an equal approach as the c-beam concept, the two parameters are also made dependent on each other through the shown equation (7-8).

$$f_{Sweep}(x) = 1.6129 * x + 0.3194 \quad (7-8)$$

where:

| | |
|-------------|---|
| f_{Sweep} | Start point of the sweep |
| x | Relative chordwise position of the front spar |

It is similar recognizable, that the earlier the sweep of the spars starts, the greater the impact on the induced twist is. Furthermore, the impact is also greater, the higher the shifting of the spar positions to the leading edge.

Based on the introduced parameter space and the equations, 4 different parameter combinations are evaluated for this concept. The parameters of the layouts are shown in **Table 7-2**.

Table 7-2 „Technology 1“ Swept Beam Layouts

| Layout Number | Relative Chordwise Position of the Front Spar at the Blade Tip | Relative Start Position of the Sweep |
|---------------|--|--------------------------------------|
| 1 | 0.05 | 0.4 |
| 2 | 0.10775 | 0.5 |
| 3 | 0.171875 | 0.6 |
| 4 | 0.236 | 0.7 |

The following **Figure 7-14** to **Figure 7-17** are furthermore showing the different spar layouts 1 – 4 from the top view.

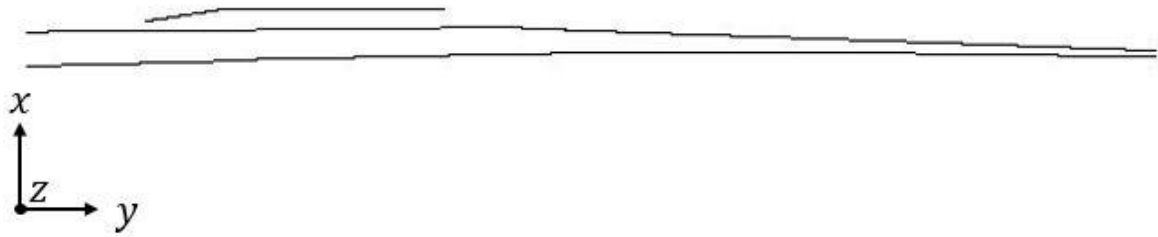


Figure 7-14 Swept Beam Layout 1

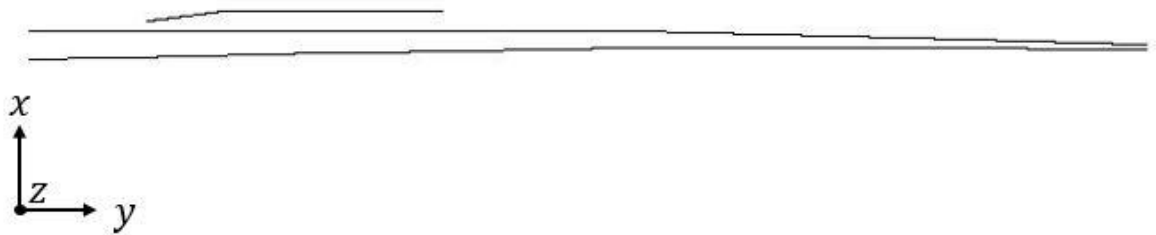


Figure 7-15 Swept Beam Layout 2

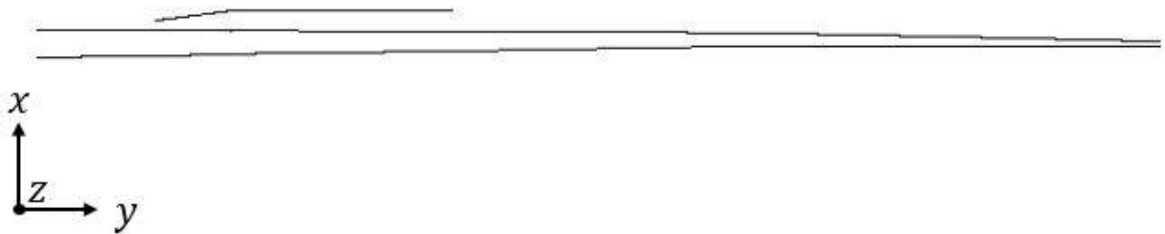


Figure 7-16 Swept Beam Layout 3

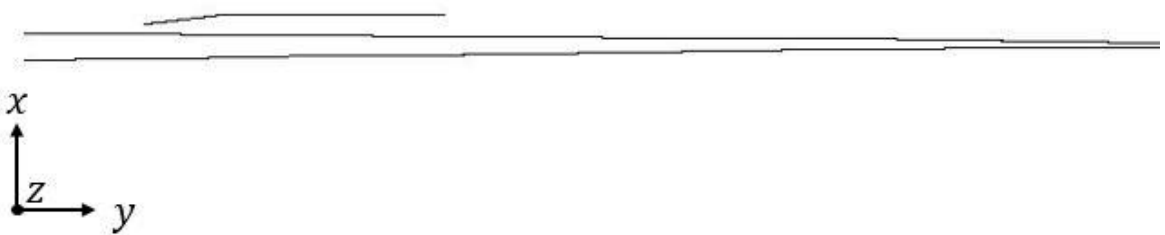


Figure 7-17 Swept Beam Layout 4

7.1.3 Induced Twist Concept

In order to evaluate different induced twist variations, it must be ensured that the blade achieves different induced twist angles compared to the reference design. It is therefore necessary to change the evaluated structure layout. For this study, it is reasonable to choose a concept that produces a large induced twist. In this way, a larger range of induced twists can be evaluated, since the twist constraint only has a limiting effect on the induced twist. As explained in chapter 7.1, all concepts aim at reducing the induced twist. Thus, these concepts would not be suitable for a study with a large range of induced twists. For this reason, the c-beam layout 6 is chosen to evaluate different induced twists. As described in chapter 7.1.1, only the front spar is shortened in this layout. The position of the rear spar remains unchanged compared to the reference design. Thus, the shear centre is moved further to the trailing edge. This shift results in an increased induced twist compared to the reference design and a larger range of induced twists can be evaluated.

The parameter set for this evaluation is not determined by changes to the structural layout, but by the allowed maximum induced twist. The parameter is therefore the limitation of the induced twist. The parameter space cannot be delimited before the study is carried out. It is dependent on the different results achieved within the study.

7.2 „Technology 2“

The established loads process does not allow to take into account the load reduction caused by the active flap. However, the arising cut-out near the blade-tip for the flap must be compensated by the structure. The “Smart Blades 1” project achieved the result of the optimal position of the flap as well as the flap depth. The following parameters in **Table 7-3** are displaying this optimum:

Table 7-3 Flap Dimensions

| Flap Start | Flap End | Flap Depth |
|------------|----------|--------------------------------|
| 66 m | 76 m | 30 % of the local chord length |

The correlated FE model is shown in **Figure 7-18**.



Figure 7-18 „Technology 2“ Flap Cut-Out Plan View

From the values in **Table 7-3** results the relative chordwise depth of the flap of 0.7. As the rear spar, which is located nearer to the flap than the front spar, is running at a relative chordwise position of roughly 0.4 in the radial region around the flap cut-out, the cut-out is not sufficiently closed. It is therefore obvious to move the rear spar towards the flap cut-out to not only close the cut-out, but also compensate for the added instability in the region of the flap cut-out.

For the design, two new positions are defined for the rear spar which correspond to the position of the flap start and the flap end in the CPACS file. The new positions of the rear spar at these locations is set to a relative chordwise position of 0.65. Even though the flap has only a total depth of 30 % of the local chord length, a 5 % margin is added for possible connection components between the flap and the spar. The adaptation of the rear spar position is shown in **Figure 7-19**.

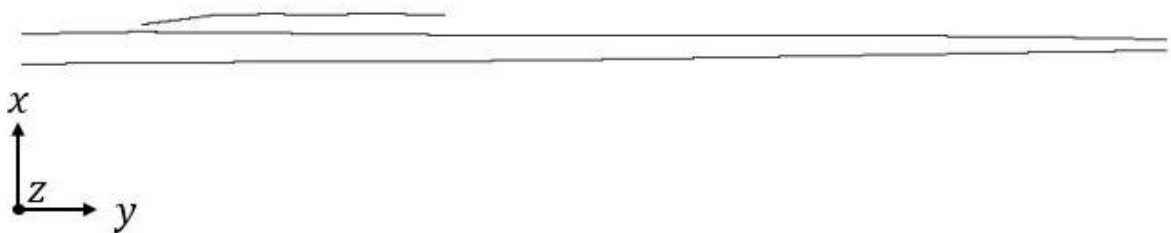


Figure 7-19 „Technology 2“ Spar Layout

It is still recognizable, that the region between the spars, thus the spar caps, has an increased area in comparison to the reference design. In contrast to the two previous concepts introduced in "Technology 1", the increase in the area of the spar caps is due to the mere displacement of the rear spar. **Figure 7-20** displays the detailed spar course at the flap cut-out. The yellow colour marks the lower shell of the blade, the red colour the spars. The upper shell is hidden for a clear view.

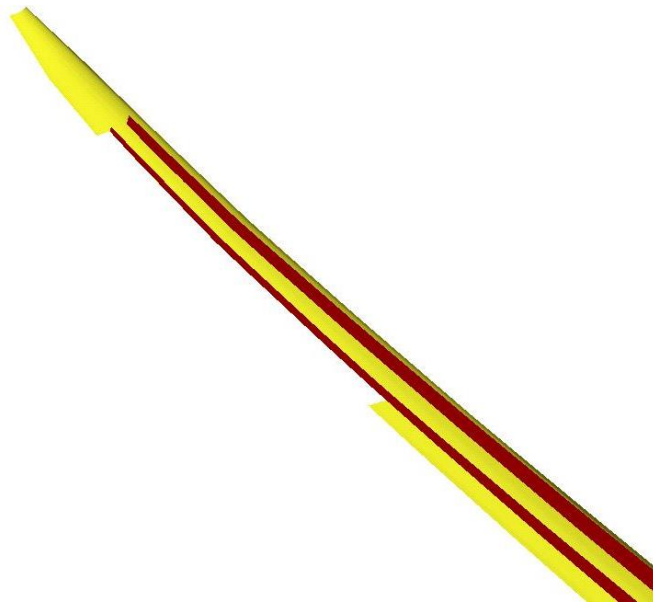


Figure 7-20 Spar Course at the Flap Cut-Out

Figure 7-21 shows the blade flap cut-out including the upper shell, marked in blue.

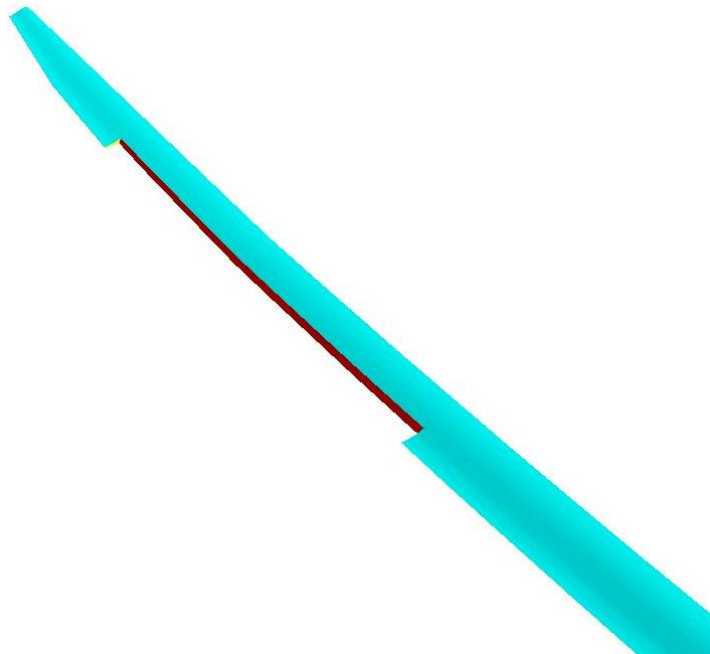


Figure 7-21 Flap Cut-Out with all Assemblies

8 Results Discussion

In the following sections, the different achieved results from the previous explained parametric studies are shown. First, the sizing of the reference design is discussed in order to be able to compare the different results for adapted structural layouts. Second, the „Technology 1“ is discussed, starting with the achieved results for the twist optimization as it shall be used as a base for the following optimization of the c-beam and the swept beam. Finally, the „Technology 2“ results are compared to the results of the reference design.

8.1 Reference Design

The sizing of the reference design, which is also in detail shown in chapter 6.1, is necessary to assess the different results from the evaluated parametric studies. Besides the resulting mass of the blade, the acting forces on the structure shall be depicted. As the forces are further described by their indexes based on the used coordinate system, the coordinate system of the blade shall be displayed. The positive x axis points towards the trailing edge of the blade. The positive y axis describes the radial position along the blade. Last, the positive z axis is parallel to the wind direction, pointing towards the tower. These definitions are equal to the coordinate systems shown in the FE model figures. The coordinate system is also sketched in **Figure 8-1**.

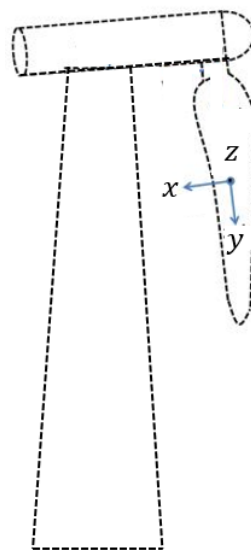


Figure 8-1 Global Force Coordinate System [23]

The angle of attack of an airfoil of the blade is defined by the pitch of the blade, the pre-twist, as described in chapter 4, and the induced twist. From a structural point of view, the pitch of the blade as well as the pre-twist are given parameters. The pitch of the blade is dependent on the reviewed load scenario. The pre-twist is defined through the reference design of the blade. The design parameter is therefore the induced twist. In the following, the induced twist hence depicts changes on the angle of attack in comparison to the reference design. The angles of the induced twists are corresponding to the shown coordinate system. For the induced twist, a negative value defines a torsion towards lower angle of attacks of the airfoil. At a positive induced twist, the blade twists towards a higher angle of attack. A positive induced twist angle α is shown in **Figure 8-1**, indicating a torsion leading to an increased angle of attack.

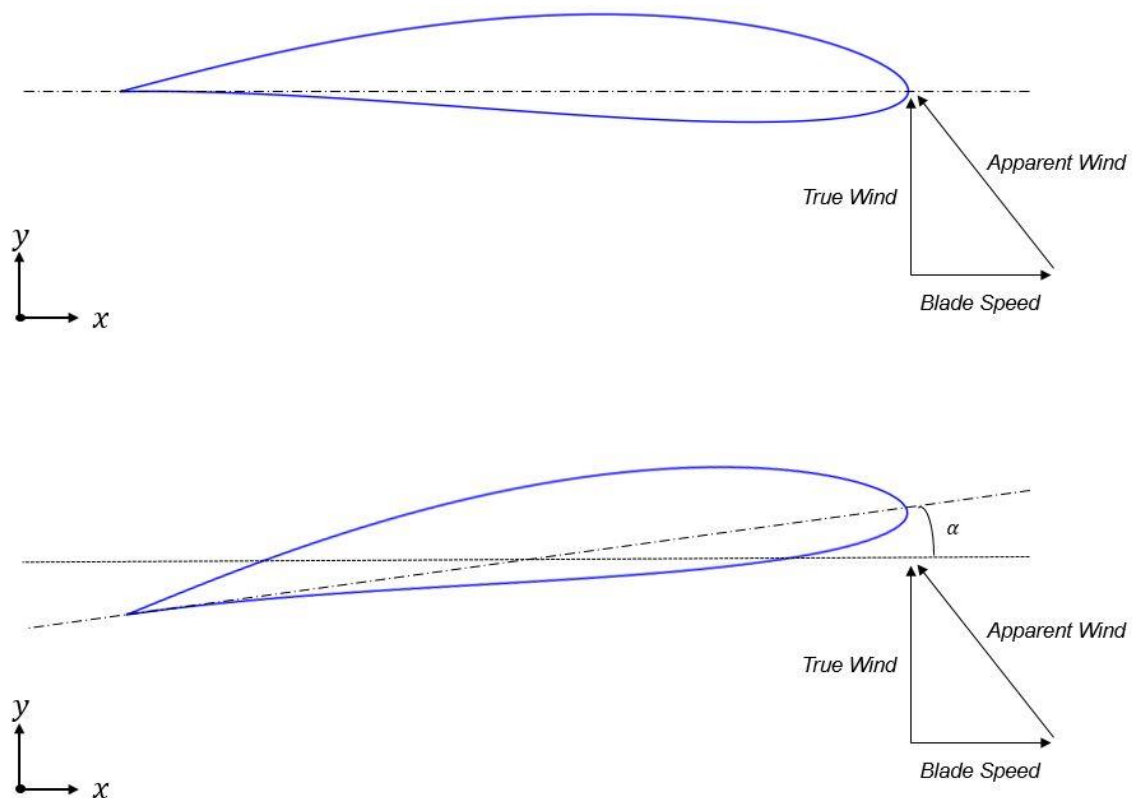


Figure 8-2 Positive Induced Twist Angle [9]

Furthermore, the deflections of the blade are similar based on the shown coordinate system. Hence, a negative deflection of the blade depicts a bending of the blade away from the tower. A positive deflection represents the bending of the blade towards the tower.

The **Table 8-1** is showing the achieved results of the structural sizing of the reference blade.

Table 8-1 Reference Design Results

| Layout | Mass [t] | Deflection min [m] | Deflection max [m] | Induced Twist min [°] | Induced Twist max [°] |
|-----------|----------|--------------------|--------------------|-----------------------|-----------------------|
| Reference | 19.166 | -2.76 | 8.98 | -0.49 | 1.39 |

The arising moments and forces, which include the aerodynamic and the inertia parts, are furthermore referred to as the reference moments and forces. They are set as the reference mark for further concepts, displayed with a relative value of 100 %. Furthermore, the loads from all RBE elements along the blade, compare **Figure 6-5**, are summed up for each reviewed force and moment.

8.2 „Technology 1“

Before reviewing the results of the structural concepts, the parametric study on the induced twist has to be evaluated. The induced twist shall serve as a boundary condition for the structural sizing of the c-beam and the swept beam concept.

8.2.1 Induced Twist

As mentioned in chapter 6.4, the influence of the induced twist is assessed based on the aerodynamic forces rather than the total loads, which include the inertia loads. By using only one structural layout during the induced twist investigation, it becomes obvious that the masses of different induced twist evaluations are suboptimal. During the investigation, the blade is stiffened more to limit the induced twist. Hence, the mass of the blade with limited induced twist is increasing, leading to higher inertia loads.

As described in chapter 7.1.3, the c-beam layout 6 is used during the induced twist investigation. This concept is leading to different induced twists in comparison to the

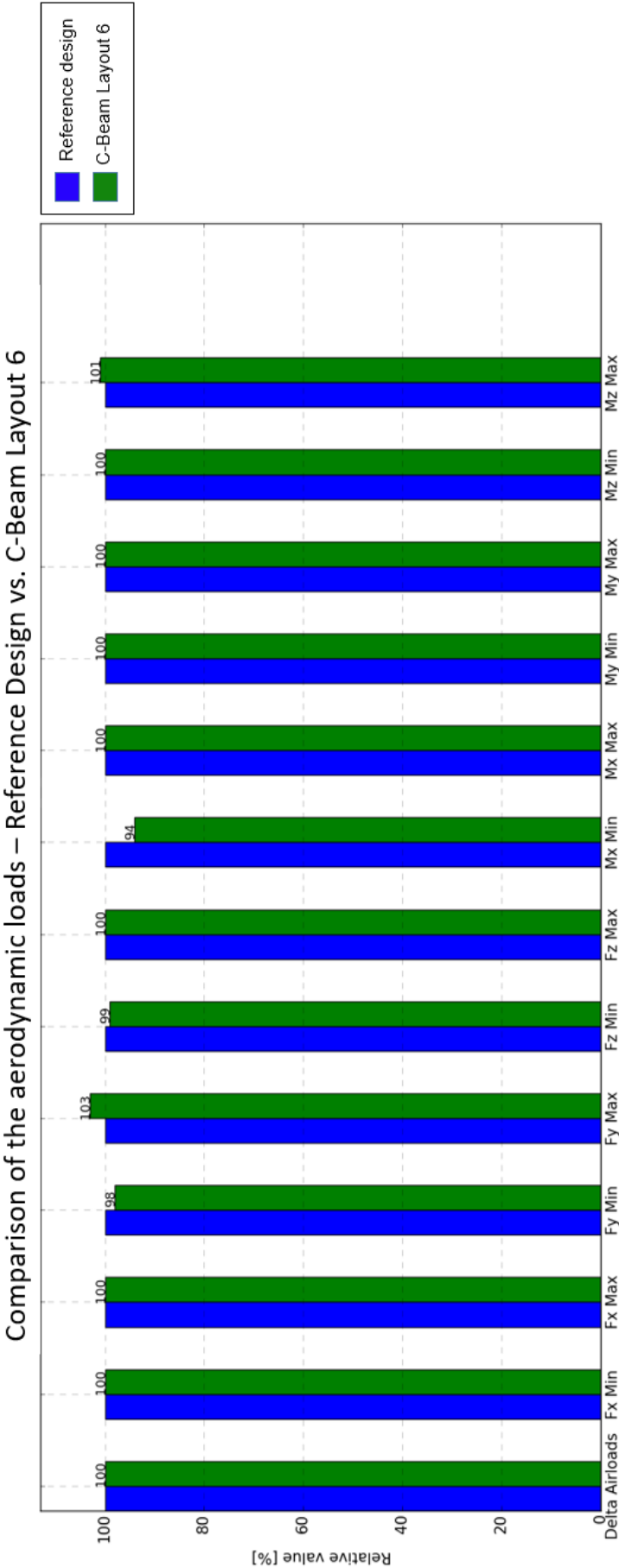
reference blade, because of the changed structural layout. The structural layout of the spars is shown in **Figure 7-12**. The achieved results for this concept without applying the induced twist constraint is shown in **Table 8-2**. The masses achieved are not evaluated for the previous introduced reasons.

Table 8-2 Induced Twist Base Concept Results

| Layout | Deflection min [m] | Deflection max [m] | Induced Twist min [°] | Induced Twist max [°] | Relative Delta of the loads of Air- |
|----------|-----------------------|-----------------------|-----------------------------|-----------------------------|--|
| C-Beam 6 | -2.83 | 9.10 | -0.57 | 1.69 | 1.0 |

The deflections of the blade in comparison to the reference design are only minor changed. The maximum value of the induced twist increases to 1.69° (1.39° in the reference design). The minimum induced twist is growing from -0.49° in the reference design to -0.57° . The increase in induced twist is expected as in this layout the shear centre is shifted towards the trailing edge, see chapter 7.1.3. Therefore, no aerodynamic load decrease is to be expected for these increased twists either. The results are supporting this expectation, as the overall delta of the relative aerodynamic loads in comparison to the reference design remain unchanged, see **Figure 8-3** “Delta Airloads”. However, when assessing each aerodynamic force for its own, a difference is observable.

Figure 8-3 Aerodynamic Loads - Reference Design vs. C-Beam Layout 6



As visible from the previous figure, the F_x and F_z forces, displaying the edgewise and flapwise forces, remain largely unchanged. The $F_{y_{min}}$ forces, displaying the radial acting forces, are decreasing by 2 %, while the $F_{y_{max}}$ forces are increasing by 3 %. The acting aerodynamic moments are equally unchanged. Only the $M_{x_{min}}$ moments, the moments acting in the flapwise direction, are reducing by 6 %.

In the following study, the induced twist is limited by the twist constraint. The maximum induced twist is limited as it leads to higher angle of attacks. Thus, a reduction of the maximum induced twist shall lead to lowered lift forces. A detailed overview about the achieved results is shown in **Table 8-3**.

Table 8-3 Limited Maximum Induced Twist Results

| <u>Limit of the maximum induced twist [°]</u> | <u>Max. Deflection [m]</u> | <u>Min. Deflection [m]</u> | <u>Max. Induced Twist [°]</u> | <u>Min. Induced Twist [°]</u> | <u>Relative Delta of the Aerodynamic Loads</u> |
|---|----------------------------|----------------------------|-------------------------------|-------------------------------|--|
| None | 9.10 | -2.83 | 1.69 | -0.57 | 1.0 |
| 1.4 | 8.50 | -2.56 | 1.24 | -0.44 | 0.97 |
| 1.2 | 8.50 | -2.51 | 1.22 | -0.40 | 0.98 |
| 1.0 | 8.27 | -2.39 | 1.05 | -0.39 | 0.95 |
| 0.8 | 8.10 | -2.24 | 0.86 | -0.38 | 0.93 |
| 0.7 | 7.85 | -2.23 | 0.70 | -0.25 | 1.3 |

Based on the shown results in **Table 8-3** several conclusion are drawn. First, for the sizing's limited to a maximum induced twist of 1.4° and 1.2° the same stiffness result is found. Therefore, a similar maximum induced twist is observable. Secondly, by limiting the maximum induced twist, the total aerodynamic loads are reduced. This trend is visible between a limitation of the maximum induced twist of 1.4° and 0.8° . At a limitation of 0.8° , the aerodynamic loads are reaching a maximum reduction of 7%, down to an overall relative difference of 93% in comparison to the reference design. A further limitation of the induced twist to 0.7° results into a load increase of 30 %. This sudden increase of the loads cannot be fully explained by the induced twist value. Since the limitation of the maximum induced twist leads to lower angle of attacks, it is possible that a negative lift force is induced at the blade tip at a maximum induced twist of 0.7° . By inverting the lift force at the blade tip, a change in flapwise deflections in the radial direction of the blade occur. This may lead to an increase of the aerodynamic loads.

The **Figure 8-4** shows the achieved results as a graph. From the graph it can be observed, that in a limitation range of 1.4° to 0.8° , the aerodynamic loads are lowered. This range is further described as “TR1” (Twist Range 1). The “TR2” (Twist Range 2) is depicting the area of an induced twist between 1.4° and 1.7° . In this design range, the aerodynamic loads remain largely unchanged. A load increase results from limiting the maximum induced twist below 0.8° .

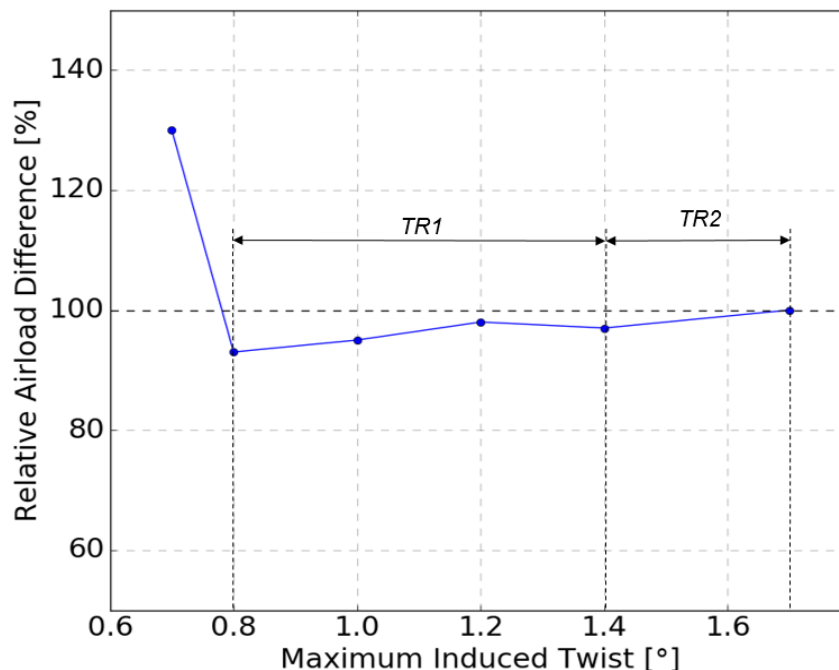


Figure 8-4 Relative Load Difference vs. Maximum Induced Twist

The reduction of the total aerodynamic loads in the “TR1” is represented by following **Figure 8-5**, which shows the acting aerodynamic forces at 1.4° maximum induced twist. The load reduction of the total aerodynamic loads are resulting from reduced $F_{y_{max}}$ forces and $M_{x_{min}}$ moments. At a maximum induced twist angle of 1.4° , these forces are lowering down to 89%.

Figure 8-6 displays the aerodynamic forces for a maximum induced twist of 0.8° . The $F_{y_{max}}$ forces are lowering even more down to 11 %. In contrast, the $M_{x_{min}}$ moments are increasing from the previous achieved 89 % up to 124%. The $M_{x_{max}}$ moments are similarly increased by 3 %. Most of the other forces and moments are lowered by 2 – 3 % in comparison to the reference design. An exception from this are the F_z forces, which are increasing by a relative amount of 2 %.

As an overall conclusion from the performed study, the relative values of the aerodynamic forces are reduced with a lower maximum induced twist down to a limit of 0.8° . A further limitation of the maximum induced twist results in a load increase of 30 %. Therefore, a maximum induced twist between 1.4° and 0.8° seems to be preferable to achieve a load reduction. The “TR1” is therefore displaying the preferred maximum induced twist range.

Figure 8-5 Aerodynamic Loads - Reference Design vs. C-Beam Layout 6 limited to 1.4° Induced Twist

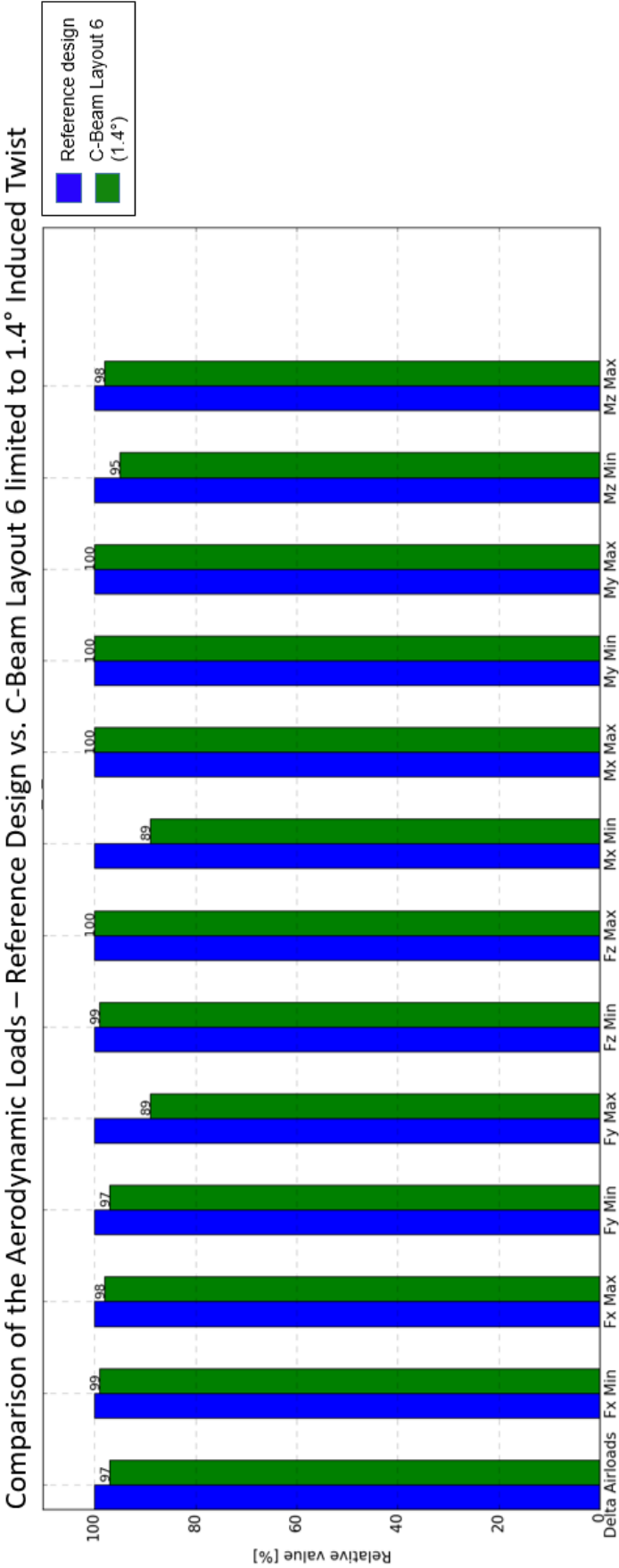
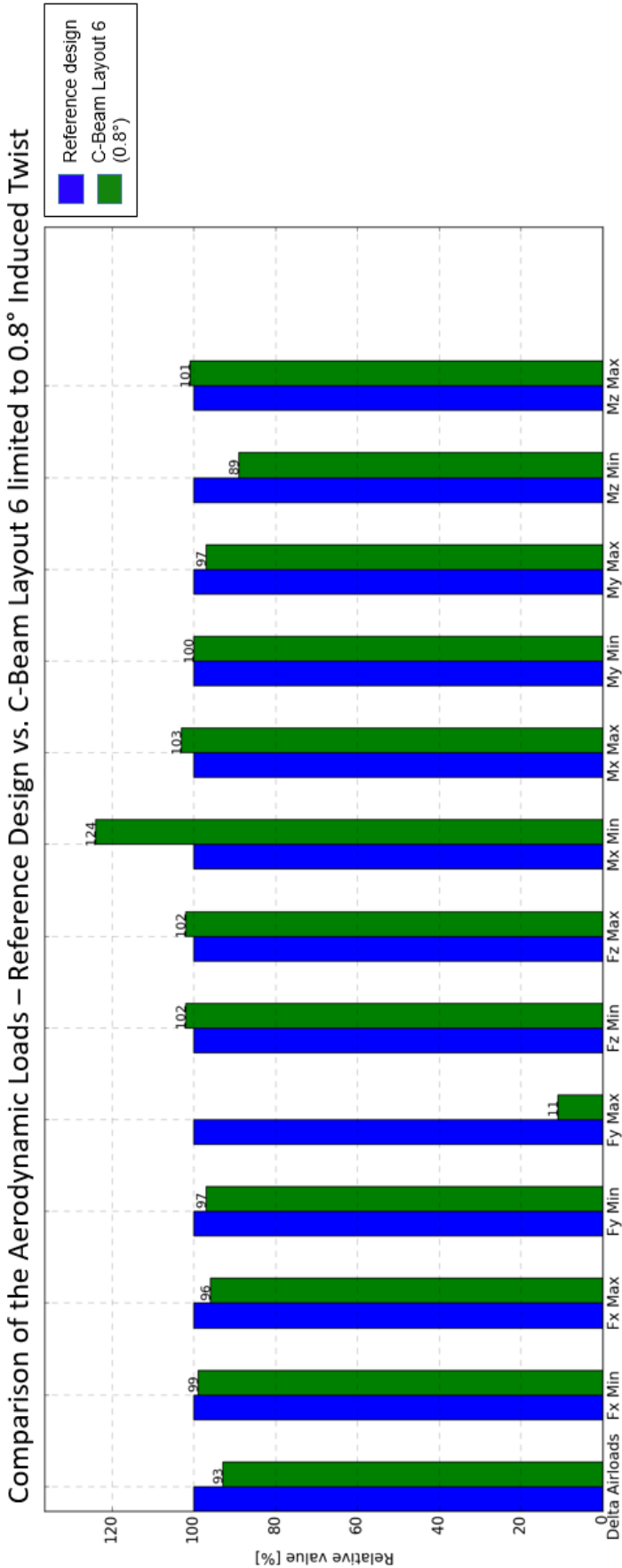


Figure 8-6 Aerodynamic Loads - Reference Design vs. C-Beam Layout 6 limited to 0.8° Induced Twist



While the presented results indicate a conclusive trend, several outliers are also observed in the investigation. It became clear that some material layouts of the blade for the required stiffness's are resulting into a non-convergence of the iterative loads-sizing process. This non-convergence is identified by a drastic load increase between iterations of the load-sizing process. These drastic increased loads are explainable by oscillations of the structure in the load simulation. This is depicted by the assessment of the deflections of the structure during the sizing process. This shall be shown exemplarily by the limitation of the maximum induced twist to 1.3° . With this limitation, the above mentioned oscillations that occur during the simulation for several concepts become clear. **Table 8-4** indicates the creation of oscillations in the simulation by comparing deflection results before the drastic load increase and after the drastic load increase. The first shown values are corresponding to the sizing where no oscillations occur in the simulation. The second value links to the sizing results with the drastic increased loads.

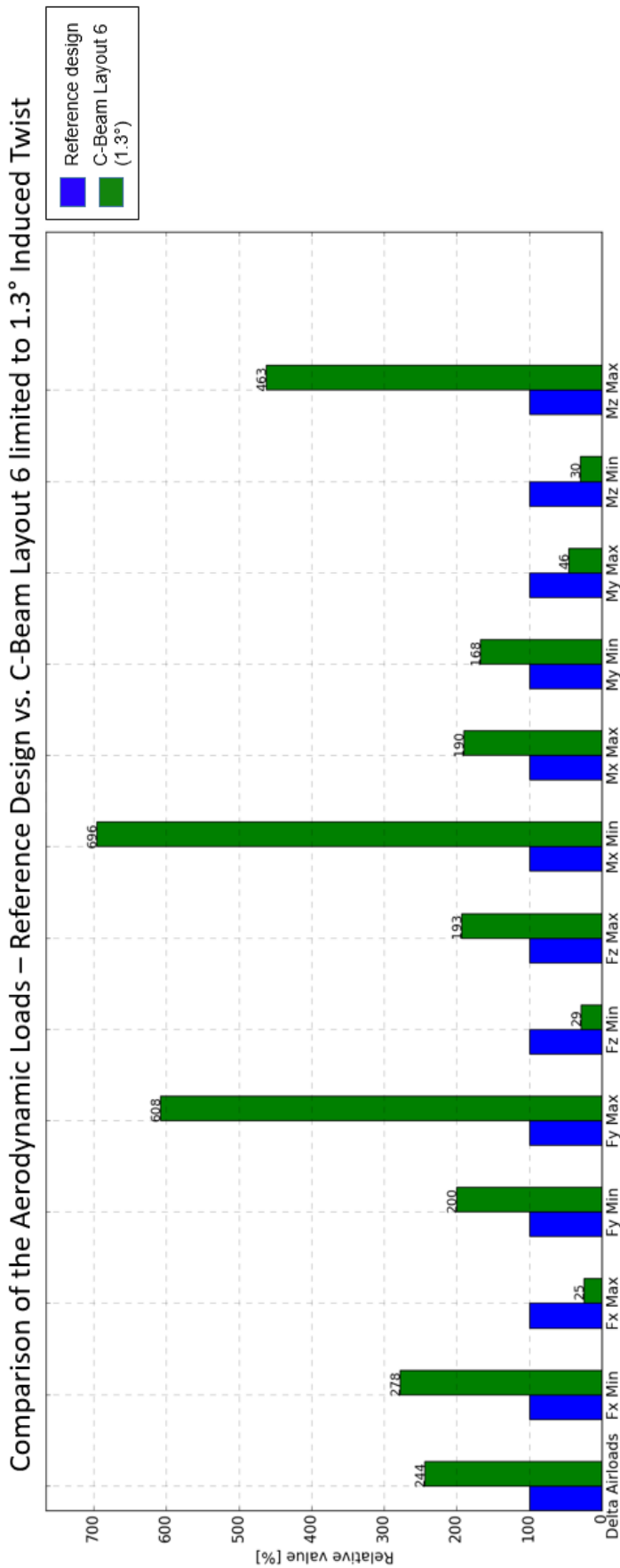
Table 8-4 Induced Twist Concept Non-Convergence Example

| Layout | Deflection min [m] | Deflection max [m] | Induced Twist min [°] | Induced Twist max [°] |
|--------------------------|-----------------------|-----------------------|--------------------------|--------------------------|
| C-Beam 6 (1.3°) | -2.56 / -8.62 | 8.66 / 8.69 | -0.43 / -1.35 | 1.29 / 1.36 |

An oscillation in the bending wise direction of the blade becomes obvious, as the minimum deflection values, so the blade deflection against wind direction, increases from -2.5 m up to -8.6 m .

This non-convergence based on oscillations is observed during several investigations for the maximum induced twist. The result of such a non-convergence sizing is a blade with an unreasonable high mass to withstand the loads created by the oscillations. Due to these circumstances, the twist constraint for the evaluations of the following structural concepts is neglected. The risk of generating undesirable oscillations in the structure caused by a stiffness increase is too great. Promising concepts may thus become not assessable. The following **Figure 8-7** shows the occurring increased aerodynamic loads for the limitation of 1.3° maximum induced twist during a simulation with oscillations.

Figure 8-7 Aerodynamic Loads - Reference Design vs. C-Beam Layout 6 limited to 1.3° Induced Twist



8.2.2 C-Beam

As described in the previous chapter, the structural concepts are optimized without the usage of the twist constraint. The induced twist is only dependent on the concept itself. Although no twist constraint is used, the concepts can nevertheless be compared to the results of the twist study to assess the aerodynamic load reduction.

A general overview of the achieved results for the different c-beam concepts are displayed in **Table 8-5** on the following page.

Several of the concept are leading to a non-convergence of the load-sizing process, similar to the twist constraint investigations. This non-convergence is equally observable by drastic increased loads between iterations of the load-sizing process. The visible oscillations differ from the previous oscillations, as they are torsional. This is shown in the table by the induced twist values, which are increasing greatly during the iterative process, showing that the upper and lower boundary of the induced twist become similar and their values are unreasonable high. Again, the first shown values are corresponding to the sizing where no oscillations occur in the simulation. The second value links to the sizing results with the drastic increased loads

Table 8-5 C-Beam Concept Results

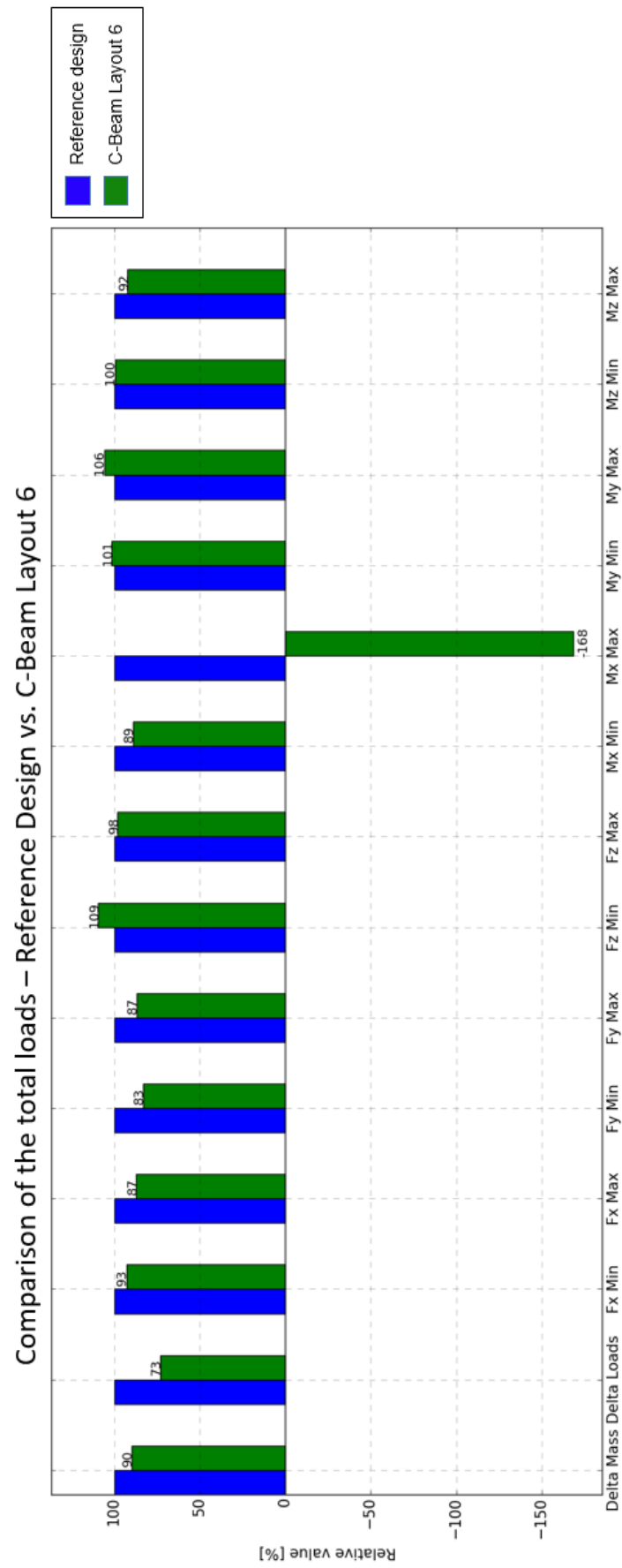
| <u>LAYOUT</u> <u>NUMBER</u> | <u>MASS [t]</u> | <u>MAX. DEFLECTION</u> [m] | <u>MIN. DEFLECTION</u> [m] | <u>MAX. INDUCED TWIST</u> [°] | <u>MIN. INDUCED TWIST</u> [°] | <u>CONVERGED</u> |
|--------------------------------|-----------------|-------------------------------|-------------------------------|----------------------------------|----------------------------------|------------------|
| Reference | 19.166 | 8.98 | -2.76 | 1.39 | -0.49 | Yes |
| 1 | 62.46 / 149.17 | 8.02 / 10.04 | -7.42 / -6.61 | 9.42 / 19.65 | -8.91 / -12.55 | No |
| 2 | 24.16 / 97.79 | 11.14 / 9.79 | -3.20 / -8.12 | 4.53 / 19.01 | -2.76 / -18.11 | No |
| 3 | 30.14 / 131.31 | 9.49 / 9.36 | -2.57 / -12.88 | 2.87 / 12.88 | -2.15 / -13.01 | No |
| 4 | 18.66 / 63.37 | 10.05 / 10.07 | -2.97 / -9.23 | 2.27 / 13.06 | -0.77 / -13.29 | No |
| 5 | 26.63 | 8.09 | -2.59 | 1.29 | -0.45 | Yes |
| 6 | 17.18 | 9.10 | -2.83 | 1.69 | -0.57 | Yes |

Besides the non-converged structural layouts, the layout 5 and 6 deliver assessable results. The structural layout 5 achieves a mass of roughly 26 t . This is a drastic increase from the reference design mass. The deflection and the induced twist are lowered in comparison to the reference design. The maximum induced twist is in the “TR1” of the induced twist study.

The structural layout 6, which corresponds to the used layout for the induced twist investigations, reaches a lower mass in comparison to the reference design of only 17.18 t . This is a relative reduction of the mass of about 10 %. In contrast to the layout 5, the layout 6 has slightly increased deflections and an increased induced twist. The induced twist in comparison to the reference design is increased from 1.39 ° up to 1.69°. The total load comparison of the layout 6, including the inertia loads from the simulation, is shown in **Figure 8-8**.

In comparison to the reference design, the overall loads are reduced by 27 %. All normal forces, except the $F_{z_{min}}$ are lowered, resulting in a relative value between 83 – 98 %. The $F_{z_{min}}$ force is increased by 9 %. The $M_{x_{max}}$ values are inverted and increased by additional 68 %.

Figure 8-8 Load Comparison for C-Beam Layout 6

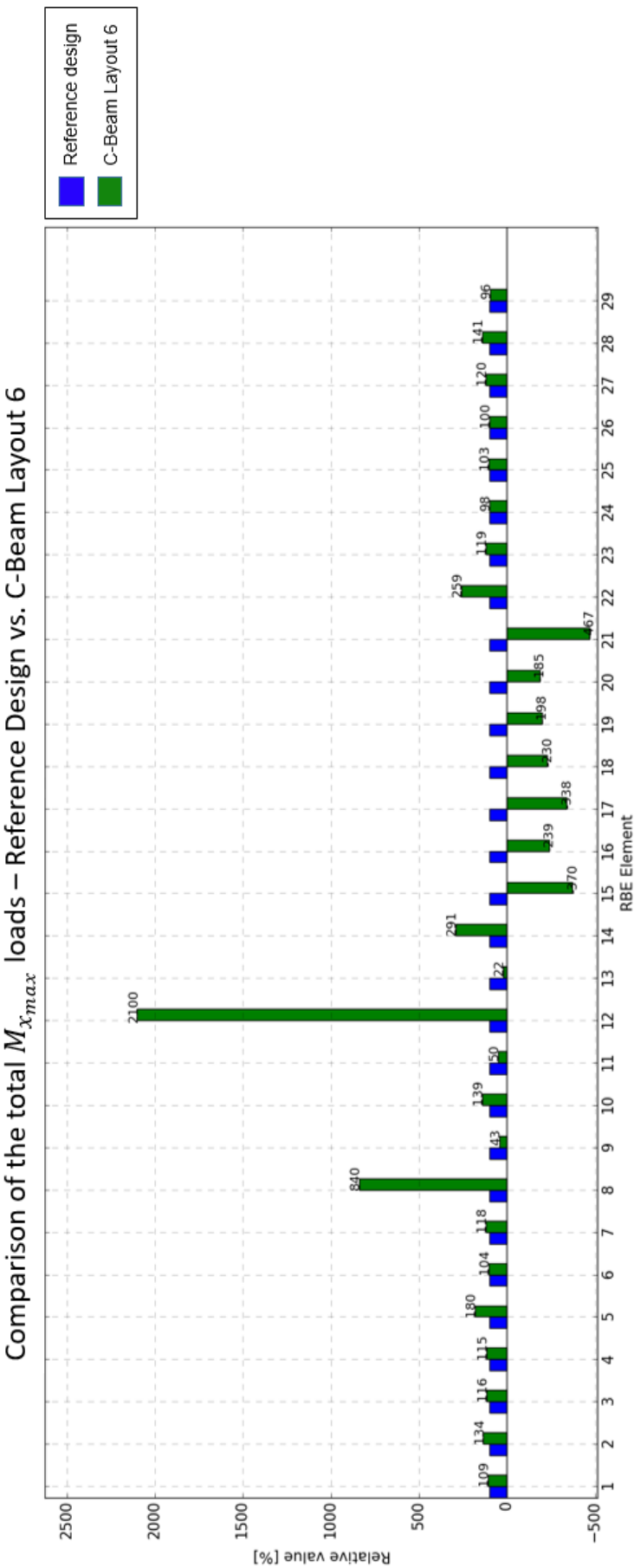


To understand the inversion of the $M_{x_{max}}$ moment more precisely, the moments for each single RBE element in comparison to the reference design are furthermore shown in **Figure 8-9**. The RBE element 29 is at the tip of the blade, the RBE element 1 shortly after the blade root. The RBE element 0 is not shown, because this RBE element is part of the blade clamping. Thus, the node forces in this RBE element are always equal to 0.

As visible from **Figure 8-9**, the different induced twist in comparison to the reference design is affecting all $M_{x_{max}}$ moments along the blade. This difference might not only be resulting from different aerodynamic loads. The inertia loads are dependent on many factors, including the material distribution and corresponding eigenfrequencies. The $M_{x_{max}}$ moments are mainly increasing for all RBE elements before the RBE element 15. In contrast, the RBE elements from 15 to 21, so the RBE elements corresponding to a total blade length from 40 to 56 m, have an inverted moment. Their relative value is also further increased by a factor of roughly 3. Based on this observation, it can be concluded that the inversion of $M_{x_{max}}$ is primary influenced by the inverted acting moments at the RBE elements 15 – 21.

The other forces acting on the RBE elements for the c-beam concept 6 are included in Appendix A.

Figure 8-9 $M_{x_{max}}$ Load Comparison for C-Beam Layout 6



Concluding the introduced results for the c-beam concept: The instability added by the reduction of the front spar length leads to non-realizable layouts. For the c-beam, the occurrence of these non-realizable layouts is expected, as the stability of the blade is strongly reduced by reducing the length of the front spar. Based on the minimum and maximum induced twist values, it is observable, that the amplitude of the torsional oscillations is influenced by the total length of the front spar. This supports the explanation for the previous mentioned instability problem. Furthermore, these non-realizable layouts are forming the boundary condition for the parameter space for a possible following more in-depth optimization. A maximum relative reduction of 13 % marks the boundary for the length reduction of the front spar based on the layout 5. The evaluation of layout 6 results into a load reduction and therefore a mass reduction of the blade about 10 %. The load reduction is visible at nearly all normal forces. The general concept is therefore proven. However, this mass reduction is not to be expected with this layout, since the maximum induced twist is increased compared to the reference design. The corresponding aerodynamic loads of this concept, which are presented in chapter 7.1.1, underline this assumption. Compared to the reference design, there is no aerodynamic load reduction. The load reduction achieved with this layout is therefore based on the reduction of inertial loads. Additionally, the consideration of the individual RBE element node forces reveals which elements cause an inversion of the $M_{x_{max}}$ moments. The corresponding maximum induced twist at the c-beam layout 6 is in the “TR2”, see **Figure 8-10**. Therefore, the aerodynamic loads are mainly unchanged. Thus, the load reduction has to be achieved by lower inertia loads.

The abbreviation “C” stands for c-beam. The depicted number refers to the layout number.

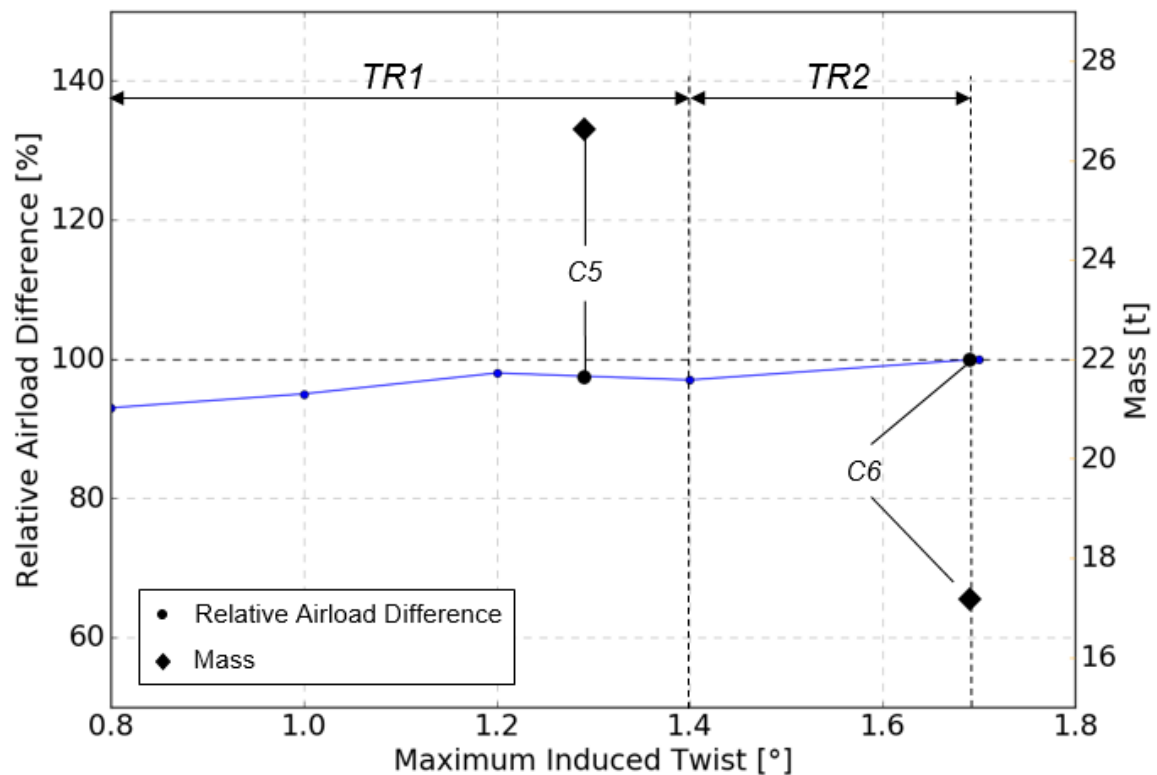


Figure 8-10 Relative Load Difference vs. Maximum Induced Twist C-Beam Concept

8.2.3 Swept Beam

A general overview of the achieved results for the swept beam layouts is shown in **Table 8-6** on the following page.

Similar to the c-beam concept, the first layout for the swept beam, layout 1, shows a non-convergence. In contrast to the c-beam, the occurring oscillations seem to be conditioned by the bending of the blade. This is indicated by the minimum deflections, which are reaching an absolute value of up to -9.23 m , while comparable converged layouts are achieving a minimum deflection of roughly -2.5 m .

Table 8-6 Swept Beam Concept Results

| <u>Layout Number</u> | <u>Mass [t]</u> | <u>Max. Deflection [m]</u> | <u>Min. Deflection [m]</u> | <u>Max. Induced Twist [°]</u> | <u>Min. Induced Twist [°]</u> | <u>Converged</u> |
|--------------------------|-----------------|--------------------------------|--------------------------------|-----------------------------------|-----------------------------------|------------------|
| Reference | 19.166 | 8.98 | -2.76 | 1.39 | -0.49 | Yes |
| 1 | 86.52 / 84.97 | 9.06 / 9.43 | -9.23 / -9.05 | 17.11 / 14.48 | -3.71 / -3.89 | No |
| 2 | 24.99 | 8.21 | -2.42 | 1.16 | -0.42 | Yes |
| 3 | 17.44 | 7.05 | -2.08 | 1.30 | -0.37 | Yes |
| 4 | 25.57 | 8.05 | -2.24 | 0.98 | -0.36 | Yes |

All converged concepts are resulting in a maximum induced twist in the "TR1" range, see **Figure 8-11**. Thus the aerodynamic forces are reduced for these concepts. Although the aerodynamic forces are reduced, the layout 2 and 4 show a mass increase. Accordingly, this mass increase must result from increased inertial loads. Layout 3 achieves a mass reduction to 17.44 t. This corresponds to a relative mass decrease of 8 %.

The abbreviation "S" stands for swept beam. The depicted number refers to the layout number.

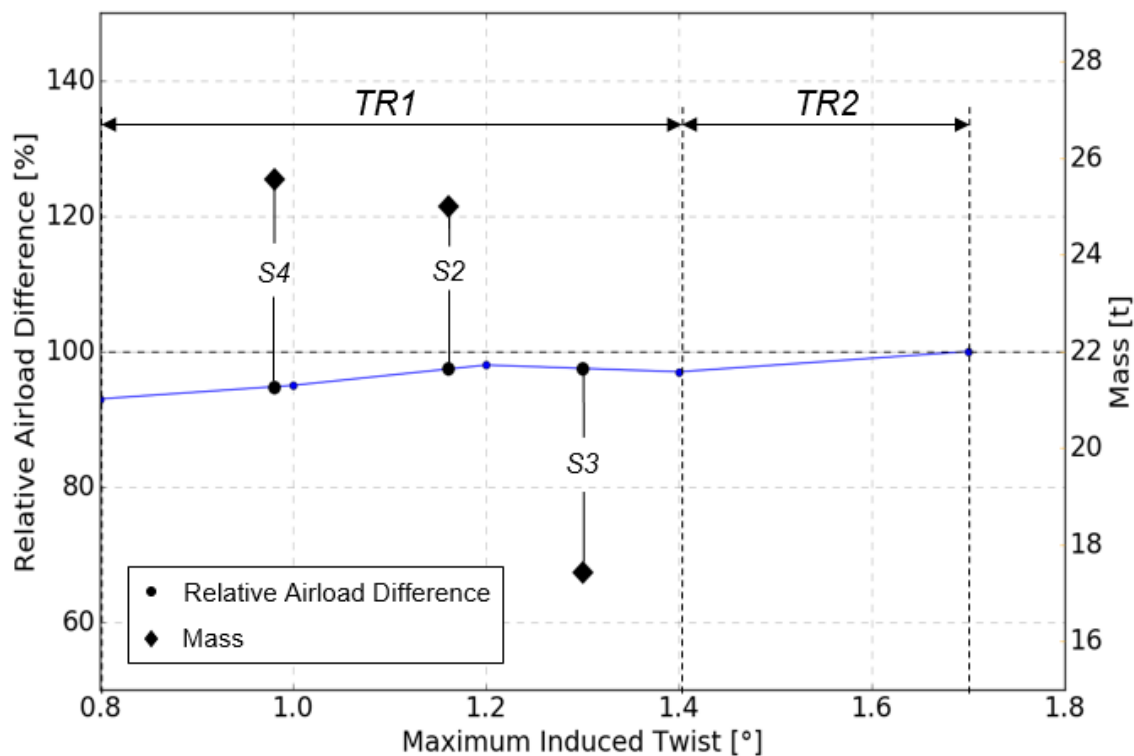


Figure 8-11 Relative Load Difference vs. Maximum Induced Twist Swept Beam Concept

The load comparison between the reference design and the layout 3 of the swept beam is shown in **Figure 8-12**. The comparison shows similarities to the investigated c-beam layout 6. The total loads are reduced by 8 %. All normal forces are lowered, resulting in a relative value between 93 – 99 %. The $M_{x_{max}}$ values are similar to the c-beam layout 6 inverted and increased by –51 %. In contrast, the M_y moments at the swept beam layout are additionally reduced by up to 27 %.

The $M_{x_{max}}$ moments for each single RBE element in comparison to the reference design are shown in **Figure 8-13**. The inversion is very similar to the c-beam layout 6. Again, the RBE elements 15 – 21 are inverted. The other forces acting on the RBE elements for the swept beam concept 3 are included in Appendix B.

Figure 8-12 Load Comparison for Swept Beam Layout 3

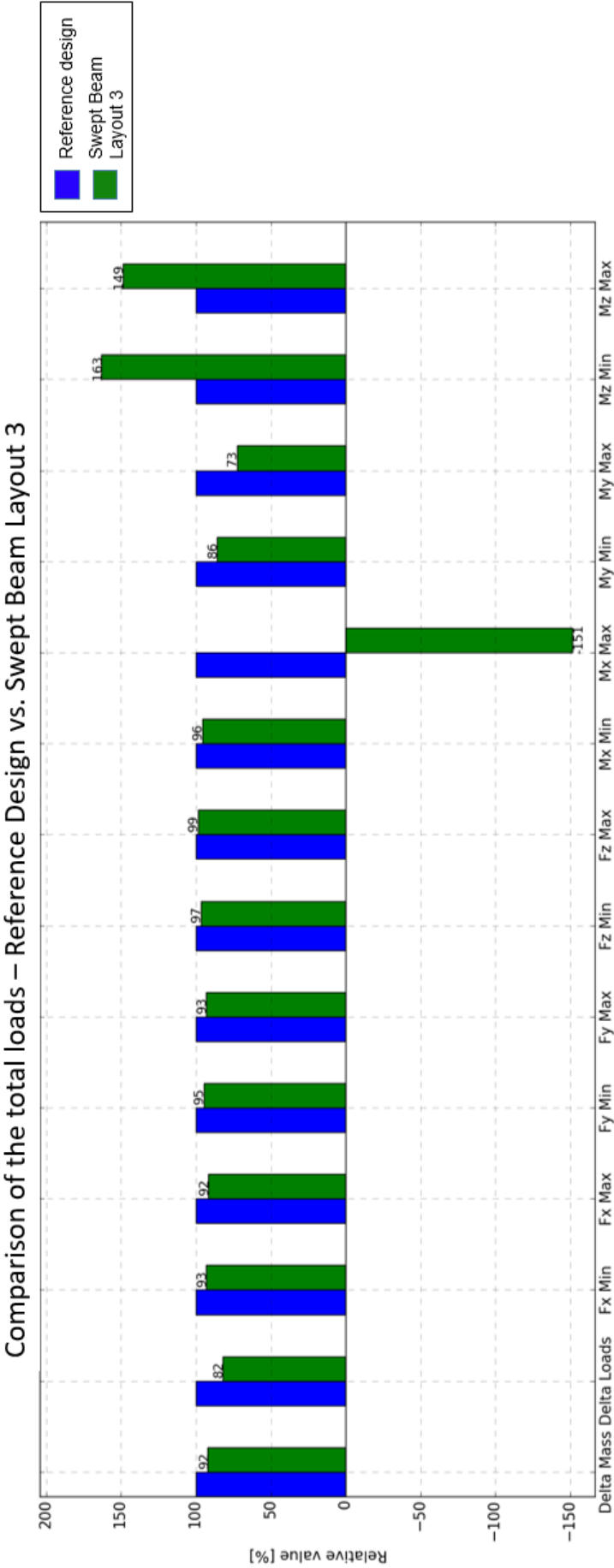
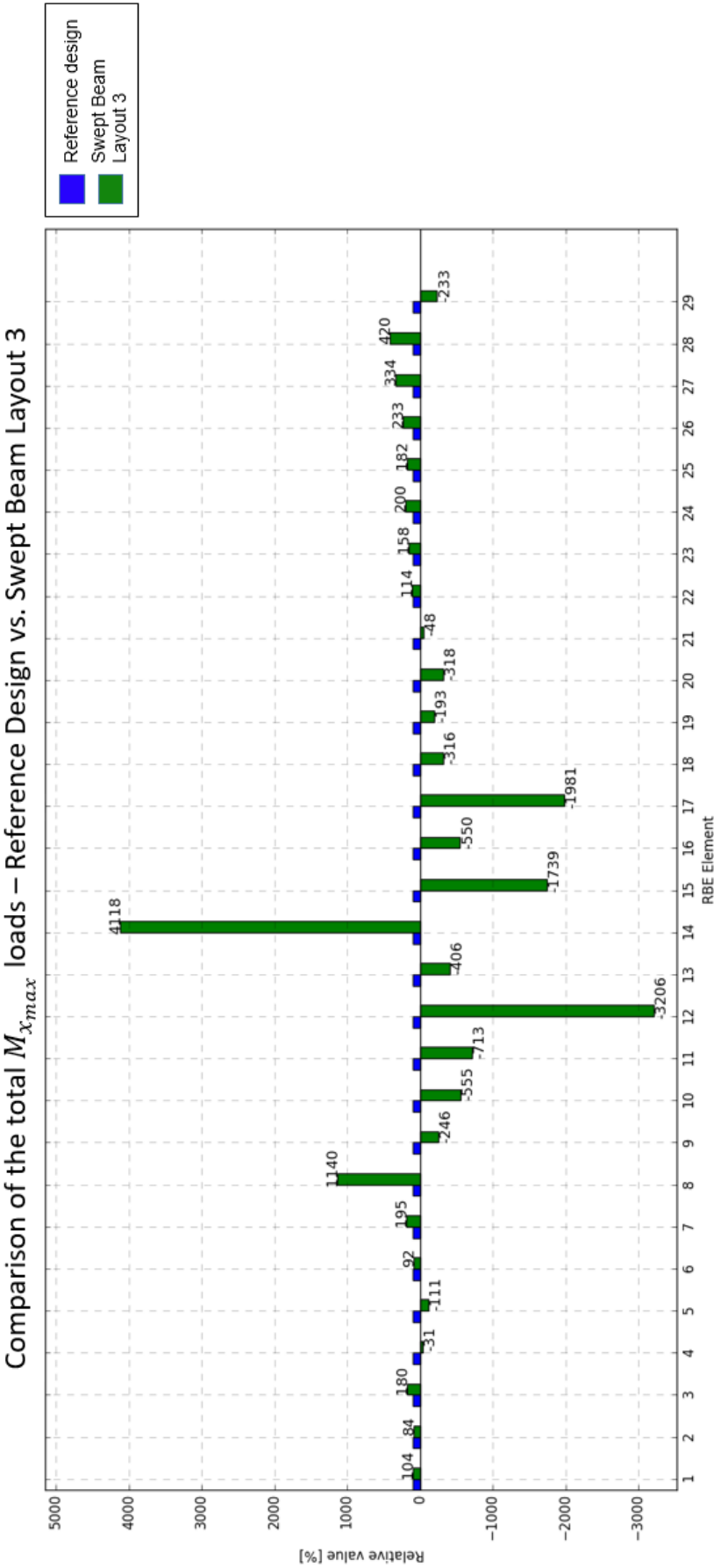


Figure 8-13 $M_{x_{max}}$ Load Comparison for Swept Beam Layout 3



For the swept beam concept, it can be concluded that the general concept is similar proven. The layout 3 leads to a mass reduction of 8 %. Equal to the c-beam, all normal forces are lowered. The maximum induced twist of this layout is in the “TR1”. Because of the non-converged layout 1, the parameter space for the concept is further adaptable for in-depth optimizations. The pre-sweep start should be adapted to a minimum of 50 %.

8.2.4 Conclusion

Overall, for the structural concepts of „Technology 1“, it is concludeable that both assessed structural concepts are able to reduce the acting forces and moments on the blade leading to a mass decrease. The best c-beam layout reaches a load reduction of 27 %. In contrast, the best swept beam design reaches a load reduction of 18 %. These load reductions are resulting into a blade design with a lower mass compared to the reference design. Furthermore, the parameter space for both concepts is further localized by the non-converged concepts. An optimization algorithm might therefore find concepts, which are leading to a greater load reduction by investigating a larger number of parameter sets. Therefore, it cannot be concluded that the c-beam concept leads in general to a larger load reduction than the swept beam concept.

The classification of the evaluated concepts into the developed twist ranges “TR1” and “TR2” are shown in **Figure 8-14**. The abbreviation “S” stands for the swept beam, the abbreviation “C” for the c-beam and the abbreviation “Ref” for the reference design. The numbers are referring to the structural layout number.

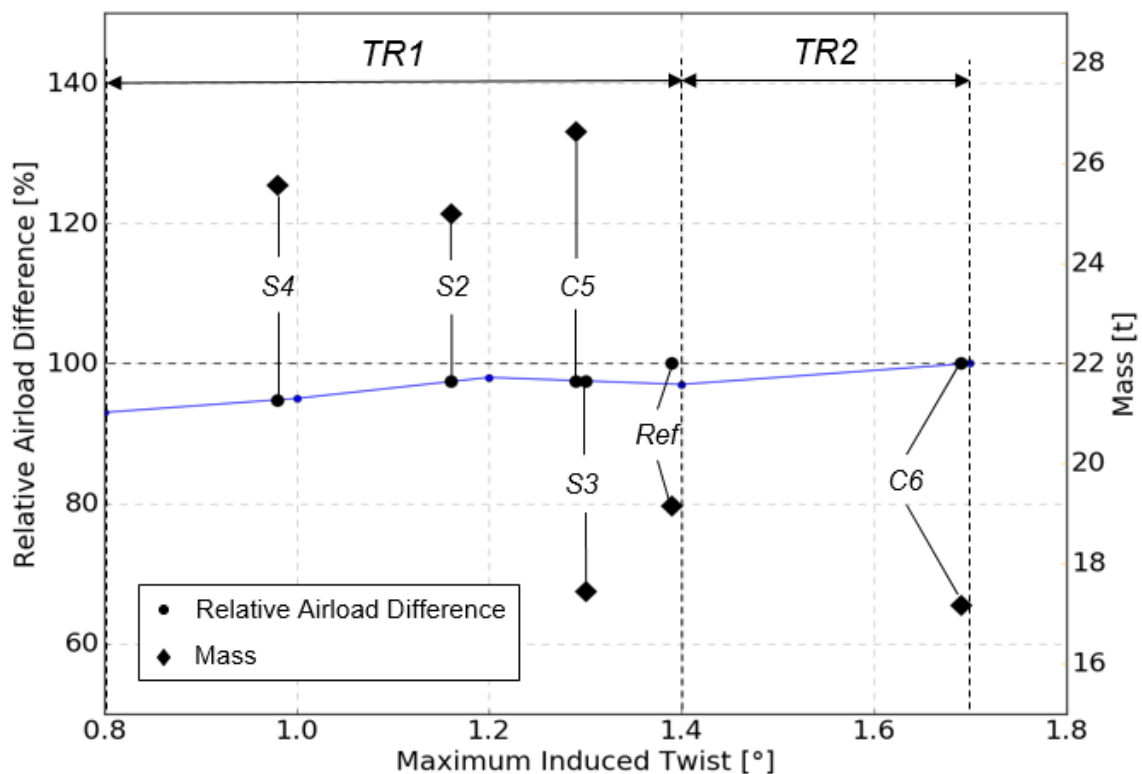


Figure 8-14 Relative Load Difference vs. Maximum Induced Twist of the Investigated Structural Layouts

The c-beam layout 6, “C6”, is located in the “TR2” of the induced twist study. The aerodynamic loads remain therefore largely unchanged. Nevertheless, the concept reaches the lowest mass of all reviewed concepts. The swept beam design 3, “S3”, is located in the “TR1”. Here, a mass decrease is achieved, which supports the results of the induced twist study.

In contrast, the other evaluated structural concepts “S4”, “S2” and “C5” are in the desired “TR1”, but are leading to a mass increase. The aerodynamic loads are thus reduced, but the total loads increase. Therefore, the corresponding inertia loads of the different concepts must be increased, leading to a higher mass of the structure. Finally, it must be concluded from the comparison of the induced twist study with the concepts results, that the maximum induced twist cannot be regarded as the sole parameter for a total load reduction. However, it is not possible to derive all determining parameters from the studies presented. In the following, different approaches are described, which explain the deviations observable from the results. Furthermore, different parameters are described, which may have an influence on the total load reduction.

On the one hand, it is possible that the induced twists resulting from the extreme load tables deviate from the minimum and maximum values achieved in the simulation. Thus, the concepts may not reflect the actually achieved induced twists. This problem could be solved by creating an additional load case from the load simulation, which corresponds to the times of the actual maximum and minimum twist. The evaluation of the load reduction would continue to be performed using the extreme load tables, but the corresponding induced twist would be evaluated from the newly created dynamic load cases.

Another similar explanation is that the maximum and minimum values of the induced twist do not act at the times of the occurring maximum loads. Thus, the current approach based on the assessment of the limits of the induced twist would not accurately reflect the resulting load reduction. The solution here would not be to consider the limits of the induced twist resulting from the extreme load tables, but possibly an average value of the induced twist occurring at the maximum loads.

Based on the first solution approaches presented, it would still be advisable to consider the actual angle of attack. As already mentioned, the angle of attack also depends on the pitch of the blade. Since different load scenarios are evaluated in

which the turbine operates with different blade pitches, it is possible that the weighted induced twist does not correspond to the actual change of the angle of attack. Accordingly, a modified process should evaluate not only the induced twist as a design parameter, but also the actual angle of attack.

In addition, the flapwise deflection of the blade is not interpreted as a determining parameter in the current evaluation. However, this deflection also has an influence on the angle of attack. As a solution, a constraint could be introduced to limit the influence of the deflection of the blade by not only limiting the maximum deflection of the blade, but also the minimum deflection. Thus, equivalent conditions would be created for the evaluation of the load reduction by the induced twist.

A further possibility is that the results obtained are meaningful, but the concepts that show an increased mass despite their reduced aerodynamic loads show suboptimal eigenfrequencies. Thus, although the aerodynamic loads would be reduced, the inertial loads would be increased. A further design constraint, which limits the eigenfrequencies to an optimal range by minimizing the resulting inertial loads, could produce significantly improved results. This can also counteract the oscillations occurring in the load simulation and thus increase the currently limited parameter space of the concepts.

Based on the approaches described above, the focus for future investigations should therefore be on identifying the relevant parameters resulting from the loads process. In addition, the introduction of further restrictions of the structural design process, such as the limitation of natural frequencies, can make the results more conclusive. In addition, the parameter space for the concepts can also be increased in this way.

8.3 „Technology 2“

When reviewing the results for „Technology 2“, the active flap towards the blade tip, it should be recognized that no load evaluation is done for this concept. The basic design with the rear spar moving in the direction of the flap cut-out is dimensioned using the reference loads of the blade. Based on the flap depth of 30 % of the local chord length, the rear spar is shifted to a relative chord wise position of 0.65 in the area of the flap cut-out from 66 – 75 *m* of the total blade length. The displacement of the spar also increases the area of the spar caps in this concept. This should counteract the reduced stiffness of the structure due to the flap cut-out. The following **Table 8-7** shows the achieved results for the blade with the flap cut-out and the moved rear spar.

Table 8-7 „Technology 2“ Results

| Mass [t] | Deflection [m] | min | Deflection max [m] | Induced Twist min [°] | Induced Twist max [°] |
|----------|----------------|-----|--------------------|-----------------------|-----------------------|
| 24.50 | -2.02 | | 9.95 | -1.54 | 0.61 |

The mass of the adapted blade increases by approx. 5 *t* compared to the reference design. The flap deflections and the induced torsion are slightly increased. This does not necessarily meet expectations, since the increase of the area of the spar caps significantly increases the flapwise stiffness as well as the torsional stiffness. It must therefore be concluded that the increase of the area of the spar caps is not sufficient to compensate for the reduced stiffness of the blade.

Since the load reduction achieved by the flap is not currently evaluated, it is possible that the total mass of the blade will be reduced using the actual loads. However, the shown mass clearly indicates that a significant load change must be achieved.

Overall, a load simulation that includes the effects of the flap must be set up for a general evaluation of the concept. This is indispensable in order to reach a precise conclusion on the effectiveness of the concept. Furthermore, it must be noted that the cost savings resulting from a possible mass reduction must be greater than the costs resulting from the implementation of the flap.

9 Conclusion and Outlook

This thesis provides design studies for reducing the acting forces and moments on wind turbine rotor blades. Within these studies, different structural design concepts have been assessed, that shall lead to the load reduction. The overall objective was to decrease the total mass of a wind turbine rotor blade.

The proposed structural designs were derived from two main technologies. First, the aeroelastic tailoring, which couples the bending of the blade to a torsion. Second, an active flap at the trailing edge of the blade. For both technologies, automated sizing processes have been developed. For the aeroelastic tailoring, those automated sizing processes are iteratively assessing the loads acting on the structure and the blade is correspondingly sized. A combination of these individual processes is not yet state of the art. Thus a way for the combination of the individual processes was pointed out, which can be further optimized in the future. Furthermore, a twist constraint has been implemented into the automated sizing processes. This constraint allowed performing an induced twist study to determine the impact of the maximum induced twist on the aerodynamic loads.

The results of this induced twist study showed that a reduction of the aerodynamic loads is achieved when the maximum induced twist is in a range between 0.8° and 1.4° . The assessment of the aeroelastic tailoring has shown, that a c-beam concept as well as a swept beam concept is leading to a mass reduction of 8 – 10 % in comparison to the reference rotor blade. When classifying the results of the structural concepts in the induced twist study, it was found that the results do not correlate. Therefore, it has to be concluded, that the maximum induced twist is not the sole design parameter for a load reduction. The adaptation of the structural layout for the flap has depicted, that the flap cut-out leads to a strongly increased mass of the blade. A load reduction of several percent has therefore to be reached to decrease the total mass of the blade.

For further studies of the aeroelastic tailoring it is important to further investigate the dynamic behaviour of the blade in a load simulation. The relevant dynamic state of the induced twist is to be found. This can then be used as a boundary condition in subsequent investigations. For further studies of the active trailing edge flap, it is important to quantify the load reduction achieved by the flap. Only in this way can a statement be made about the effectiveness of the concept.

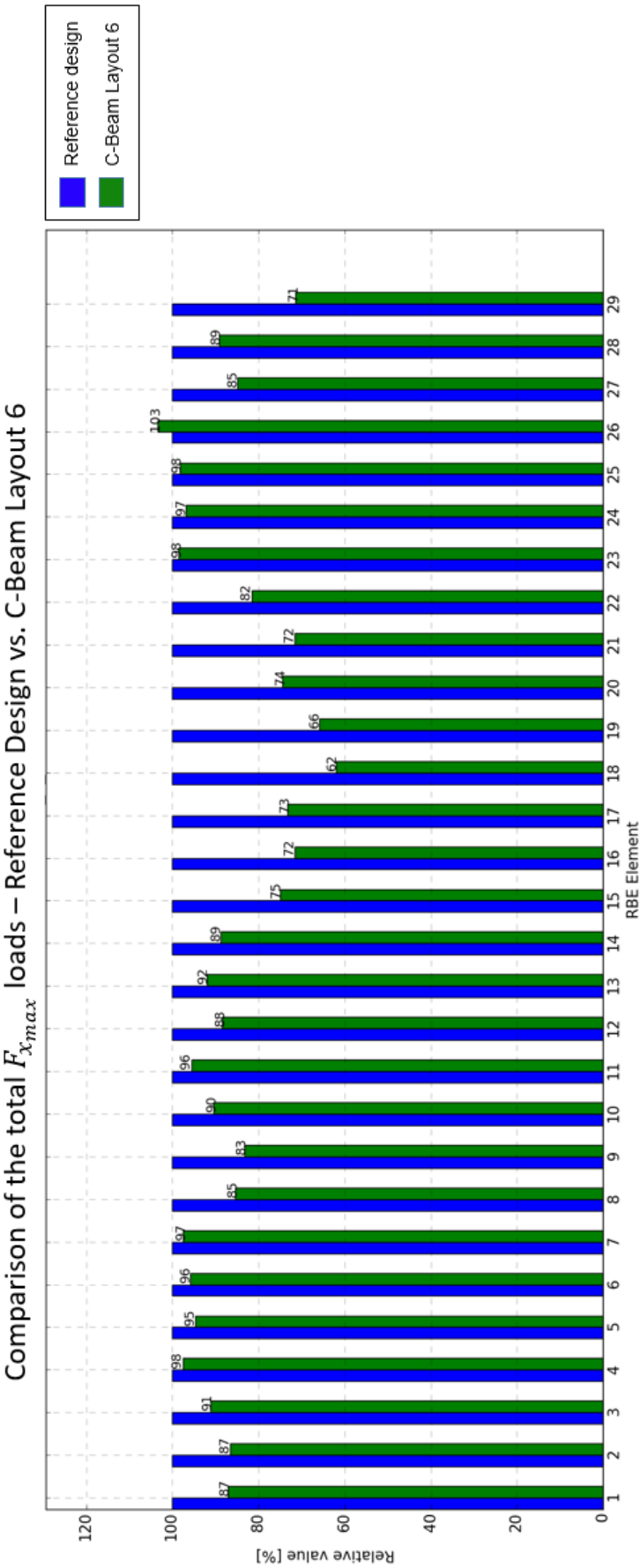
Bibliography

- [1] E. Hau, "Windkraftanlagen," Springer Berlin Heidelberg, 2014, p. 284
- [2] E. Hau, "Windkraftanlagen," Springer Berlin Heidelberg, 2014, p. 285
- [3] E. Hau, "Windkraftanlagen," Springer Berlin Heidelberg, 2014, p. 302 ff.
- [4] Ceyda Icpinar Dr. Elia Daniele Dr. Johannes Riemenschneider Dr. Michael Hölling Dr. Claudio Balzani Dr. Jan Teßmer, "Schlussbericht - Smart Blades," DLR, IWES, ForWind, Braunschweig, Jul. 2016
- [5] D. M. Pohl, "Smar Blades 2 - Dauerversuch der Hinterkante," DLR, Braunschweig, Oct. 2018
- [6] E. B. Nick Jenkins David Sharpe Tony Burton, "Wind Energy Handbook," Wiley, 2011, p. 7
- [7] R. A. Thomas P. Sevinc A. Rosemeier M. Bätge M. Braun R. Meng F. Horte D. Balzani C. Bleich O. Daniele E. Stoevesandt B. Wentingmann M. Polman J. D. Leimeister M. Schümann B. Popko W., "IWES Wind Turbine IWT-7.5-164 Rev 4," Bremerhaven: Fraunhofer Institute for Wind Energy Systems IWES, 2018, p. 30 [Online]
Available: <https://doi.org/10.24406/IWES-N-518562> [Accessed: 10-Apr-2019]
- [8] P. Thomas, "Lastrechnung und Systemdynamik." [Online]
Available:
<https://www.iwes.fraunhofer.de/de/forschungsspektrum/einstiegsseite-hersteller-und-zulieferer/aerodynamik-fuer-windenergieanlagen/Lastrechnung-und-Systemdynamik.html#tabpanel-2011683939> [Accessed: 8-Apr-2019]
- [9] Stackexchange, "Graphic Design." [Online]
Available: <https://graphicdesign.stackexchange.com/questions/35038/how-to-draw-a-wing-cascade-with-boundary-layers> [Accessed: 23-Apr-2019]
- [10] R. A. Thomas P. Sevinc A. Rosemeier M. Bätge M. Braun R. Meng F. Horte D. Balzani C. Bleich O. Daniele E. Stoevesandt B. Wentingmann M. Polman J. D. Leimeister M. Schümann B. Popko W., "IWES Wind Turbine IWT-7.5-164 Rev 4," Bremerhaven: Fraunhofer Institute for Wind Energy Systems IWES, 2018, p. 26 [Online]
Available: <https://doi.org/10.24406/IWES-N-518562> [Accessed: 10-Apr-2019]
- [11] I. E. Commission, *International Standard IEC 61400-1, Wind Turbines - Part 1: Design requirements*. International Electrotechnical Commission, 2005
- [12] S. Pansart, *DNV GL Standard, Rotor blades for wind turbines*. DNV GL, Renewables Certification, Section rotor blades, 2015
- [13] DLR, "CPACS." [Online]
Available: <https://www.cpacs.de/> [Accessed: 2-May-2019]
- [14] W. C. Heinecke F. Führer T. Freund S., "Parametric Model Generation and Sizing of Lightweight Structures for a Multidisciplinary Design Process," NAFEMS DACH-Tagung, Bamberg, May 2014
- [15] *HyperSizer 7.3 Manual*. Collier Research Corporation, 2018
- [16] R. M. Jones, "Mechanics of Composite Materials," Taylor & Francis, 1999, p. 70 ff.
- [17] R. M. Jones, "Mechanics of Composite Materials," Taylor & Francis, 1999, p. 191 f.
- [18] R. M. Jones, "Mechanics of Composite Materials," Taylor & Francis, 1999, p. 195 ff.

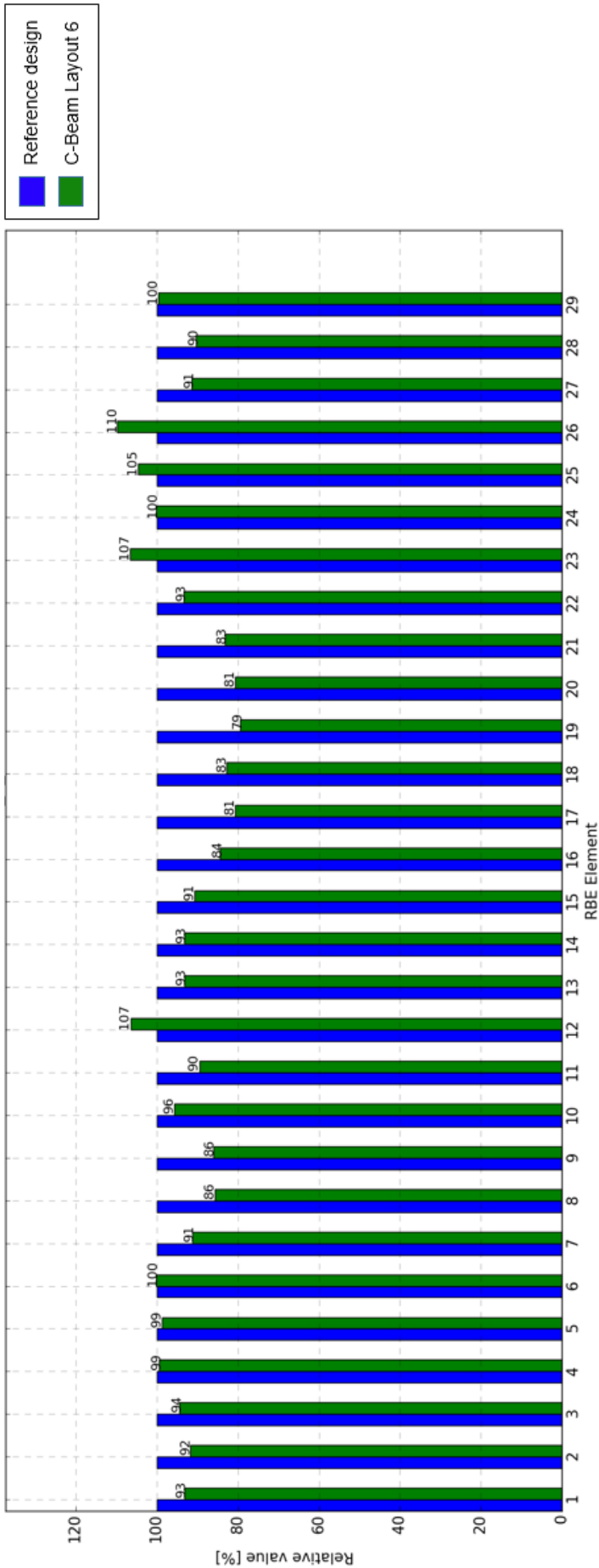
- [19] S. D. Christian Willberg, "WindMUSE - Windturbine in Multidisziplinärer Simulationsumgebung," DLR, 2017
- [20] Incotology, "Multiaxial-Gelege." [Online]
Available: <http://incotology.de/multiaxial-gelege/> [Accessed: 23-Apr-2019]
- [21] R. M. Jones, "Mechanics of Composite Materials," Taylor & Francis, 1999, p. 63
- [22] D.-I. T. H. Dipl.-Ing. Tobias Schulze Prof. Dr.-Ing. Berthold Schlecht, "Multibody-System-Simulation Of Wind Turbines For Determination Of Additional Dynamic Loads." Nov-2004 [Online]
Available:
http://www.simpack.com/fileadmin/simpack/doc/usermeeting04/um04_tu-dresden-schu.pdf [Accessed: 3-May-2019]
- [23] F. Meng, "Loads of the reference turbine," IWES, 2015
- [24] I. E. Commission, *International Standard IEC 61400-1, Wind Turbines - Part 1: Design requirements, Amendment 1*. International Electrotechnical Commission, 2010
- [25] DLR, "Distributed Integration Environment." [Online]
Available: <http://rcenvironment.de> [Accessed: 5-May-2019]
- [26] K.-H. G. und Jörg Feldhusen, Ed., "Dubbel - Taschenbuch für den Maschinenbau," Springer Vieweg, 2014, p. C 17
- [27] NASA, "Center of Pressure." [Online]
Available: <https://www.grc.nasa.gov/www/k-12/airplane/cp.html> [Accessed: 18-Apr-2019]
- [28] E. Werthen, "Bewertung unkonventioneller Bauweisen - Definition der Parameterstudie," DLR, 2017
- [29] D. Verelst and T.Larsen, "Load Consequences when Sweeping Blades - A Case Study of a 5 MW Pitch Controlled Wind Turbine," Forskningscenter Risoe, Tekniske Universitet Riso, 2010

Appendix

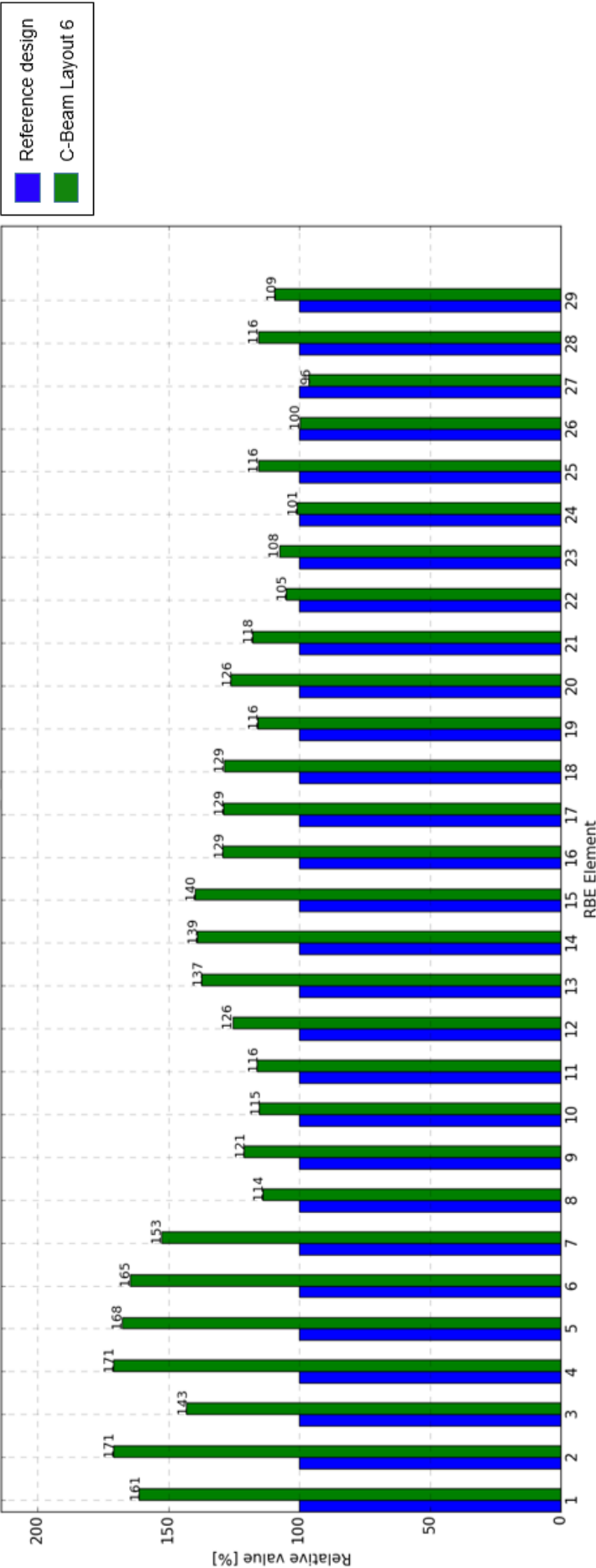
A. C-Beam Layout 6 RBE Element Forces and Moments



Comparison of the total $F_{x_{min}}$ loads – Reference Design vs. C-Beam Layout 6

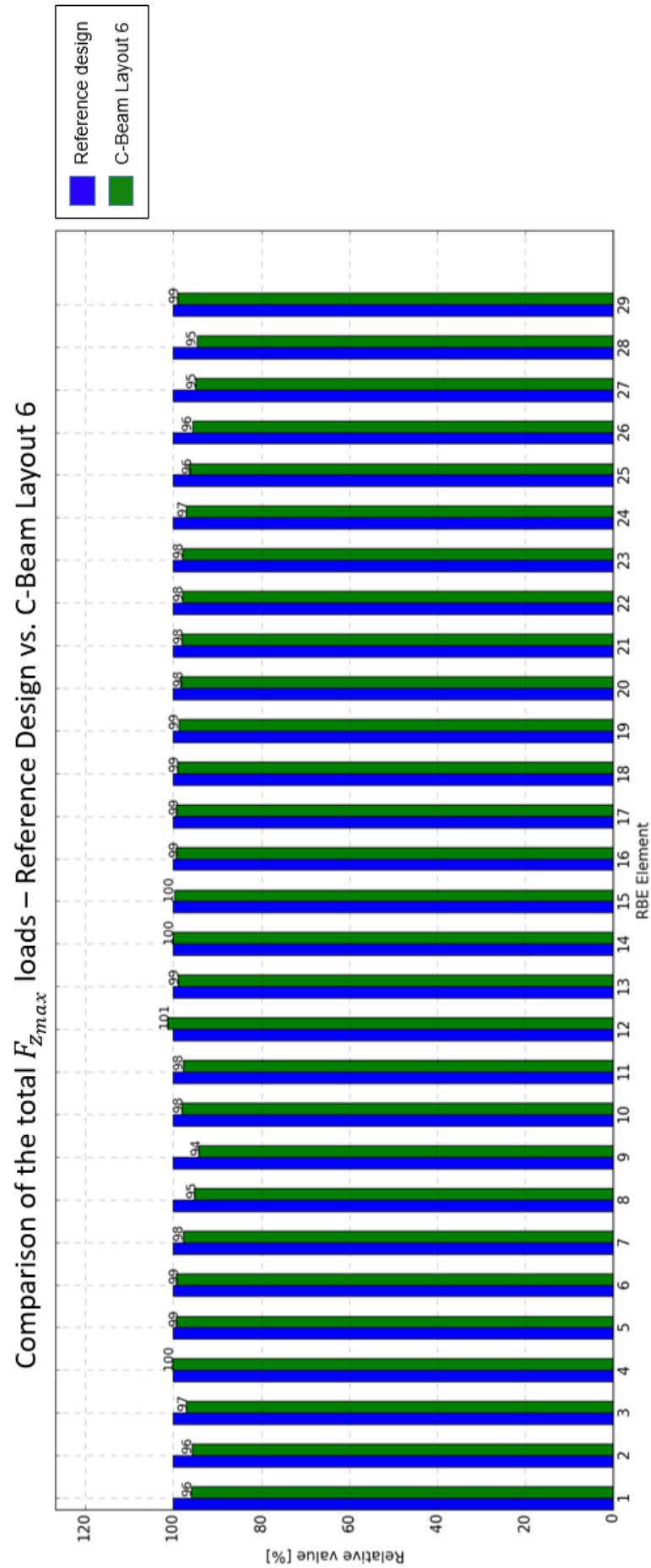


Comparison of the total $F_{y_{max}}$ loads – Reference Design vs. C-Beam Layout 6

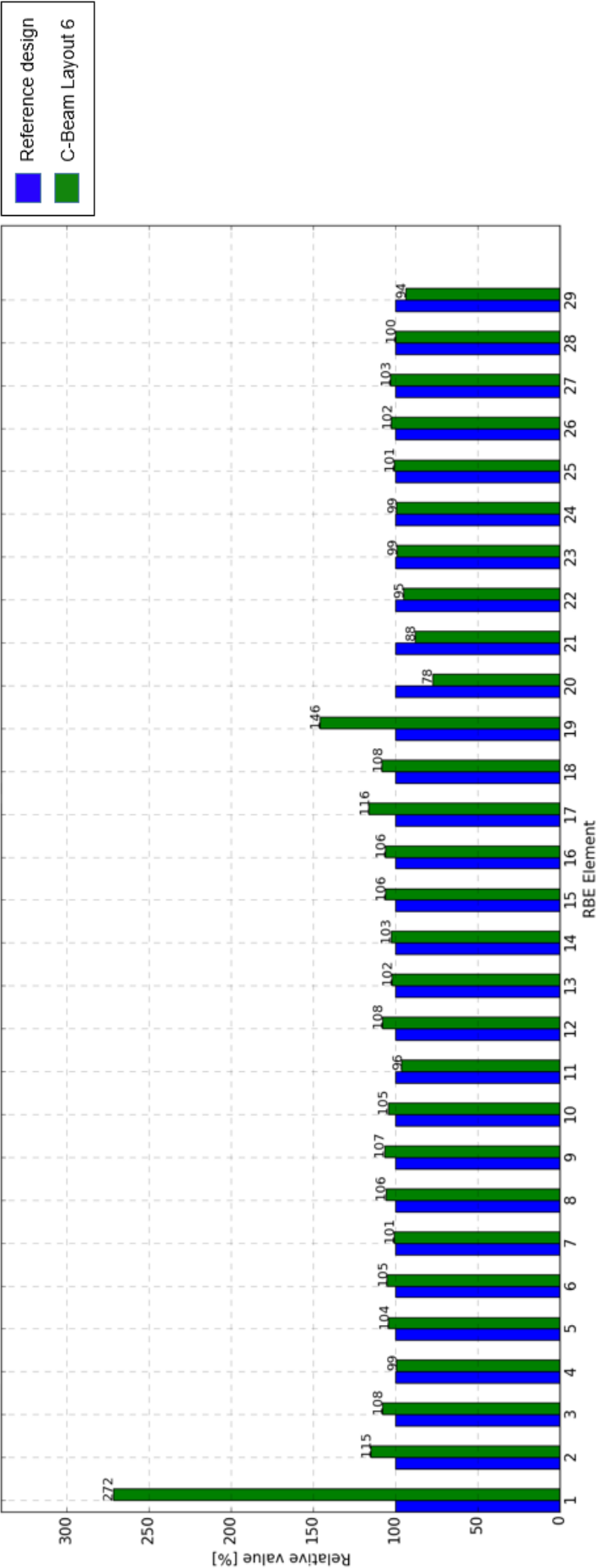


Comparison of the total F_{ymin} loads – Reference Design vs. C-Beam Layout 6

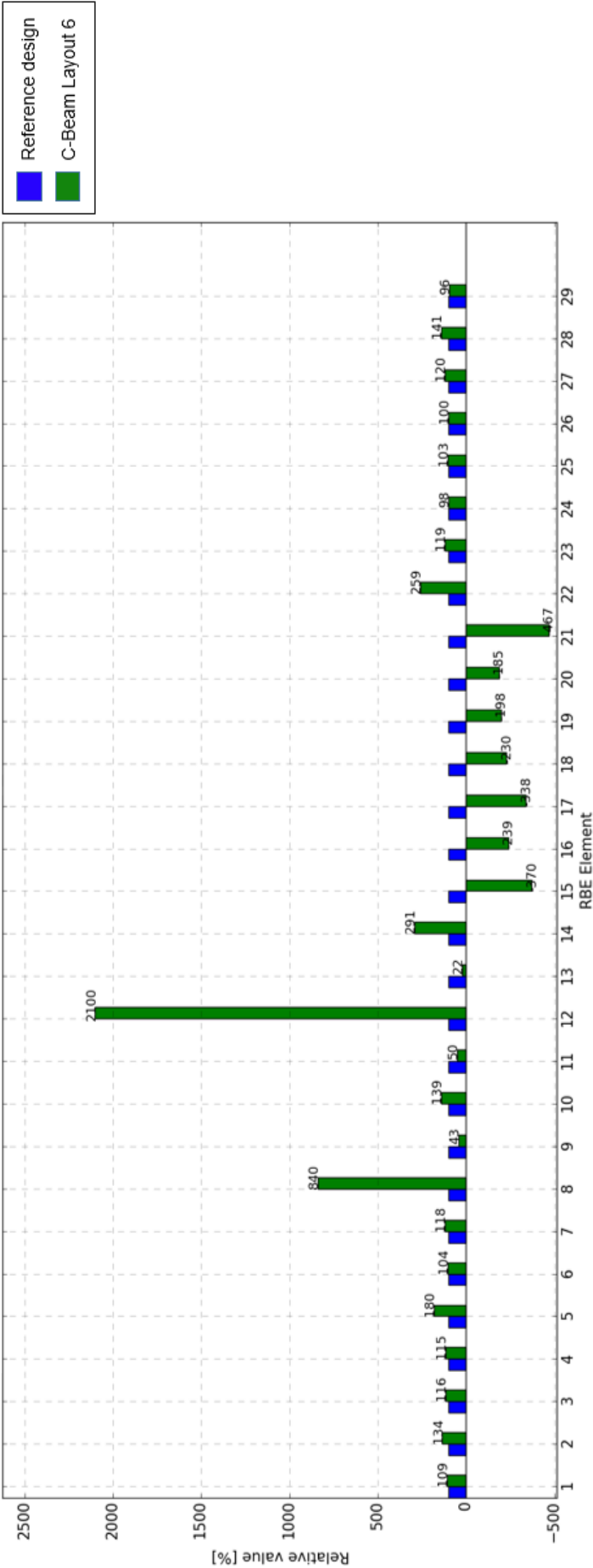




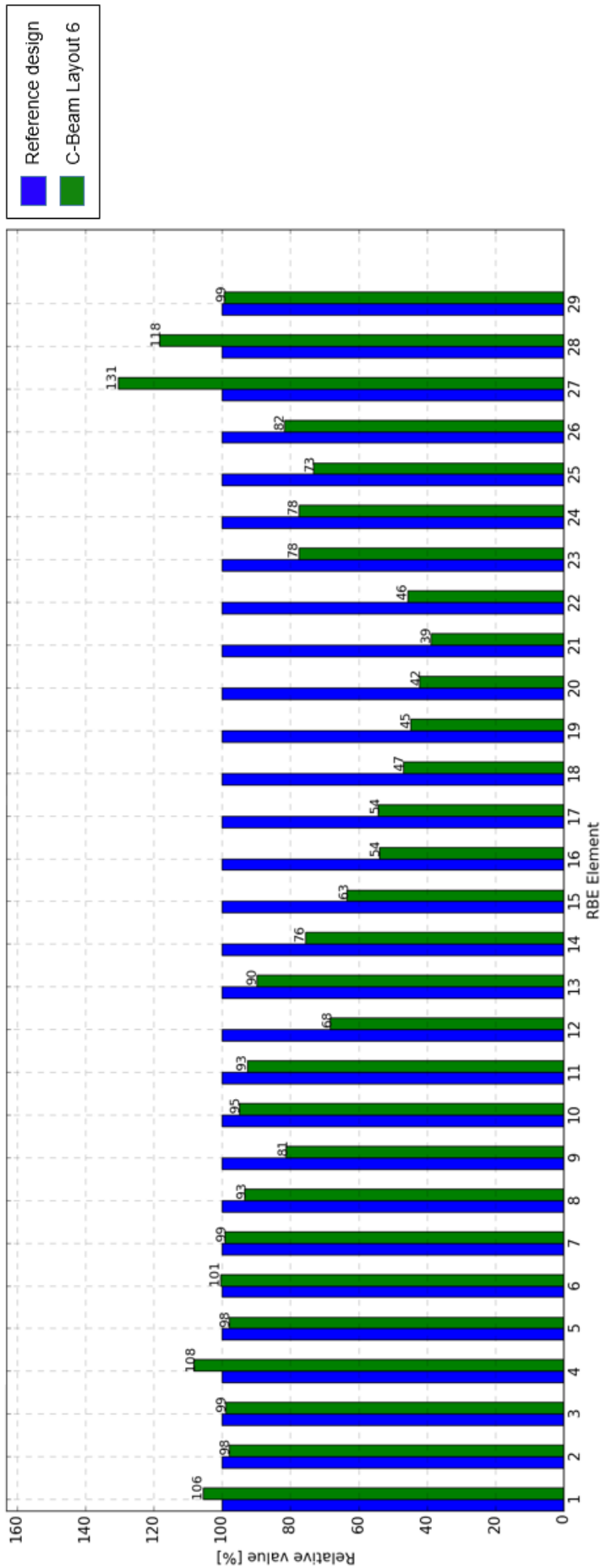
Comparison of the total $F_{Z_{min}}$ loads – Reference Design vs. C-Beam Layout 6



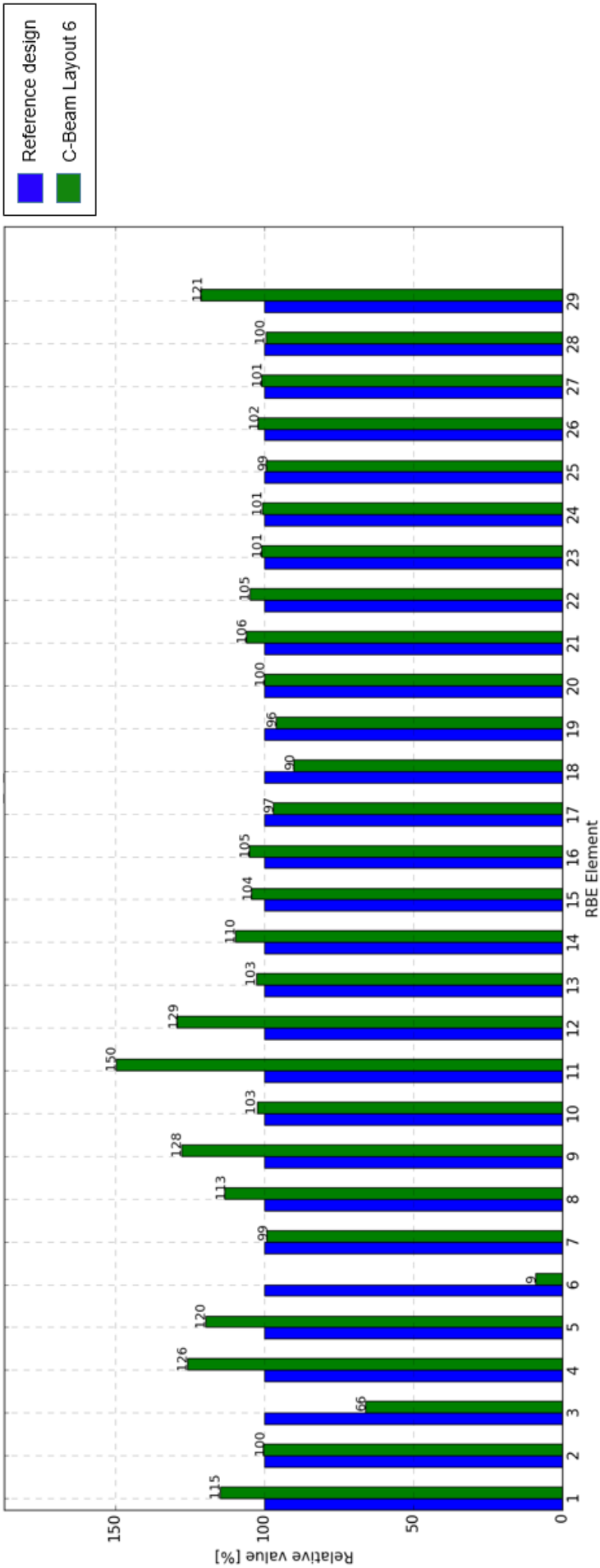
Comparison of the total $M_{x_{max}}$ loads – Reference Design vs. C-Beam Layout 6



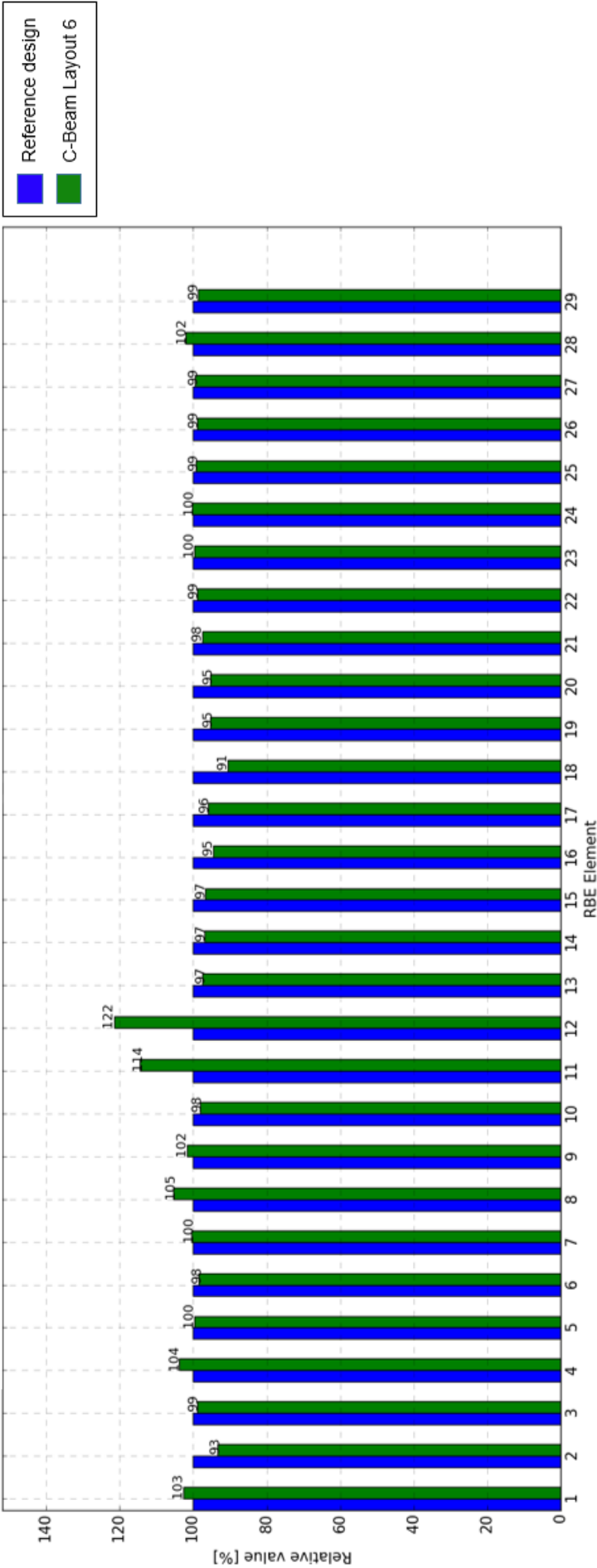
Comparison of the total $M_{x_{min}}$ loads – Reference Design vs. C-Beam Layout 6



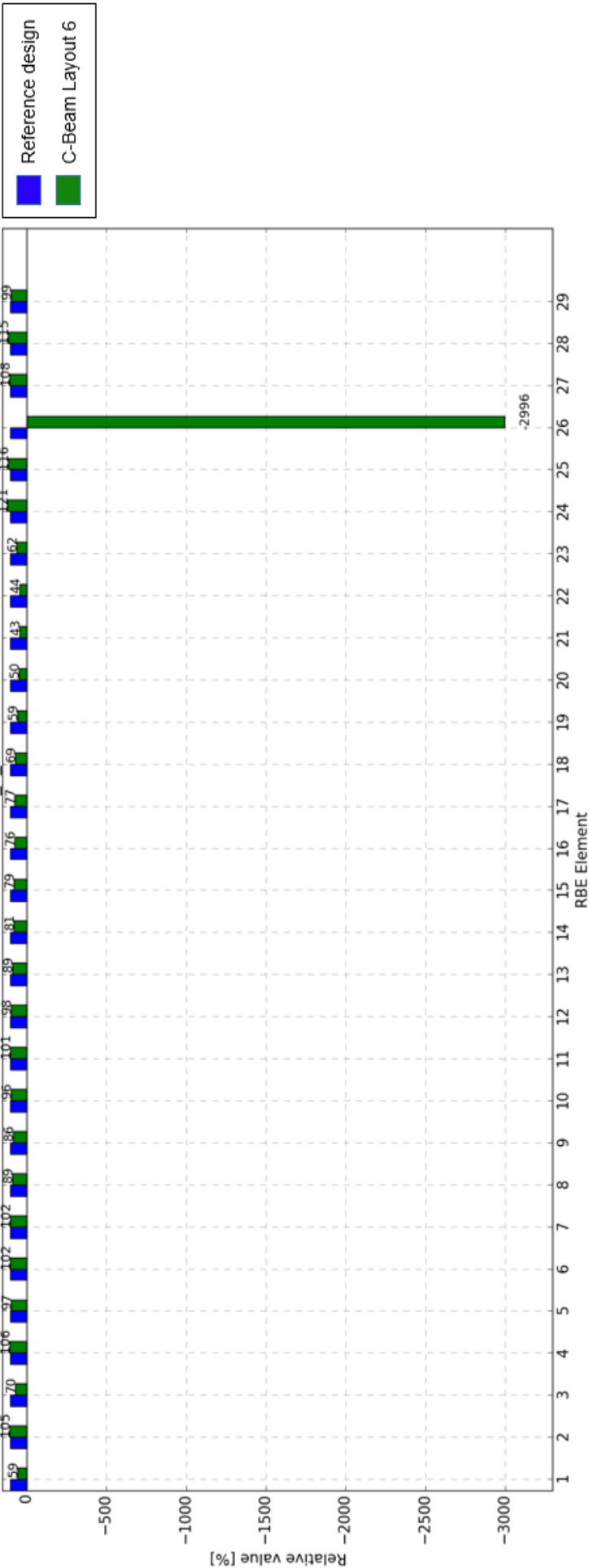
Comparison of the total $M_{y_{max}}$ loads – Reference Design vs. C-Beam Layout 6



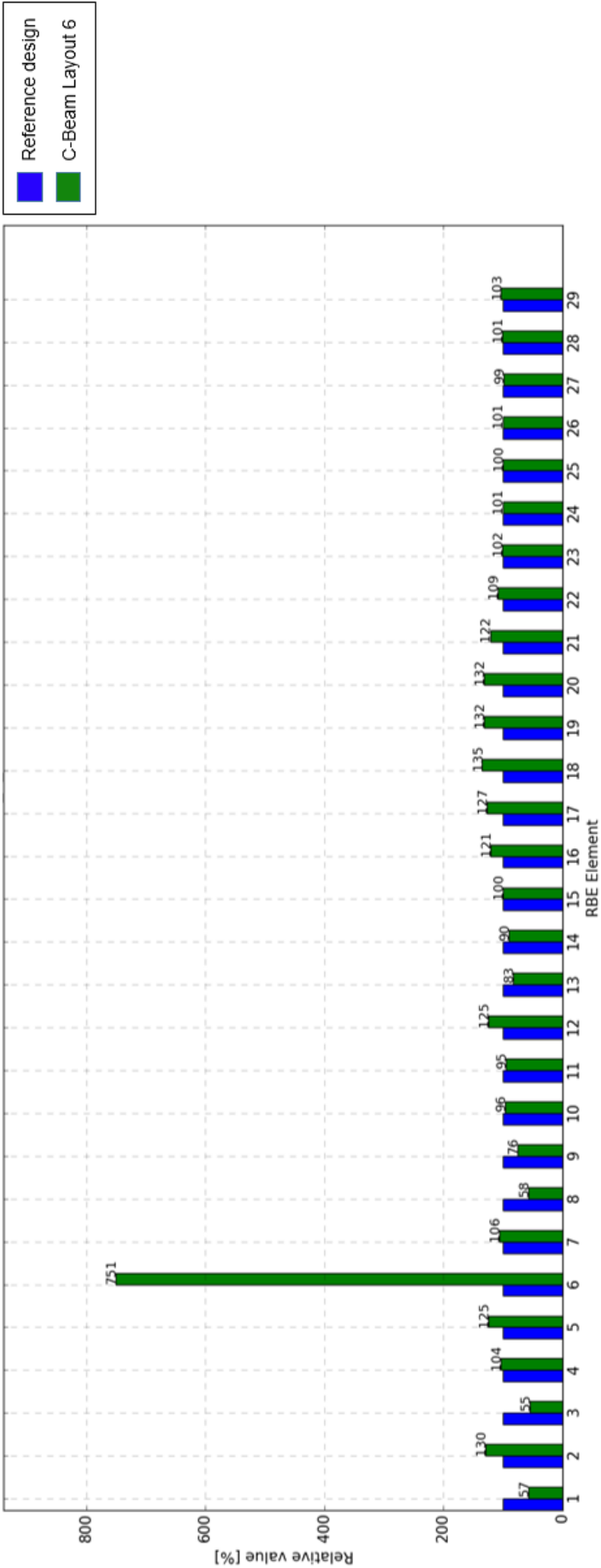
Comparison of the total $M_{y_{min}}$ loads – Reference Design vs. C-Beam Layout 6



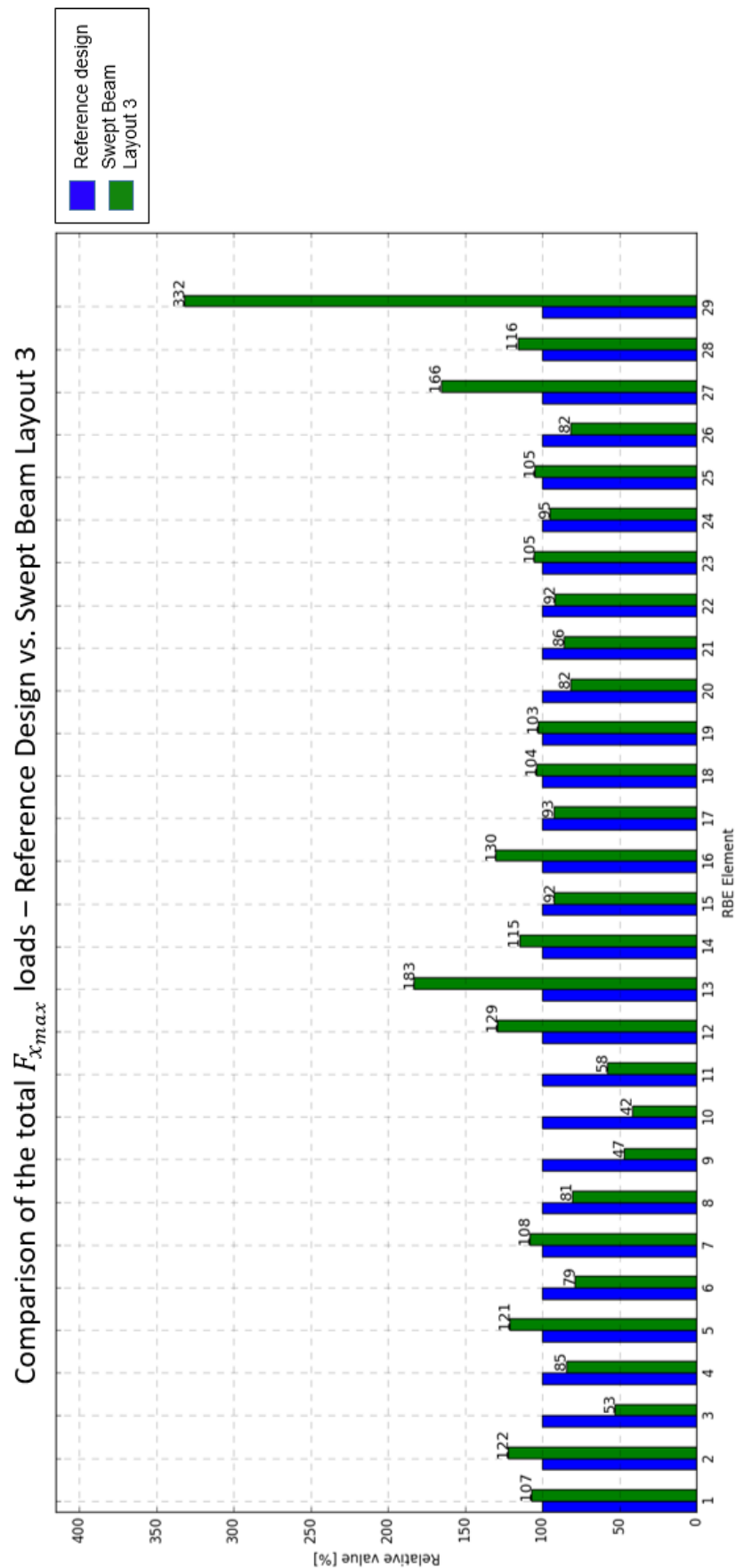
Comparison of the total $M_{z_{max}}$ loads – Reference Design vs. C-Beam Layout 6



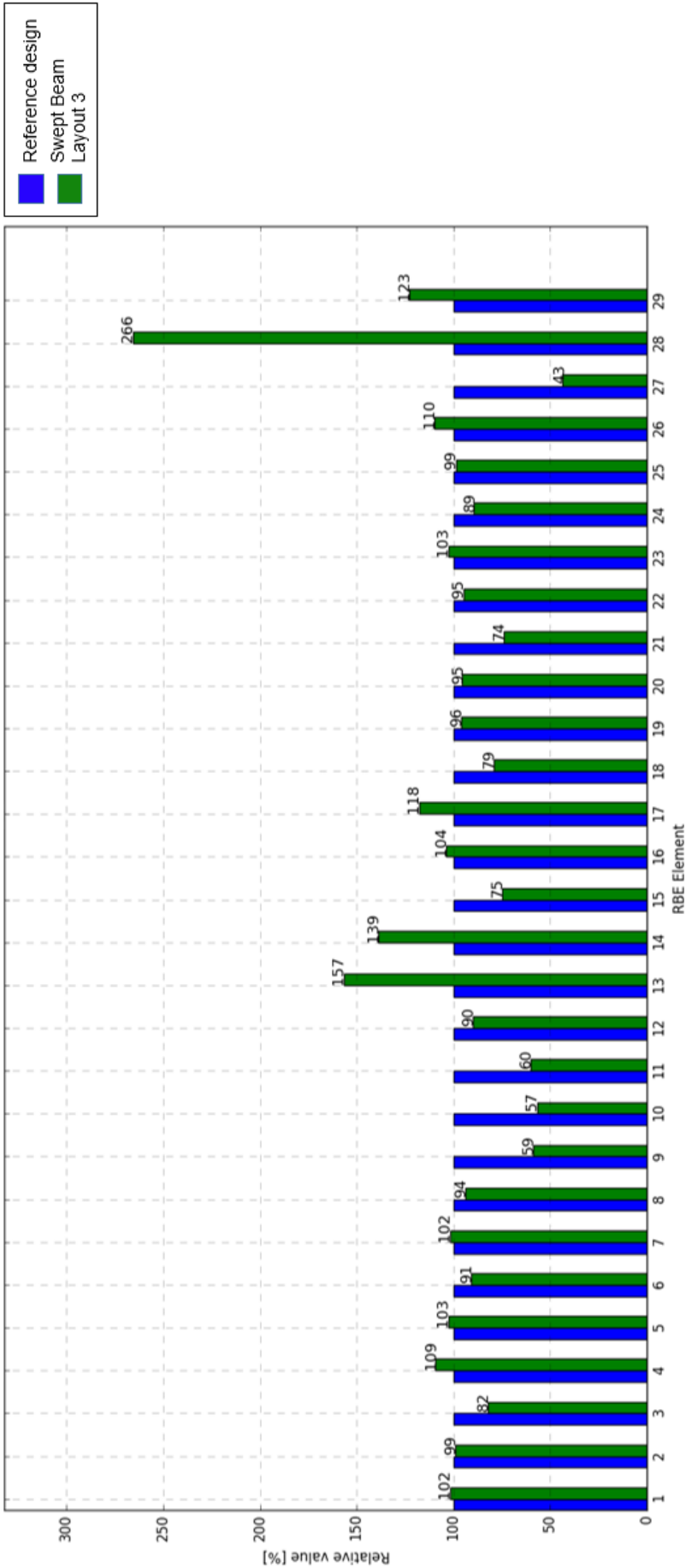
Comparison of the total $M_{z_{min}}$ loads – Reference Design vs. C-Beam Layout 6



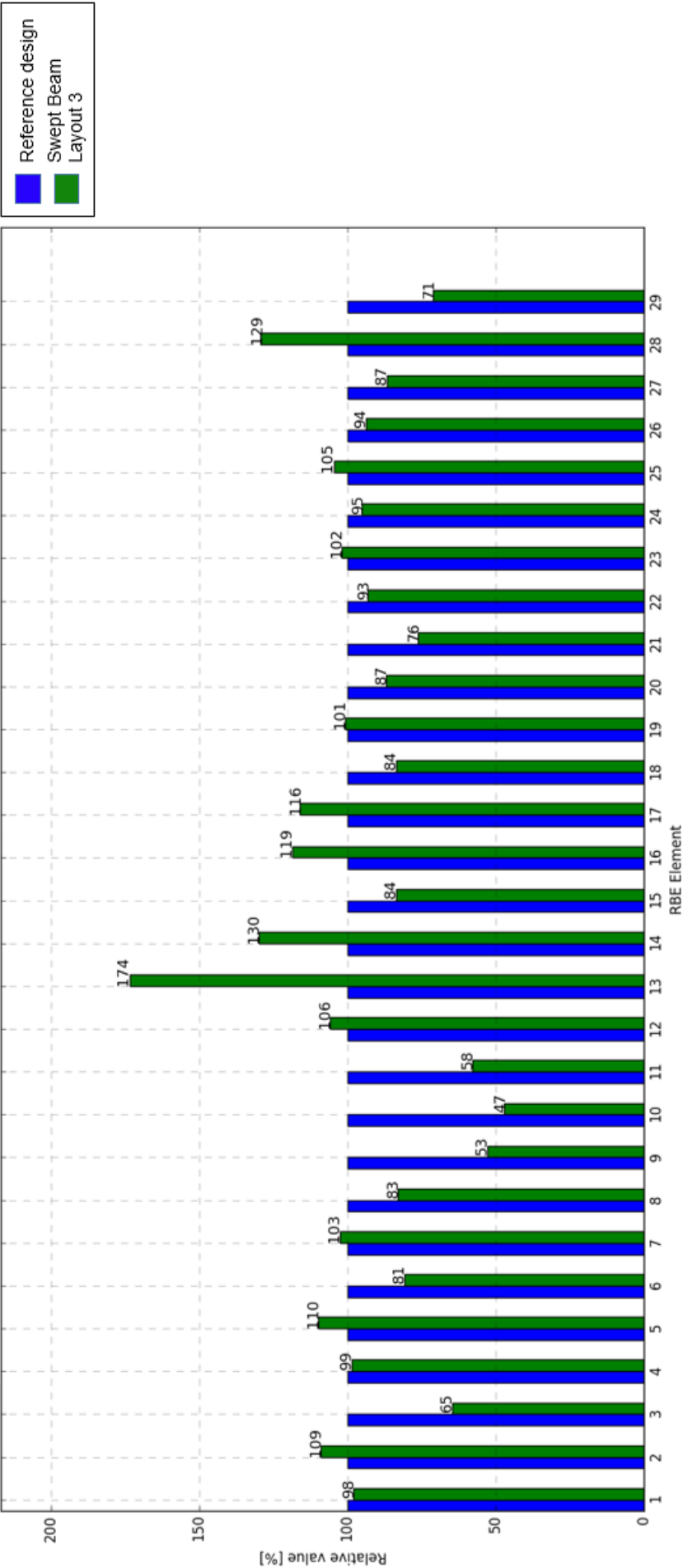
B. Swept Beam Layout 3 RBE Element Forces and Moments



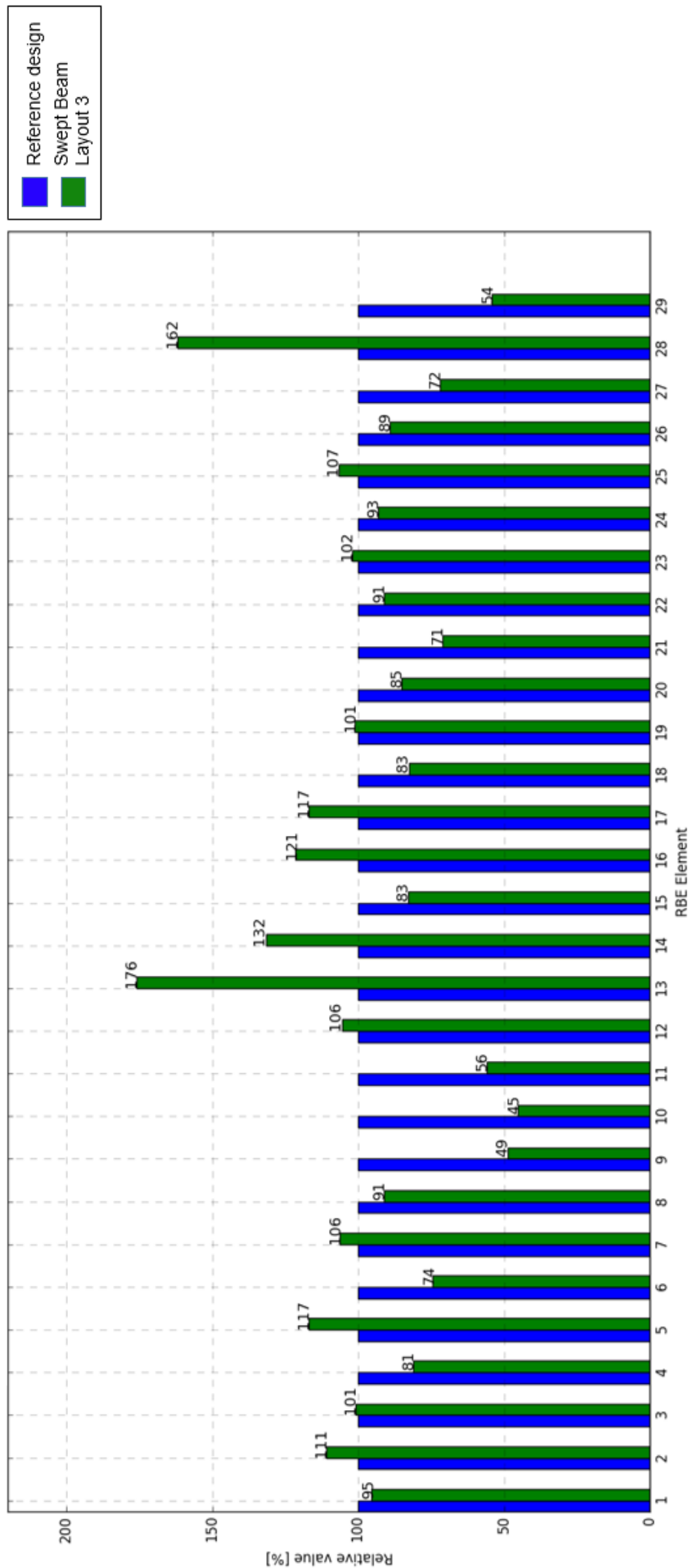
Comparison of the total $F_{x,min}$ loads – Reference Design vs. Swept Beam Layout 3



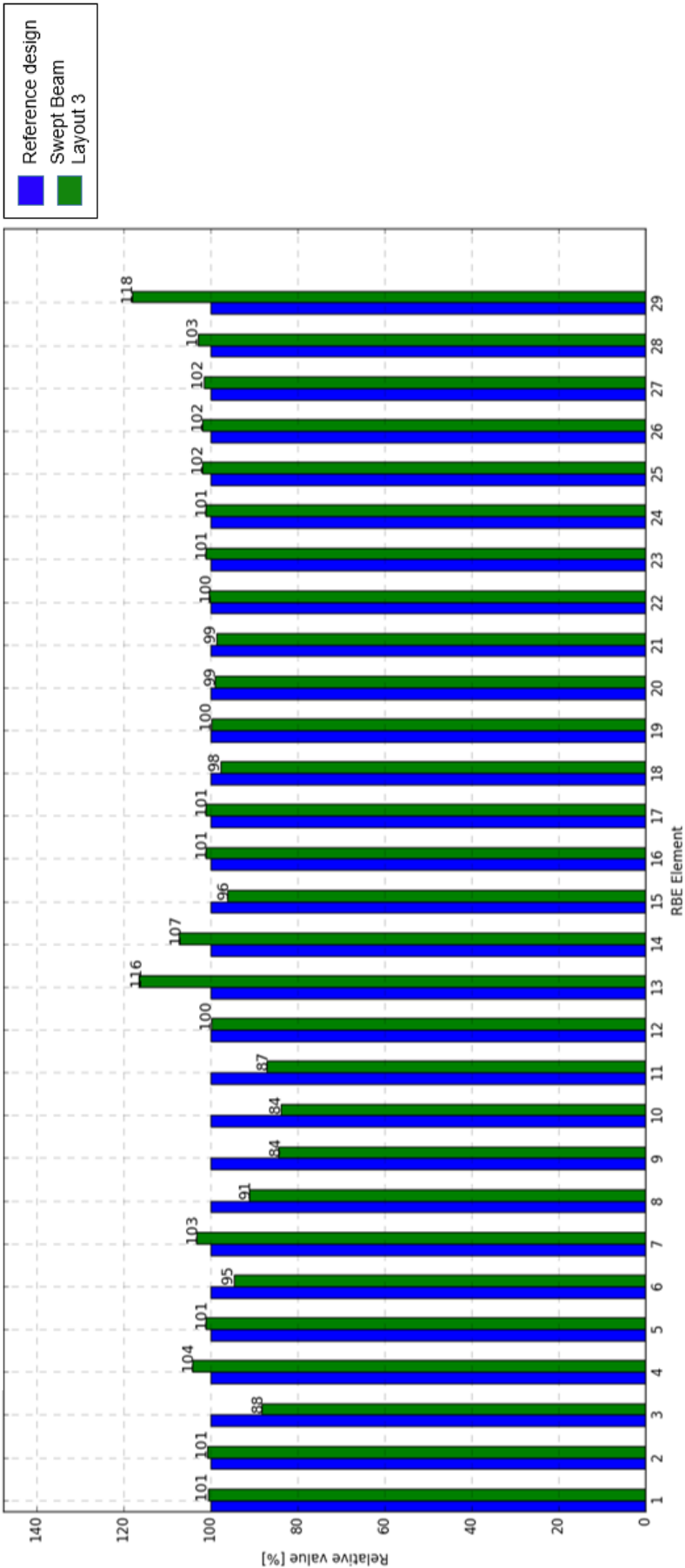
Comparison of the total $F_{y_{max}}$ loads – Reference Design vs. Swept Beam Layout 3



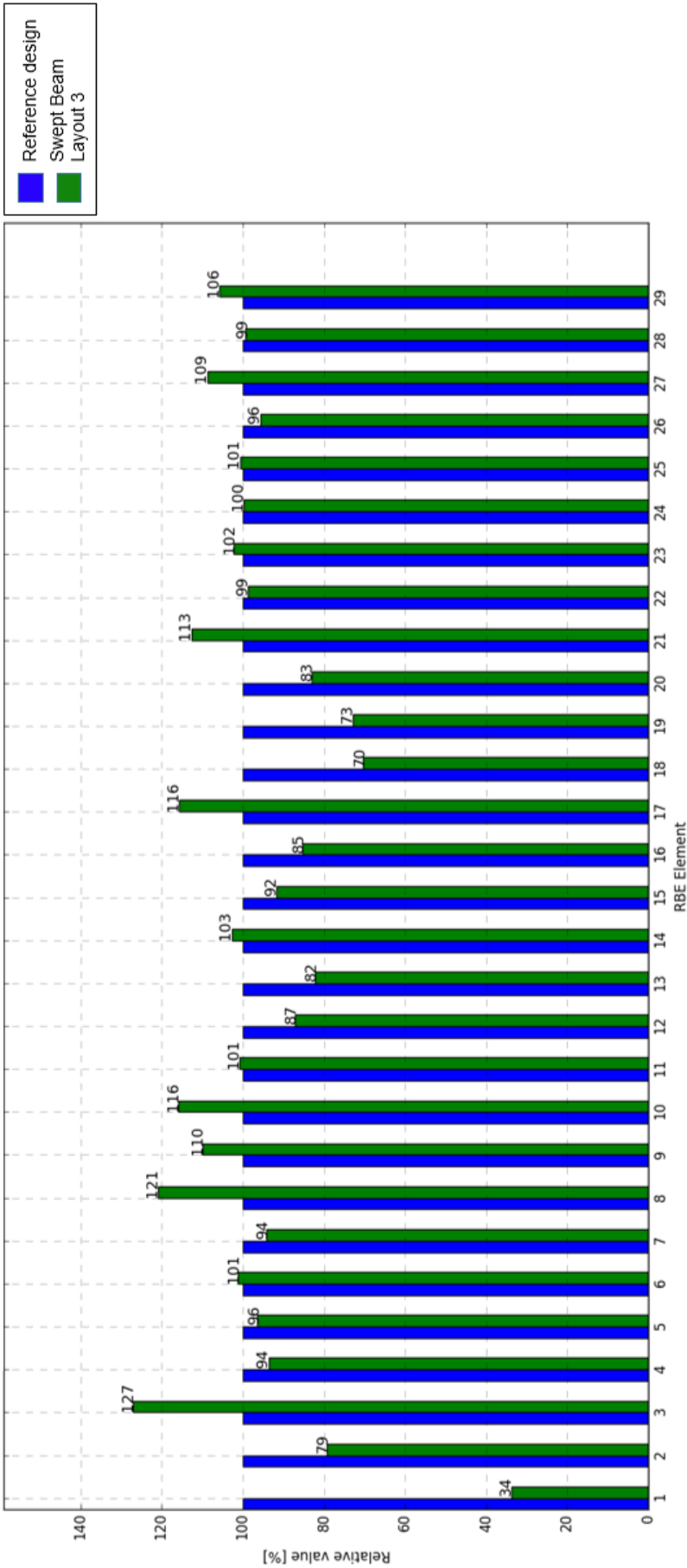
Comparison of the total $F_{y_{min}}$ loads – Reference Design vs. Swept Beam Layout 3



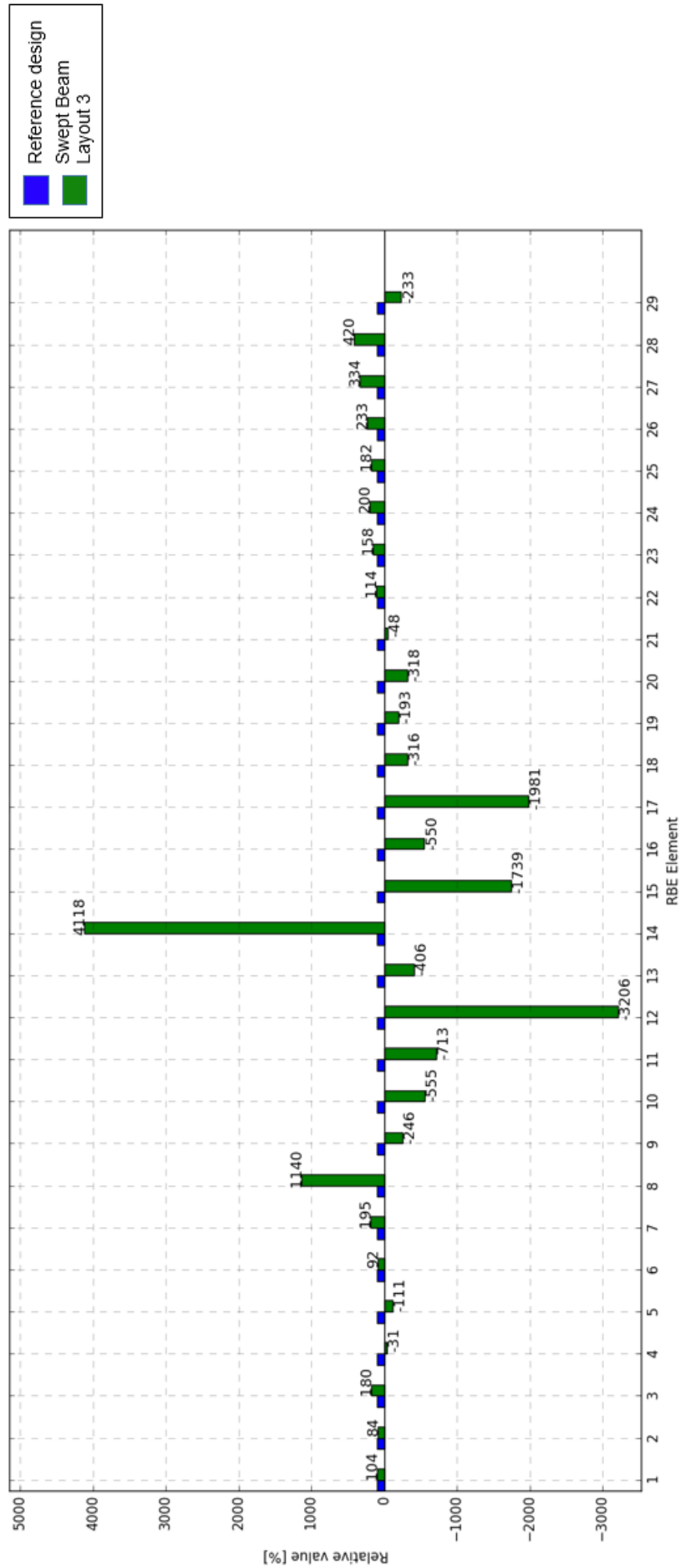
Comparison of the total $F_{Z_{max}}$ loads – Reference Design vs. Swept Beam Layout 3



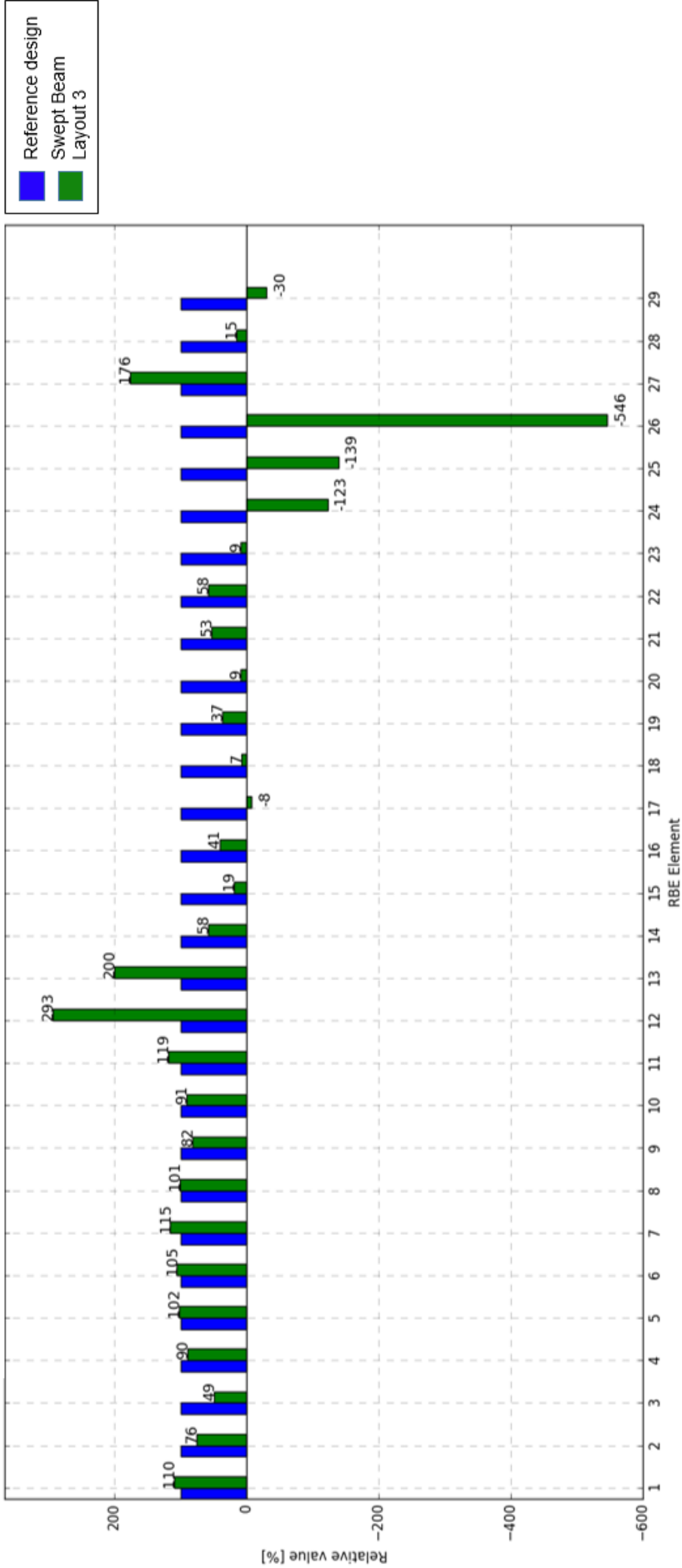
Comparison of the total $F_{z_{min}}$ loads – Reference Design vs. Swept Beam Layout 3



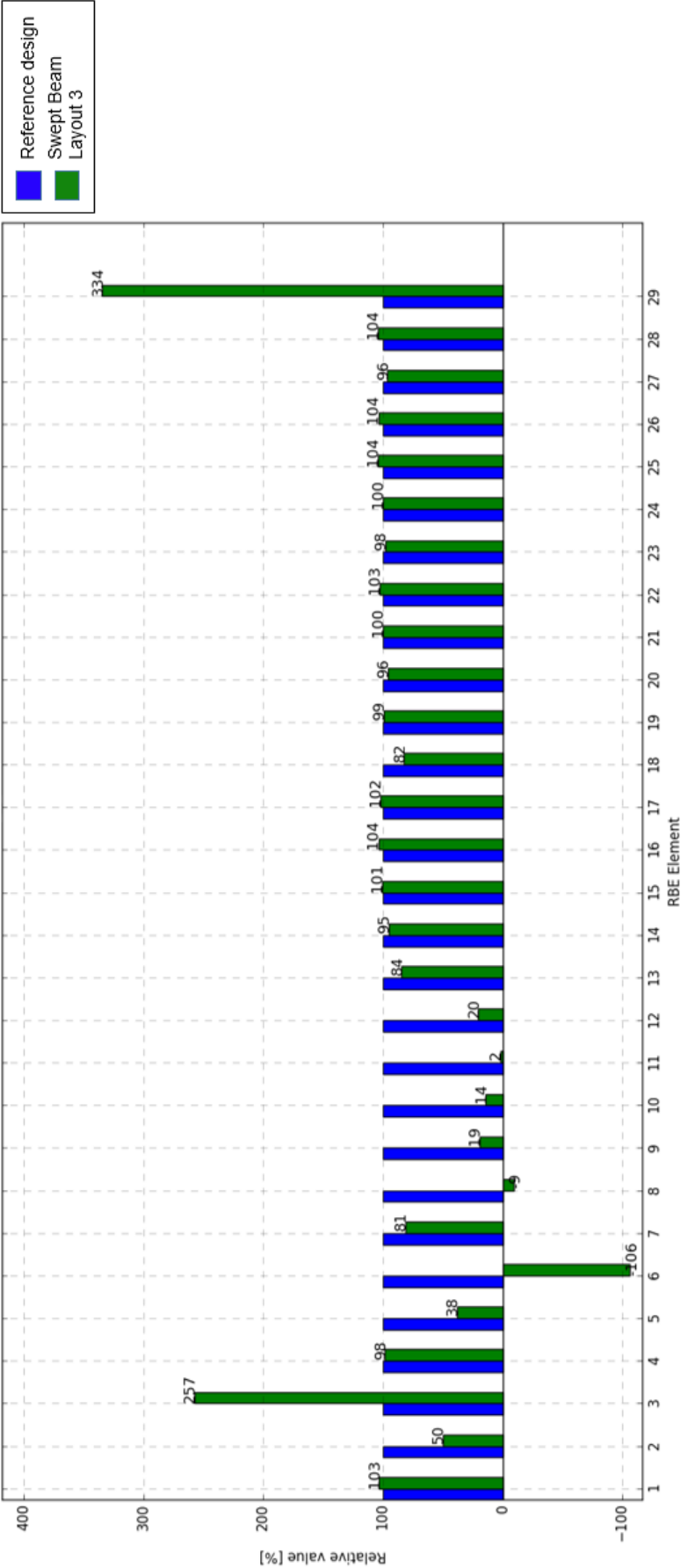
Comparison of the total $M_{x_{max}}$ loads – Reference Design vs. Swept Beam Layout 3



Comparison of the total $M_{x_{min}}$ loads – Reference Design vs. Swept Beam Layout 3



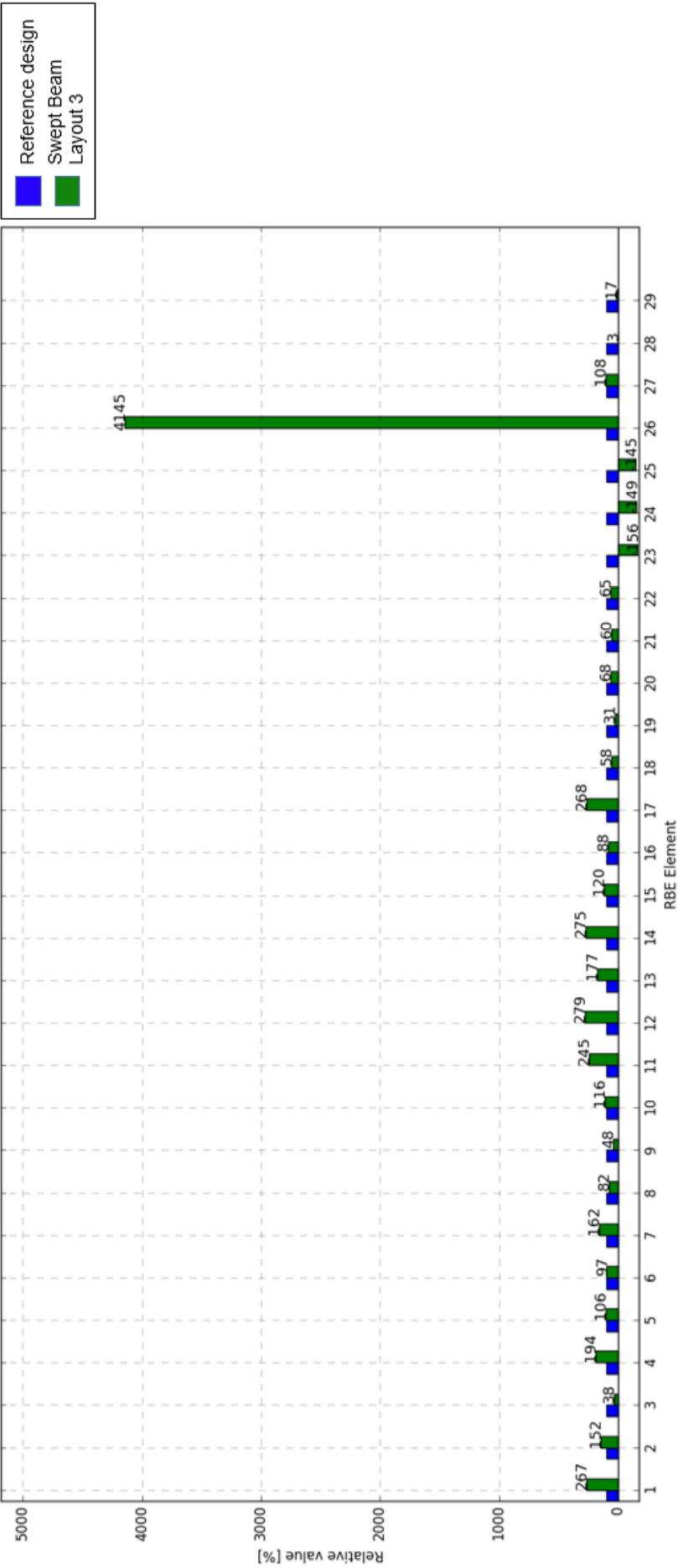
Comparison of the total $M_{y_{max}}$ loads – Reference Design vs. Swept Beam Layout 3



Comparison of the total $M_{y_{min}}$ loads – Reference Design vs. Swept Beam Layout 3



Comparison of the total $M_{Z_{max}}$ loads – Reference Design vs. Swept Beam Layout 3



Comparison of the total $M_{Z_{min}}$ loads – Reference Design vs. Swept Beam Layout 3

